EFFECT OF PENETRATOR CONFIGURATION AND SIZE ON THE DYNAMIC BEHAVIOR OF COMPOSITE MATERIAL UNDER HIGH STRAIN RATE LOADING

by

Ojo Olorunfemi Bamisaye

HND, The Polytechnic, Ibadan Oyo State, Nigeria 1995

PGD, Rivers State University of Technology, Port Harcourt, Nigeria 1998

M.Sc, University of Pittsburgh, Pittsburgh 2003

Submitted to the Graduate Faculty of

School of Engineering in partial fulfillment

of the requirements for the degree of

Master of Science

University of Pittsburgh

2003

UNIVERSITY OF PITTSBURGH

SCHOOL OF ENGINEERING

This thesis was presented

by

Ojo Olorunfemi Bamisaye

It was defended on

June 20, 2003

and approved by

Dr. Dipo Onipede, Assistant Professor, Department of Mechanical Engineering

Dr. Slaughter IV William, Associate Professor, Department of Mechanical Engineering

Thesis Advisor: Dr. Sylvanus N. Nwosu, Associate Professor, Department of Mechanical Engineering

ABSTRACT

EFFECT OF PENETRATOR CONFIGURATION AND SIZE ON THE DYNAMIC BEHAVIOR OF COMPOSITE MATERIAL UNDER HIGH STRAIN RATE LOADING

Olorunfemi B. Ojo, MS

University of Pittsburgh, 2003

Dynamic test was carried out on a plain weave carbon epoxy composites plate of different thickness (12, 16 and 24 layers) to determine the penetration and perforation threshold energies for each specimen using penetrators of different sizes and geometries namely: Protruding spherical, protruding hemispherical and conical hemispherical penetrators. The specimen damage thresholds considered in this thesis are: Below ballistic limit (BBL), at ballistic limit (BL) and above ballistic limit (ABL). Ballistic limit here is defined as the threshold energy or minimum energy that has to be exceeded before perforation takes place on the specimen.

High strain rate loading on the specimen was achieved by a newly installed Penetrating Split Hopkinson bar (P-SPHB) in the Material Behavior Lab at the University of Pittsburgh. A model 220 CCD video camera and 330 high speed imaging camera was used to measure the speed of crack propagation in the specimens. Cracks were found to propagate faster in the thinner specimen in all the damage thresholds.

The ballistic limit for each specimen was experimentally determined. The result shows that sample thickness, penetrator size and geometries play a significant role in characterizing specimen damage. Energy absorption rate was found to increase as the penetrator size increased.

The nature of specimen damage was found to depend on the penetrator geometry. The result also shows that strain depends on both striker impact energy and the target thickness. By varying the penetrator size and geometries it was discovered that both variables play a significant role in energy absorption rate of the specimen.

ACKNOWLEDGEMENT

I would like to thank the Almighty God for seeing me through my studies at the University of Pittsburgh. Also I would like to express my appreciation to several individuals whose invaluable contributions to this work has made it a great success: Dr. Sylvanus Nwosu, my advisor for this thesis, for allowing me to work on this research with him. Thank you for your help and advise throughout the entire period of this research; Dr. Dipo Onipede (Jnr) my thesis committee member, for your encouragement and support during my studies at the University of Pittsburgh, Dr William Slaughter (IV) for accepting to serve as a member of my committee; Dr. Mike Okoroafor (Technology Director, Coca Cola) whose encouragement made me to take the step of pursuing my graduate degree; Mr. Lawrence Herman, Keith Devine, Bob and Scott (mechanical workshop) for your technical assistance in putting together the research Lab; Miss Beth Buhot (Diversity program assistant) for your help in getting all the research materials ordered in a timely manner.

I would also like to thank the US Wright Patterson Air Force base for sponsoring this research and Dr. Arnold Mayer who is the program coordinator.

Lastly, I want to thank my dear wife Adenike and children (Mayowa and Moyosore) for their unflinching support and understanding throughout this period. Thank you Sweetie for tolerating my shortcomings. Special thanks also to my Father and Mother who were the architects of the whole thing. Mr. Bayo Adedimila for your help in proofreading this thesis. May God bless and reward you all (Amen).

TABLE OF CONTENTS

Page

ABSTRACT ……...iii

ACKNOWLEDGEMENT ……v

LIST OF TABLES ……....x

LIST OF FIGURES ……...xi

1.0 INTRODUCTION ……...1

1.1 Various Test Techniques Used for Composite Material Testing. ……..…7

1.1.1 Hydraulic machine test method ……..…7

1.1.2 Izod Method ……..…7

1.1.3 Charpy Method ……..…7

1.1.4 Drop Weight ……8

1.1.5 Gas gun method ……8

1.1.6 Hopkinson Bar ……..…9

2.0 THEORETICAL FORMULATION AND DATA REDUCTION PROCESS ……11

2.1 Data Reduction Process ……11

2.1.1 Determination of Energy absorbed parameters ……13

2.1.2 Sample stress measurement ……16

3.0 EXPERIMENTAL SETUP ……18

3.1 Base Support ……18

3.2 Alignment Flat Bar ……19

3.3 Hammer Assembly ……20

3.4 Striker Rod ……20

3.5 Design of Penetrator ……....21

3.6 Brief Description of Hopkinson bar Operation ……23

3.7 System Calibration ……....31

3.7.1 Striker and Penetrator Velocity (Calibration results) ……31

3.7.1.2 Calibration ……....31

3.8 Criteria for experimental validation of Hopkinson bar ……...34

4.0 EXPERIMENTAL RESULT ……...36

4.1 Determination of Ballistic Limit for Woven and Laminated Composites ……..…….36

4.2 Characterization of the Wave Forms ……42

4.3 Effect of penetrator size on dynamic failure response of graphite epoxy (woven) composite around the critical perforation energy ……...49

4.3.1 Effect of penetrator size on damage parameter around the Critical Energy using spherical protruding Penetrator for varying sample thickness ……..50

4.3.1.1 Energy Absorbed – time Profile ……...50

4.3.1.2 Effect of penetrator size on Energy absorbed for varying sample Thickness ……...55

4.3.1.3 Strain rate – Strain Behavior ……55

4.3.1.4 Stress–Strain profile for varying thickness around the ballistic limit vicinity ……61

4.3.1.5 Force – Displacement ……....63

5.0 EFFECT OF PENETRATOR GEOMETRY ON DYNAMIC FAILURE RESPONSE OF GRAPHITE EPOXY (WOVEN) COMPOSITE AROUND THE CRITICAL PERFORATION ENERGY ……67

5.1 3/16-inch Protruding Spherical and 3/16-inch Protruding Hemispherical penetrator …..67

5.1.1 Energy Absorbed ……67

5.1.2 Strain rate-Strain ……69

5.1.3 Force – Displacement ……72

5.2 1/4-inch Protruding Spherical and 1/4- inch Conical Hemispherical Penetrators ……74

5.2.1 Energy Absorbed profile ……74

5.2.2 Strain rate – Strain ……77

5.2.3 Force – Displacement ……79

6.0 EFFECT OF SAMPLE THICKNESS ON THE SPEED OF CRACK PROPAGATION USING 1/4-INCH PROTRUDING SPHERICAL PENETRATOR WITH THE AID OF AN HIGH SPEED DIGITAL VIDEO IMAGING CAMERA ……84

6.1 Introduction ……84

6.1.1 Operation of model 330 camera ……84

6.1.2 Calibration and magnification of the high speed camera ……86

6.2 Effect of penetrator geometry on speed of crack propagation around the ballistic limit using the high-speed CCD intensifier camera ……95

7.0 CONCLUSIONS ……100

APPENDIX ……102

BIBLOGRAPHY ……105

LIST OF TABLES

Page

Table 4.1 Damage initiation energy/layer for graphite epoxy woven specimen using 3/16 –inch Protruding Spherical……...40

Table 4.2 Damage initiation energy/layer for graphite epoxy woven specimen using 7/32 -inch Protruding Spherical……41

Table 4.3 Damage initiation energy/layer for graphite epoxy woven specimen using 1/4 -inch Protruding Spherical……..41

Table 4.4 Damage initiation energy/layer for graphite epoxy woven specimen using 3/16 -inch Protruding Hemispherical……41

Table 4.5 Damage initiation energy/layer for graphite epoxy woven specimen using 1/4 -inch Conical Hemispherical……..….42

LIST OF FIGURES

Page

Figure 3.1 Showing typical alignment flat bar for both incident and transmitter bar ……19

Figure 3.2 Showing different penetrators geometries and sizes ……22

Figure 3.3 A schematic diagram of the penetrating Hopkinson pressure bar system showing (a) Perforation sample holder fixture (b) System configuration and instrumentation……25

Figure 3.4 (a) Typical wave showing the incident, reflected and transmitted wave pulse and (b)Lagrangian diagram for the P-SHPB ……27

Figure 3.5 Picture showing (a) Experiment set-up of Penetrating split Hopkinson pressure bar (b) Nicolet data acquisition system with display of typical strain wave ……29

Figure 3.6 Integrated operational layout of the penetrating split Hopkinson pressure bar (P-SHPB) system ……30

Figure 3.7 (a) Variation of striker impact and penetrator velocities with compressor Air Pressure (MPa) and (b) variation of incident bar penetration energy with striker velocity ($V_{pb}=0.0665V_{i,}$ $R^2 = 0.92$, $E_{pb}=0.0271E_{i,}R^2=1.0$) ……33

Figure 4.1 Variation of (a) Crack height and (b) crack length with striker impact energy for Plain woven graphite epoxy composite using 1/4-inch spherical nose penetrator .37

Figure 4.2 Variation of striker bar ballistic limit velocity with sample thickness for three penetrator geometries (a- c) protruding spherical and (b) protruding hemispherical and (d) conical hemi-spherical (The penetrating bar ballistic velocity is $V_{pb}^{BL}= 0.0665V_i^{BL}$) for plain weave specimen ……38

Figure 4.3 Effect of penetrator size on specimen waveform using different sized protruding spherical penetrators ……43

Figure 4.4 Effect of sample thickness and energy absorbed on specimen waveform using 3/16 –inch protruding hemispherical penetrator ……44

Figure 4.5 Effect of sample thickness and energy absorbed on the specimen waveform using 1/4-inch conical hemispherical penetrator ……45

Figure 4.6 Effect of penetrator geometry on specimen waveform using 3/16-inch protruding spherical and 3/16-inch protruding hemispherical ……46

Figure 4.7 Effect of penetrator geometry on specimen waveform using 1/4-inch protruding spherical and 1/4-inch conical hemispherical ……46

Figure 4.8 (a-c) Energy Absorbed – time plot for varying sample thickness (12, 16 24- layer) specimen different sized penetrators (a-c) 3/16, (d-f) 7/32 and (g-I) 1/4-inch protruding spherical penetrator ……51

Figure 4.9 Showing the effect of sample thickness on peak energy absorption by the specimen at the damage threshold (below, at and above ballistic limit) for (a) 3/16, (b) 7/32 and (c) 1/4-inch protruding spherical penetrator ……..54

Figure 4.10 Effect of penetrator size on energy absorbed by the specimens for varying thickness (a) 12-, (b) 16-, and (c) 24-layer ……...55

Figure 4.11 (a-c) Strain rate – strain plot for varying sample thickness (12, 16 and 24- layer) specimen different sized penetrators (a-c) 3/16, (d-f) 7/32 and (g-I) 1/4-inch protruding spherical penetrator ……56

Figure 4.12 Effect of penetrator size on specimen response for varying sample thickness: (a) 12, (b) 16 and (c) 24 layer using different sized penetrator ends (3/16, 7/32 and ¼-inch) ……58

Figure 4.13 Strain rate – strain behavior for different specimen thickness for (a) 12-, (b) 16- and (c) 24-layers penetrated with energy around ballistic limit energy using different sized spherical protruding penetrators (3/16, 7/32 and 1/4-inch) ……58

Figure 4.14 (a-c) Variation of specimen response at the damage threshold for varying penetrator sizes, (d-f) effect of sample thickness on strain rate at the damage thresholds, (g-i) Effect of Impact energy on strain rate ……..60

Figure 4.15 Ratio of strain rate to strain at the damage threshold for varying sample thickness using different sized penetrators ……61

Figure 4.16 Stress-strain response for varying specimen thickness (12, 16 and 24 layer) and penetrator sizes (a-c) 3/16, (d-f) 7/32 and (g-i) 1/4-inch) ……63

Figure 4.17 (a-c) Force- displacement plot for varying sample thickness (12, 16 and24) 24-layer specimen different sized penetrators (a-c) 3/16, (d-f) 7/32 and (g-I) 1/4-inch protruding spherical penetrator ……65

Figure 4.18 (a-c) Variation of sample thickness (12, 16 and 24 layer) on peak loading for different sized penetrators (3/16-, 7/32- and 1/4-inch) ……66

Figure 5.1 Comparison of energy absorption for 3/16-inch protruding spherical and 3/16-inch protruding hemispherical penetrators for 12-, 16-, and 24 –layer specimen at damage thresholds (below, at and above ballistic limit) energies ……68

Figure 5.2 Comparison of energy absorption for 3/16-inch protruding spherical and 3/16-inch protruding hemispherical penetrators for 12-, 16-, and 24 –layer specimen at the same impact energies ……69

Figure 5.3 Comparison of strain rate – strain plot for 3/16-inch protruding spherical and 3/16-inch protruding hemispherical penetrators for 12-, 16-, and 24 –layer specimen at damage thresholds (below, at and above ballistic limit) energies ……71

Figure 5.4 Comparison of strain rate – strain for 3/16-inch protruding spherical and 3/16-inch protruding hemispherical penetrators for 12-, 16-, and 24 –layer specimen at the same impact energies ……72

Figure 5.5 Comparison of force- displacement for 3/16-inch protruding spherical and 3/16-inch protruding hemispherical penetrators for 12-, 16-, and 24 –layer specimen at damage thresholds (below, at and above ballistic limit) energies ……73

Figure 5.6 Comparison of energy absorption for 3/16-inch protruding spherical and 3/16-inch protruding hemispherical penetrators for 12-, 16-, and 24 –layer specimen at the same impact energies ……...74

Figure 5.7 Comparison of energy absorption for 1/4-inch protruding spherical and 1/4-inch conical hemispherical penetrators for 12-, 16-, and 24 –layer specimen at damage thresholds (below, at and above ballistic limit) energies ……76

Figure 5.8 Comparison of energy absorption for 1/4-inch protruding spherical and 1/4-inch conical hemispherical penetrators for 12-, 16-, and 24 –layer specimen at the same impact energies ……76

Figure 5.9 Comparison of strain rate - strain for 1/4-inch protruding spherical and 1/4-inch conical hemispherical penetrators for 12-, 16-, and 24 –layer specimen at the damage thresholds (below, at and above ballistic limit) energies ……78

Figure 5.10 Comparison of strain rate – strain for 1/4-inch protruding spherical and 1/4-inch conical hemispherical penetrators for 12-, 16-, and 24 –layer specimen at the same impact energies ……79

Figure 5.11 Comparison of force-displacement plot for 1/4-inch protruding spherical and 1/4-inch conical hemispherical penetrators for 12-, 16-, and 24 –layer specimen at the damage thresholds ……80

Figure 5.12 Comparison of force – displacement plot for 1/4-inch protruding spherical and 1/4-inch conical hemispherical penetrators for 12-, 16-, and 24 –layer specimen at the same impact energies ……81

Figure 5.13 Tensile strain release at the damage threshold for 16-layer specimen using 1/4-inch Conical hemispherical penetrator (a) Energy Absorbed and (b) Force – time plot ……82

Figure 5.14 Effect of sample thickness on tensile strain release for (a) Force – time at different impact energies, (b) Force – time at the same impact energy ……83

Figure 6.1 System configurations showing high-speed camera looking into sample holder illuminated by 5kV flash unit via fiber optical cables ……86

Figure 6.2 Crack propagation for 12-layered woven graphite-epoxy specimen below ballistic limit velocity using 1/4-spherical penetrator at 60J Below BL impact energy …88

Figure 6.3 Crack propagation for 12-layered woven graphite-epoxy specimen at ballistic limit velocity using 1/4-inch spherical penetrator at 68 J above BL impact energy 89

Figure 6.4 Crack propagation for 16-layered woven graphite-epoxy specimen below ballistic limit velocity using 1/4-inch spherical penetrator at 68 J ……90

Figure 6.5 Crack propagation for 16-layered woven graphite-epoxy specimen at ballistic limit velocity using a 1/4-inch spherical penetrator at 76 J impact energy……91

Figure 6.6 Crack propagation for 16-layered woven graphite-epoxy specimen above ballistic limit velocity using a 1/4-inch conical hemi-spherical penetrator at 85J BL impact energy ……..92

Figure 6.7 Crack propagation for 24-layered woven graphite-epoxy specimen below ballistic limit velocity using a 1/4-inch conical hemi-spherical penetrator at 180J BL impact energy ……..93

Figure 6.8 Crack propagation for 24-layered woven graphite-epoxy specimen above ballistic limit velocity using a 1/4-inch conical hemi-spherical penetrator at 201J BL impact energy ……94

Figure 6.9 Crack propagations using high-speed video model 220 CCD Camera and a picture of 1/4-inch protruding spherical penetrator (25 psi=54J, 32.5 psi=7 J and 35 psi= 84J of striker impact energies) ……97

Figure 6.10 Crack propagations using high-speed video model 220 CCD Camera and a picture 1/4-inch conical hemispherical-nosed penetrator (25 psi=54J, 32.5 psi=76J and 35 psi= 84J of striker impact energies) ……98

Figure 6.11 Comparison of average crack speed around the ballistic limit energies for conical hemispherical and protruding spherical penetrators ……..99

Figure I.1 Complete layout of the Hopkinson bar apparatus ……103

Figure I.2 Hammer assembly ……104

1.0 INTRODUCTION

Composite materials are gaining wide acceptance in many industrial applications due to their high strength to weight ratio. Composite materials consist of two or more materials alloyed together to form a component which when used for the specified application gives stronger and better components than when used independently. Their advantages include: high corrosion resistance, better appearance, stiffness, low density, and high strength to weight ratio are among many of its benefits. Of special interest is their use in application such as design of weight efficient; aircrafts, automobiles, space shuttle and structures [1-6].

The response of composite material to dynamic impact loading is of utmost importance [7-10]. In the design of aeronautic structures, the major concern ranges from flying debris [10-12] to bird strikes. Studies showed that major sources of low impact velocity damage to aircraft are tool dropping during maintenance, mishandling of parts and improper storage can cause severe damage and significant loss of strength [8, 10-12]. Composite materials do not respond to impact loading the same way as metallic structures do.

Several researches have been carried out to understand material failure under dynamic loading, energy absorption of laminated composite plates. Composite are mostly made from lamination of fibers, this makes them highly susceptible to impact loading when they are subjected to one. [13-16].

Studies have revealed that energy expended in damage process is proportional to the thickness of the composite plate and the specimen's impact perforation resistance depends

largely on its thickness [5, 9, 17]. The damage sustained including the energy absorbed is not linear function of impact velocity. Recent studies [8, 19] also revealed that as impact energy is increased rate of energy absorbed decreases and damage profile at higher velocity tends to be different for low velocity impact. The target thickness was also found to play an important role in the energy absorption/dissipation of the composite target material [8, 10].

Akil, Yildrin, Guden and Hall [18] performed an experiment to study the effect of compression behavior of woven fabric S2-glass fiber reinforced vinyl ester composite. The studies were conducted both quasi-static and high strain rate using split Hopkinson bar. The specimen was subjected to both in plane and through thickness loading; typical stress-strain plot for both situations shows a linear and non-linear behavior. The study also shows that average failure stress increases with increasing strain rate from quasi static to high strain rates. While average failure strain decreases with increasing strain rate. This is a good experiment and some their findings correlated with some of our result, the information of penetrator used was lacking, which made the application limited. It would have been nice if the projectile size were varied with the view of determining if the material response behavior would be the same for an increase or decrease in contact area of the projectile to the specimen target.

Sjoblom and Hartness [19] presented a report on low impact testing of composite materials using an instrumented pendulum. Even though the idea of using force history for specimen damage characterization was good, the inability to accurately impact and rebound velocities is a major set back for the method adopted. Their study also revealed that the presence of matrix cracks does not affect the overall laminate stiffness during a dynamic impact event.

Zavattieri [20] conducted a research to study the energy dissipation in ballistic penetration of fiber composites. In their research two configurations were studied: Direct

Penetration where the penetrator approaches the composite specimen and Reverse Penetration where the composite specimen approaches the penetrator. Their experimental result was compared with numerical simulation. The analyses predict a 60m/sec higher peak velocity value, which reduces sharply after the peak value is reached. However, because of high velocity of the penetrator to the specimen and vice versa, to characterize the damage propagation of the composite specimen in this experiment is very difficult, hence the data might not be reliable for design considerations, more so, if the part will be run at its threshold velocity (which is the velocity that has to be exceeded before damage can occur).

Khan, Colak and Centala [21] studied the failure mode of S2-glass reinforced polyester thick laminate using a modified split Hopkinson pressure bar called "direct disk impact technique" where the striker bar directly impacts the specimen along various off axis. The strain gages mounted on the specimen provides information about the specimen deformation while the strain gage mounted on the transmitter records the strain-time profile which converted into the specimen stress-time profile. Their study reveals that mechanical response for both circular and square are similar and that woven composites have a higher strength and failure strain along the thickness. Strain rate sensitivity was found to increase with increasing strain rate. Even though the authors varied the sample thickness, it would have been more desirable if the penetrator size and geometry were varied also.

Wen [22-23] developed an analytical equation to predict the penetration and perforation threshold for conical-nose, truncated cone-nose and hemispherical-nose projectiles. The equations were however based on the assumptions that damage to the specimens was localized and the resistances posed by the specimen were both quasi-static and dynamic in nature. This idea seems to be very brilliant, but predicting penetration and perforation based on their model

when it was not applied to other sample thickness seems to be the greatest undoing of this method and also the projectile nose diameter should have been varied to see if the analytical solution would still apply.

Vinson and Woldesenbet [24-25] studied the effect of fiber orientation on a unidirectional IM7/8551-7 graphite/Epoxy Composites. They suggested that studying individual constituents and interface of composite material and also the mode of failure at different strain rate on different off-axis orientation are necessary so as to be able to predict the composite material behavior under dynamic loading. Their off-axis loading direction was from 0 (longitudinal) to 90 (transverse) with 15 degrees increment on the test direction. Their result shows a decrease on ultimate strength as the off-axis angle increases and that 60 degrees is the plane of maximum dynamic shear stress. While this research can be regarded as very educative and instructive varying the configuration of the penetrator and comparing them at the same off-axis would have been desirable.

Rodriguez et al [26] performed an experiment to determine the influence of strain rate on the mechanical properties on aramid and polyethylene woven fabric. These authors found that changes in tensile strength and failure strain are similar to the conventional materials. From the author's point of view the linear relation assumed for this materials were not supported by the experimental result obtained. However, the author did not quantify the effect of energy absorbed by this specimen as related to the conventional materials using different specimen thickness to validate the hypothesis.

An experiment was performed on impact resistance of glass/epoxy having different stacking sequence and thickness [14]. Using different impactor sizes, they were able to determine the penetration threshold and perforation threshold velocity of glass/epoxy laminates

based on whole energy analyses. Their result indicated that increasing the impactor size results in a significant increase in the penetration threshold and perforation threshold. They reported that equal energy range, i.e. transition from penetration to perforation was proportional to composite specimen thickness and thicker specimens were found to more efficient in energy absorption than the thinner ones. This experiment though carried out in quasi-static condition, showed that some of the result seems to agree with my findings in my report in dynamic case.

Shivakumar, Elber and IIIg [27] using a transversely isotropic graphite/epoxy composite with spherical-nosed impactor predicted the impact force and duration due to low velocity using the energy balance and spring mass method. They found out that energy balance predicts the maximum force while spring mass gives a whole complete history of the force. This idea is novel in itself but since it does not take cognizance of other penetrator size and geometries their application could be said to be limited.

However, limited research has been conducted on the effect of penetrator size and configuration on the dynamic behavior of woven composites. Because woven composites have a high complex microstructure and they are new generation material, there are limited experimental and analytical data in characterizing their behavior under dynamic loading condition. Thus, the objective of the present study is to investigate the effect of penetrator configuration and size on the dynamic behavior of composite materials under high strain rate using Hopkinson bar. Modes of failure of composite material subjected to different penetrator configuration are expected to be different. While some will indent, penetrate and perforate at lower energy others will require higher energy for the same level of failure. This thesis would involve the use five different penetrators with three different configurations namely: protruding spherical (3/16, 7/32 and 1/4-inch) penetrator ends, protruding hemispherical (3/16-inch) and

conical hemispherical (1/4-inch). Also three-sample thickness will be studied namely: 12-, 16-, and 24-layer

The solution to these problems is organized as follows: Theoretical formulations, which is based on the classical wave theory and have been reviewed by many authors (see reference 1-2, 13) is presented in Chapter 2. Chapter 3 presents the experimental setup, the penetrating split Hopkinson pressure bar installed is a modified fashion of the one installed by Nwosu [5]. This chapter also covers brief description of the Hopkinson bar operation and whole system calibration curve. In Chapter 4, the damage threshold (below, at and above ballistic limit) of each specimen is experimentally determined using different penetrator size and configuration. The experiment is repeated at the same striker impact energy for each sample thickness while varying the penetrator size (in the case of protruding spherical). The wave generated is recorded and analyzed using computer software with view of characterizing the specimen response in terms of energy absorption rate, strain rate – strain, force-displacement history. Chapter 5 illustrates the effect of penetrator geometry on specimen response. The experiment is repeated as above but this time varying the penetrator geometry (protruding spherical, protruding hemispherical and conical hemispherical). The 3/16-inch protruding spherical and 3/16-inch protruding hemispherical penetrator damage profile were characterized. Also, 1/4-inch protruding spherical was compared with 1/4-inch conical hemispherical penetrator. Chapter 6 covers the measurement of crack propagation using high speed imaging video camera (model 330 and 220) manufactured by Cordin Company. While Chapter 7 presents the conclusions made from the research.

1.1 Various Test Techniques Used for Composite Material Testing

1.1.1 Hydraulic machine test method

This method has been applied to metal testing to measure its tensile strength. The hydraulic machine usually consist of chuck or holder at both ends, this is used to grip the ends of the material to be tested. The test piece end are fabricated (usually vee end is recommended) in such a way that it can fit into the holder without slipping. Tensile force is applied to the ends of the specimen pulling it apart. The specimen's strain history can be collected by the aid of strain gauge bonded to the specimen over wide range. This method is however limited because of the geometries of the specimen which can not be adapted to the type of shock loads that a material will be exposed to in the real life. Also, this method appears not to be as effective as when the compressive strength of the material is to be determined.

1.1.2 Izod Method

This method involves a test piece clamped up to the half of its length with a notch carefully grafted on the specimen [28]. The specimen is then impacted on the opposite side of the notch by a swinging pendulum towards the upper end of the specimen. The stress generated around the notch area is not accounted for in this experiment.

1.1.3 Charpy Method

The Charpy method is typically applied to thick section specimen. One of the advantages of charpy method is that its instrumentation is easy to achieve. The specimen is supported at both ends horizontally. A notch is grafted at the mid point of the specimen; this is impacted directly

opposite the notch by a swinging pendulum. The strain gauge mounted on the pendulum records all other valuable data which when analyzed can give the force-time history as well as the energy absorbed by the specimen during the impact test. This method is typically limited to short but thick specimen, which is at variance with engineering applications [17]. Because of the destructive nature of the experiment, characterizing what happened to the specimen just before failure is not possible. Hence, if it is used for design consideration it might lead to over estimation or over concentration of the material. This method does not provide an accurate strain-time history and data can only be collected at a single point which makes its application to dynamic testing materials limited [27].

1.1.4 Drop Weight

Most low velocity impact test is undertaken by using this method [12, 28, 29]. Drop weight allows many specimen geometries to be tested and can be adapted to complex specimen geometries. Basically, this method entails free weight to be dropped from a measured height unto an object. The specimen deformation depends on the size of the hammer, and the impact velocity. The velocity can be measured via an optical gate mounted just before the impact and the specimen displacement also can be determined using a displacement transducer.

1.1.5 Gas gun method

This is a high strain rate testing method. It consists of a gas gun, chamber, and target plate. The experiment could be set up as a direct penetration setup (penetrator approaches the plate) or reverse penetration method (plate approaches the penetrator)[30]. A pressurized gas in a chamber is used as a driving force for the gas gun. Impact velocity can be measured by a optical

gate device just before impacting the target. However, because this method involves high velocity testing, strain rate data, which is very important data used to characterize the damage history of the specimen, is nearly impossible to get from this type of experiment.

1.1.6 Hopkinson Bar

Hopkinson bar is mostly used for dynamic testing of material at high strain rates. This bar was named after the inventor (Hopkinson) Kolsky [31] performed many experiments using the Hopkinson bar. Many researchers have modified this bar since then [5,13, 32]. The one used for this experiment consist of two bars referred to as Incident and Transmitted bar, striker rod, Pressurized impactor ram, quick acting solenoid switch, modified test section, strain gauge, Pro 42 Oscilloscope, High speed camera (records the speed of crack propagation) and a trigger switch. Basically, the striker rod impacts the incident bar a uniaxial wave is generated between the bar/specimen interfaces. Some of this compressive wave is reflected back as a tensile wave while some pass through the specimen into the transmitter bar as a transmitted wave. The stress wave generated is amplified before it is recorded on the oscilloscope. The force/time and energy absorbed by the specimen is gotten from the analyzed wave. The advantage of the Hopkinson bar is that the experiment can be controlled because the impact is at low velocity and the speed at which bar travels can be regulated via the pressure controller compared to the gas gun method.

Various shaped penetrator configurations will be studied with the aim of characterizing their damage generation with particular references to energy absorption, damage profile on the fiber orientation and crack propagation. The anisotropy characteristics of composites, the fabrication process and the damage resulting from slight impact are what made testing composite material more difficult to test as compared to the conventional materials. High fiber content in

the woven fabric for impact protection further increases all these factors. Hopkinson bar will be used for these experiments to generate high strain rate damage. The technique, which is based on the classification of wave propagation analysis, and determination of stress and strain in the specimen, rests on the hypothesis of equilibrium within the specimen.

The aim of this research is to provide a reliable data on the effect of high strain rate on longitudinal compressive strength and failure strain using different penetrator shapes to initiate the damage. The energy absorbed by each specimen using different penetrators will be characterized with the aim of establishing which penetrator configuration impacts the most energy to the target plate.

2.0 THEORETICAL FORMULATION AND DATA REDUCTION PROCESS

The basic assumptions for the validation of Hopkinson bar to characterize specimen damage have been studied and documented by many researchers and authors [1,2, 5-6, 22] amongst others. The assumptions are as stated below:

1. The stress is one-dimensional and uniaxial over the cross sectional area of the specimen. Slenderness ratio of the Hopkinson bar used is 1/144.
2. Wave is non-dispersive
3. Composite plate is elastic and its properties remain unchanged by the impact energy.
4. Transverse strain, inertia, lateral and body forces are negligible
5. State of stress at any instant is homogenous and in equilibrium throughout the composite plate deformation process.
6. Specimen is flexible and sample strain is much greater than total strain of the bar.
7. At any point in the material the state of stress is homogenous over the entire plate

2.1 Data Reduction Process.

Nwosu [1997] and many other researchers [1, 2, 33] have done extensive work in deriving equations used for the experiment, which are based on classical wave theory. Some of their derivations will be presented here since the Hopkinson bar experiments are still based on

assumptions and equations. For this experiment, a striker bar of length L_{str} released from a preset pressure (P) and ram length I_R to impacts the incident bar thereby creating a compressive stress wave, which traveled through the length of the incident bar to the bar/specimen interface. At the interface, part of the wave will be reflected due to impedance mismatch of the bar and specimen while some will be transmitted through the specimen. Many reflections can occur if the wave-transit time in the short specimen is small compared to the loading pulse. We can therefore assume a uniform stress and strain along the specimen. Strain measurement on the specimen is achieved by the strain gauges mounted on both bars. This is integrated to get the force-time parameter and other relevant data on the specimen can be deduced from integration result.

The uniaxial stress generated during the impact process could be given as:

$$s(t) = \frac{F_0}{A} = (rC_0)V_p(t) \qquad 2.1$$

F_0= Longitudinal load of the striker rod for time interval dt

A = Area of the bar

r = Density of the striker rod

C_0= Wave velocity

$V_p(t)$ = Particle displacement velocity = $\frac{du}{dt}$

U(t) = Particle displacement expressed as [5,34]

$$U(t) = \int_0^t V_p(t)dt = \frac{1}{rC}\int_0^t s(t)dt \qquad 2.2$$

$$rC = \frac{E_0}{C_0},$$

therefore

$$U(t) = \frac{C_0}{E_0}\int_0^t s\,(t)dt \qquad 2.3$$

Thus, from Equations. (2.2) and (2.3), the net specimen displacement is given as:

$$u_n(t) = \frac{c_0}{E_0}\int_0^t [s_i(t) - s_r(r) - s_t(t)]dt \qquad 2.4$$

where s_i, s_r, s_t are incident, Reflected and transmitted stress respectively.

The specimen displacement due to the interaction of compressive and tensile waves in the sample. The specimen's strain is e_s (t)= u_n (t) /L_e) and since s (t) = $E_0 e$ (t), the sample strain and strain rate using bars of the same cross section area can be expressed (Nwosu) as:

$$e_s(t) = \frac{c_0}{L_e}\int_0^t (e_i(t) - e_r(t) - e_t(t))dt \qquad 2.5$$

and

$$\frac{d\,e_s(t)}{\partial t} = \frac{c_0}{L_e}(e_i(t) - e_r(t) - e_t(t)) \qquad 2.6$$

respectively.

L_e= Effective length of the specimen

where e_i, e_r, e_t are incident, reflected and transmitted strain respectively

2.1.1 Determination of Energy absorbed parameters

Net energy released by the striker bar and carried by the compressive wave to the specimen/bar interface can be given by:

$$E_R = \int_0^t F_i(t)\,du_n \qquad 2.7$$

where F_i (t) = A (s_i (t) + s_r (t)) is the net compressive loading force and du_n is the net plate displacement.

Integrating the force-displacement curve over the wave duration (0 to t) will yield E_R. Substituting equation 2.10 into 2.13 will give curve below:

$$E_R = \left(\frac{Ac_0}{E_0}\right)\int_0^t [\,s_i(t)^2 - s_r(t)^2 - s_t(t)^2\,]dt = \Delta E_{abs} + \Delta E_s \qquad 2.8$$

ΔE_{abs} = Energy absorbed by the specimen

ΔE_s = Energy absorbed by the system

The equation 2.8 gives the total energy absorption curve and represents the net energy to be expended for perforation process, since energy lost by the penetrator is equal to the energy absorbed by the specimen [Nwosu, 2002] plus other losses. For the wave to be under the condition, it was shifted to begin at zero and also ending at the same time. The numerical integration of the wave is thus carried out.

Nwosu expressed Equation 2.8 as the net energy lost by the incident compressive wave, i.e, $E_A = E_i - E_r - E_t$, where $E = (Ac_0/E_0)\int s^2 dt$ and can be written for incident (E_i), reflected (E_r) and transmitted (E_t) energies. Following energy balance, the energy absorbed by the composite plate and all competing processes is presented [Shivakumar et al. 1984] as:

$$E_A = (E_c + E_b + E_e) + (E_d + E_f) \qquad 2.9$$

In a typical perforation test, the penetrator emerges through the plate of thickness (L_s) to the maximum distance, $d = L_s + \chi$, where c can be either the distance the penetrator travels beyond the plate during punch-through, or the height of the damage cone above the rear surface of the laminate. For a negligible plate deflection and energy losses, Nwosu [13,34] expressed the total energy delivered by the penetrator for the process as:

$$E_R = \frac{1}{2} m_b V_{pb}^{\ 2} = \int_0^d P(x)\ dx = \int_0^{L_s} P(x)dx + \int_{L_s}^d P(x)dx \qquad 2.10$$

where V_{pb} is the penetrator critical penetration velocity or "ballistic limit" velocity, m_b is the mass of the input bar, and $P(x)$ is the penetrator point contact force exerted on the plate. The functional dependence of $P(x)$ on depth of penetration x can be represented by appropriate contact force model for the regions of interest. The second term in Equation 2.10 is the work done in the penetrator head traversing through a distance, $c = d\text{-}L_s$ above the plate.

Change in kinetic energy of the incident bar and the residual energy is derived from equation 2.10 and is given by

$$E_r = \frac{1}{2} m_b V_r = P_c c \qquad 2.11$$

$$V_r = \left(\frac{2}{m_b} P_c c \right)^{1/2} \qquad 2.12$$

where V_r= residual velocity.

Wen [20,21] developed a model to predict the ballistic limit for composite specimen using different penetrators based on the energy relationship:

Hemispherical

$$V_{bl} = \frac{3p\sqrt{r_t s_e D^2 T}}{8G}\left[1+\sqrt{1+\frac{32G}{9p r_t D^2 T}}\right] \qquad 2.13$$

Conical

$$V_{bl} = \frac{p \sin\left(\frac{q}{2}\right)\sqrt{r_t D^2 T}}{2G}\left[1+\sqrt{\frac{2G}{p \sin^2 \frac{q}{2} r_t D^2 T}}\right] \qquad 2.14$$

2.1.2 Sample Stress Measurement

At the instant of the striker rod on the incident bar a transfer energy occurs which travels to the specimen/bar interface. The particles in the incident bar will propagate to the right at a relative velocity of V_b in the longitudinal direction of the wave pulse. A specimen of cross sectional area A_s is sandwiched, between the incident and transmitter bars of cross sectional area, A_b.

For equilibrium and continuity of forces at the interfaces;

$$F_I = (\sigma_i+\sigma_r)A_b = F_{ts} = (\sigma_t)A_s \qquad 2.15$$

Where F_I= Force at the incident/specimen interface

F_{ts}= Force at the specimen/transmitter bar interface and

$$V_I = V_i - V_r = V_s \qquad 2.16$$

Combining equation (2.1, 2.15 and 2.16) particle velocity is expressed as [34]

$$V_s = \frac{C_0}{E_0}(s_i - s_r) \qquad 2.17$$

and sample stresses at the incident bar/specimen and specimen/transmitter interfaces are:

$$s_I(t) = \frac{F_I}{A_s} = \frac{A_b(s_i(t) + s_r(t))}{A_s}$$

$$s_O(t) = \frac{F_o}{A_s} = A_b s_t(t) \qquad 2.18$$

where A_s *is* the specimen cross sectional area. Thus, the average sample stress is the mean of the stresses at the interfaces, i.e.,

$$\sigma_s(t) = \frac{1}{2}(\sigma_I + \sigma_O) = \frac{1}{2}\frac{A_b}{A_s}(\sigma_i + \sigma_r + \sigma_t) \qquad 2.19$$

Assuming uniform stress through a thin specimen, $\varepsilon t(t) = \varepsilon_i(t) + \varepsilon_r(t)$ and

$\sigma_t(t) = \sigma_i(t) + \sigma_r(t)$. Substituting into equation 2.26 we have the sample stress to be:

$$\sigma_s(t) = \frac{A_b}{A_s} E_0 \varepsilon_t(t) \qquad 2.20$$

respectively. Equation 2.20 shows that stress is proportional to strain as expected. The elastic Young's modulus, E_0, is applied when the magnitude of the stress is less than the yield stress of the material. In the general case of yielding, Nwosu [5,13,34] have retained the dynamic *modulus of elasticity* as the ratio of ultimate yield stress to corresponding yield strain. Plastic deformation of a material subjected to uniaxial stress occurs at a stress level above the yield stress of the material, while the rapture of the material occurs above its *ultimate strength.* Thus, when the stress-strain curve is composed of elastic and plastic portions, the elastic modulus is determined as the slope of the straight-line portion of the stress-strain curve in the limit of small strain interval [13,34].

3.0 EXPERIMENTAL SETUP

This chapter will describe in detail the experimental equipment and processes used to conduct this research. Since this is the first time for this experiment to be performed at the University of Pittsburgh, this section will be devoted to describing in detail the setup since. The set-up consist of the following:

3.1 Base Support

The base support is divided into two sub assemblies namely the upper and lower supports. The lower assembly consists of: 6 base plates, 6 I- beams and 6 rectangular top plates. The base plate has 6 holes of 3/4-inch diameter spaced at 48-inches apart drilled into it. This is used to attach the equipment to the floor for rigidity purposes. An I-beam of 24-x 8- x 8-inches was welded on top of the base plate (for elevation purposes, any height can be chosen), The top plate (8- x 8-x 8)-inches rectangular plate was welded on this I-beam with four 0.8-inch diameter holes to connect the lower to upper support. This done to allow for easy dismantling of the whole system should there be need for it to be transported.

The upper section consists of six I-beam of 60-x 8-x 8-inches. Four holes of 3/4-inch were drilled at the center of each beam (two holes on each side of the beam used to fasten the upper section to the lower section) with the aid of the top plate. Also, 12 holes of 3/4-inch (6

holes on each side of the beam) were drilled on the top of the I-beam. This is used to hold the whole experimental equipment in place. Also there are 16 holes of 3/4-inch drilled on the both sides of the beam (with exception of the two end beams which has 8 holes only on the end). These holes allows the beams to be joined together so that the whole assembly will extend to 30 feet needed for all other accessories to be mounted on top of the I-beam. They are connected together with the aid of 36-x 6-x 3/4-inches thick flat plate that has 16 holes drilled on each of them. These holes are made to match the ones on each end of the I-beam for sturdiness and rigidity purposes. All the assemblies are fasten together with different sized bolts and nuts.

3.2 Alignment Flat Bar

Figure 3.1 shows the alignment flat bar. The alignment flat bar is in two sections, to support the following parts namely: incident and transmitter bar. They are 123- x 5-x ½-inches thick with 8 holes of ¾-inch diameter drilled into it to hold the incident and transmitter bar in place. The purpose of this plate as the name suggest is to compensate for any transverse and longitudinal misalignment during installation. Of outmost importance is for both incident and reflected bar to ride smoothly on their Teflon bearings, hence the need for straightness on the surface which they are mounted need not be emphasized. This will reduce and or eliminate any distortional effect on the experiment, which might render the experiment data invalid.

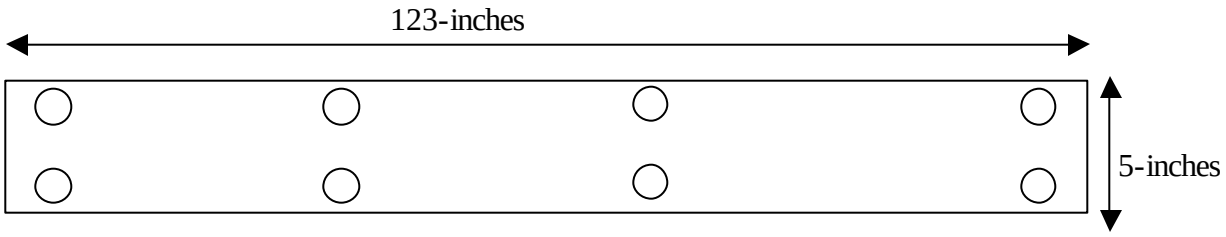

Figure 3.1 Showing typical alignment flat bar for both incident and transmitter bar

3.3 Hammer Assembly

The hammer assemblies consist of: Quick acting solenoid valve, air cylinder, striker rod and pull rod or retractor pin.

i). Figure 3.3 presents the picture of the whole Hopkinson bar setup with the modified sample holder. The advantage of the fast acting solenoid valve is that it allows a preset amount of air stored in the cylinder to pass through it when the switch is closed during operation. This pushes the striker bar towards the incident bar to impact it. The specimen is sandwiched in between the incident bar and a transmitter bar in a sample holder (see Appendix I for the detailed drawing of the Hopkinson bar setup and the hammer assembly).

(ii). Some amount of air for the compressor is stored in the cylinder, this air, which is stored as a potential from the compressor, is introduced at the back striker rod to give the striker rod a kinetic energy to move. The speed of the striker rod depends on preset compressor pressure for the experiment.

3.4 Striker Rod

The striker rod impacts its kinetic energy into the incident bar. The one used for this experiment is 610mm (24-inches) long x 6.35mm (1-inch) diameter. The contacting end is rounded so as to be able to impact the incident bar effectively. A retracting rod of 610m long x 6.35mm diameter is bolted into the striker rod at the other. This is used to pull back the striker rod to the desired ram length during an experiment.

3.5 Design of Penetrator

Figure 3.2 shows the picture of the three protruding spherical penetrator, one protruding hemispherical and conical hemispherical used for this study. Since studying protruding spherical penetrator was the primary focus for these experiment, three types of protruding spherical penetrator were fabricated for the experiment, and they are: 0.1875-inch (4.7625mm), 0.2188-inch (5.5563mm), 0.25-inch (6.35mm). These penetrators were made out of maraging steel, the rear end outer diameter is 1.5-inch x 1-inch long (38.10mm x 25.4mm long respectively), an internal diameter hole of 1-inch x 1-inch (25.4mm x 25.4mm) was drilled and recessed so as allow the penetrator to sit properly on the incident bar when coupled to reduce mismatch effect between the incident bar and the penetrator. The conical end is 0.5-inch (12.7mm) long with the protruding end extending 0.20, 0.19 and 0.14-inch long respectively. The protruding section allows the specimen deformation to be achieved by not allowing the conical section take part in specimen failure response. The spherical shaped end is (0.1875-inch) in diameter for this case.

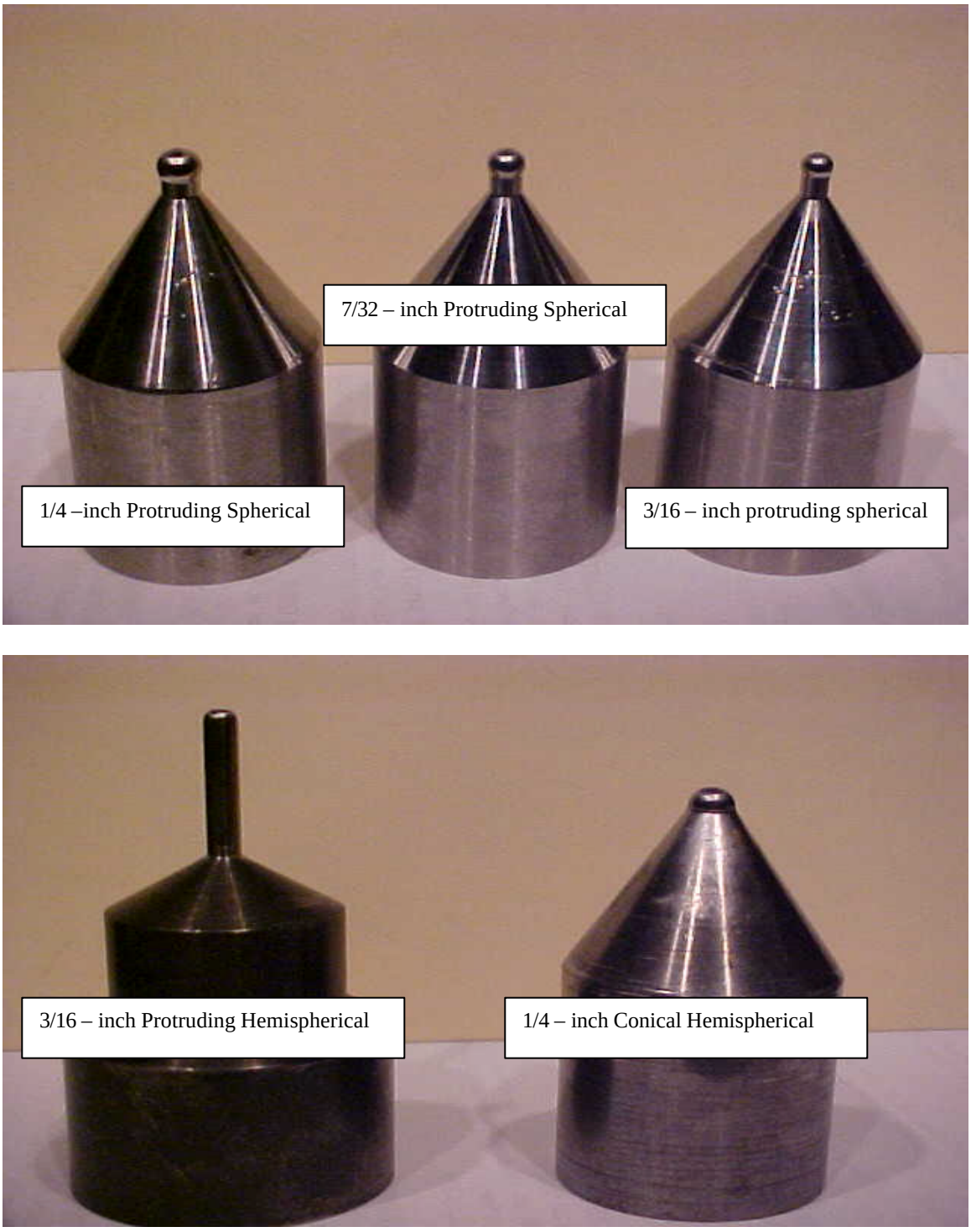

Figure 3.2 showing different penetrators geometries and sizes

The total length of the penetrator is 72.64mm (2.86-inch) long. This geometry is typical for all the protruding spherical penetrators except for the spherical ends, which were 4.76mm

(3/16-inch), 5.56mm (0.2188-inch) and 6.35mm (0.25mm) respectively. The conical hemispherical configuration is typical to the one described above except for the absence of the absence of the protruding section. The protruding section for the protruding hemispherical is 18-inches long and the tip is 0.1875mm in diameter.

For clarity purposes each of the penetrator behavior will be discussed separately and effort will be made at the end of each specimen behavior report to compare and contrast so as to arrive at a reasonable conclusion.

3.6 Brief Description of Hopkinson bar Operation

Hopkinson bar is mostly used for dynamic testing of material at high strain rates. This bar was named after the inventor (Hopkinson) and has since been modified by many other researchers [5,6,34] amongst others. The one used for this experiment consist of two bars (incident and transmitted bar), striker rod, Pressurized impactor ram, quick acting solenoid switch, modified test section, strain gauge, Pro 42 Oscilloscope, High speed camera (records the speed of crack propagation), Pulse amplifier and a trigger switch. These are all instrumented together to be able characterize the damage in a specimen.

The operation of the split Hopkinson bar (SHPB) has been documented by a lot of researchers, [1,5,6,34]. It is not the intention of this author to bore the readers with all the details as this can be gotten from the references sited above and some other referred dynamic studies journals. However, areas that are relevant to this experiment will be mentioned. Hopkinson (to whom the bar was named after) was the first researcher to perform experiments involving stress wave [5]. Kolsky also performed more experiment using Hopkinson bar to generate a dynamic stress waves in material. In his experiment he sandwiched a specimen in between the incident bar

and transmitter bar. The incident bar is impacted by an external force through the striker bar, a uniaxial compressive wave is generated, this wave continues down length of the bar to specimen interface, part of it is reflected as tensile wave and the rest is transmitted through the specimen as compressive wave. This wave is recorded through the strain gages mounted on both bars in form of a wave pulse on the digital oscilloscope used for this experiment. The specimen's mechanical response to high strain rate compressive loading and its resistance to impulse loading can be deduced from the analyzed wave.

Material response to impulse loading can also be characterized using this system, which will help in material selection for a component parts. Because the wave recorded on the oscilloscope after the impact carries all the information about the specimen damage, which is analyzed by the use of computer software. Speed of crack propagation can be calculated from the film recorded by a high speed model 330 camera from Cordin company. This high-speed camera is capable of recording 2 million frames per seconds (mfs) thus allowing the event before and after specimen deformation to be measured from the film developed.

Figure 3.3 (a-b) shows the test section and the experimental setup, the test section of the Hopkinson bar was modified to include a penetrator and a specimen holder. The advantage of this method is that, we are able to capture the crack propagation through a high-speed camera and characterize the damage profile using different projectiles. Because of the low velocity penetration process made possible by the Hopkinson bar, damage process can be controlled. Controlling the damage process has been very difficult using the ballistic test method because of the high speed [32].

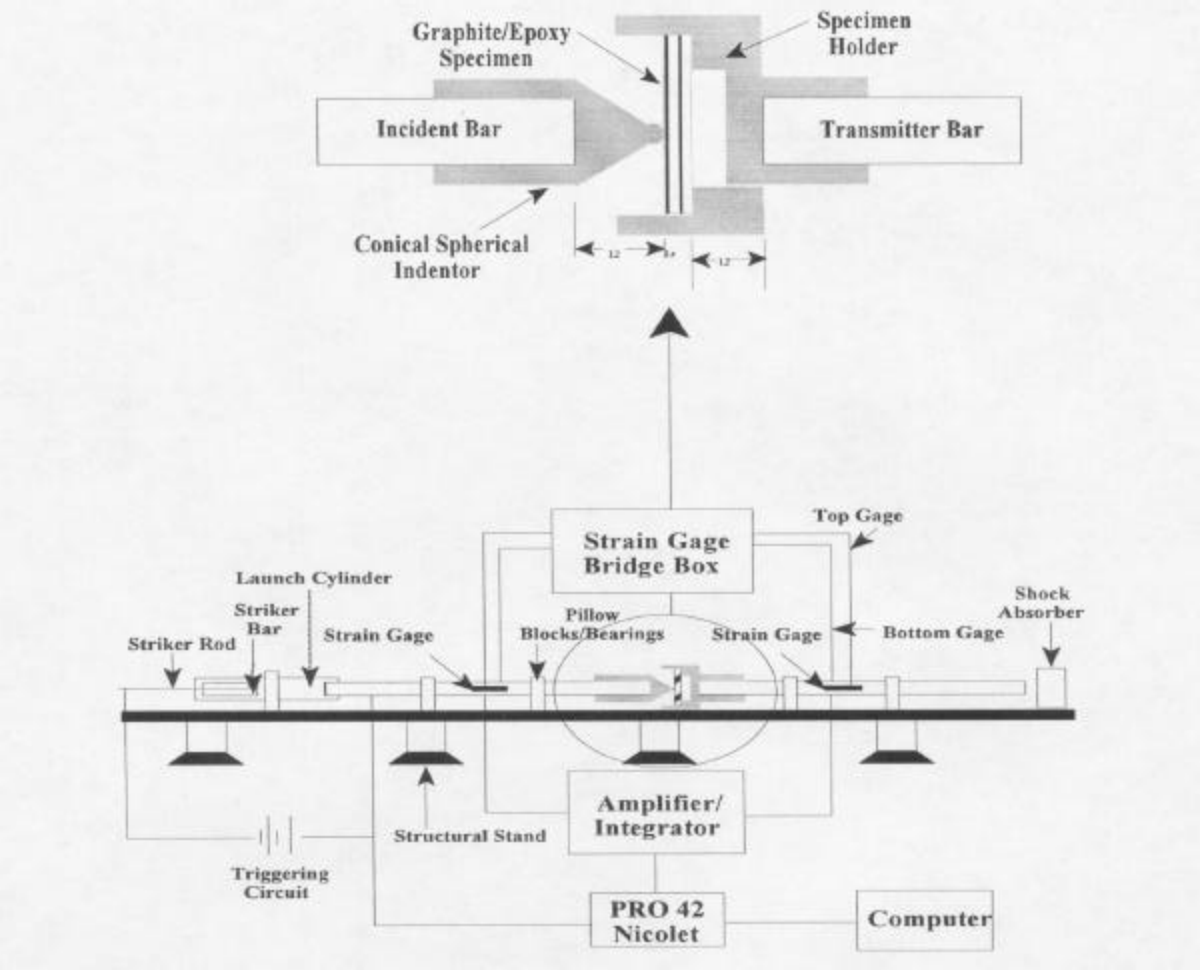

Figure 3.3 a schematic diagram of the penetrating Hopkinson pressure bar system showing (a) Perforation sample holder fixture (b) system configuration and instrumentation.

The incident and transmitter bars are made from 300-maraging AMS steel. They are 3.66m long (144inches) x 0.0254m (1-inch) in diameter. Maraging steel was chosen because it is a little bit harder than ordinary steel, hence it can be used to studying the dynamic loading effect on steels without altering the stress wave generated. The striker rod is 0.6096m (24-inches) long and is housed inside a 1.2192m (48-inches) launch cylinder driven by compressed air of up to 1.6552 MPa (240psi). Figure 3.3b shows the system's configuration, two sets of strain gages were mounted at the mid point (six inches) of each bars to record the stress wave pulse generated

as a result of the impact from the striker bar. These bars ride inside Teflon bearing type housing to reduce the effect of friction.

Figure 3.4 (a-b) shows the picture of typical compressive wave pulse and the Lagrangian diagram for penetrating split Hopkinson pressure bar (P-SHPB). When the fast acting solenoid switch is energized via the trigger button in the instrumentation room, it pushes the striker bar towards the incident bar to impact it. The kinetic energy produced is transferred into the incident bar. This impact generates an elastic strain wave known as incident wave, which is picked up at about 395 microseconds after the impact. The wave continues to travel down the length of the incident bar for another 395 microseconds, upon reaching the bar/specimen interface, some of the wave is reflected back as a reflected wave and some that penetrates the specimen is transmitted into the transmitter bar. The reflected wave is picked up by the strain gage mounted on the incident bar. Some of the reflected wave that travels to the striker/incident bar interface results in the generation of another set of wave as a result of multiple reflections at the specimen/bar interface. Plastic deformations is said to occurs when the induced strain exceed the yield limit of the material, part of this wave will be reflected back at the bar/specimen interface [34]. The specimen is sandwiched in between the incident bar and a transmitter bar in a sample holder (see Figure 3.3a above).

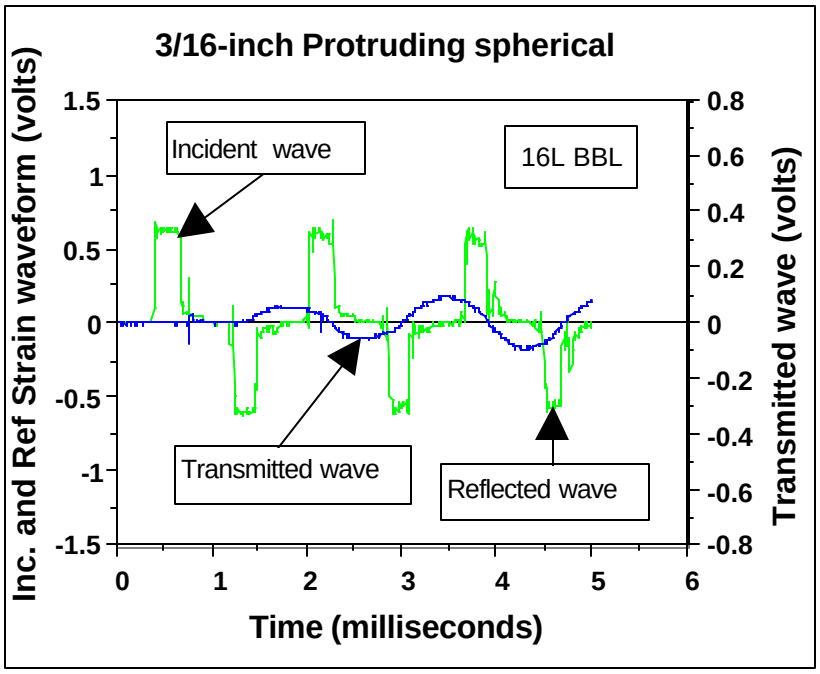

(a)

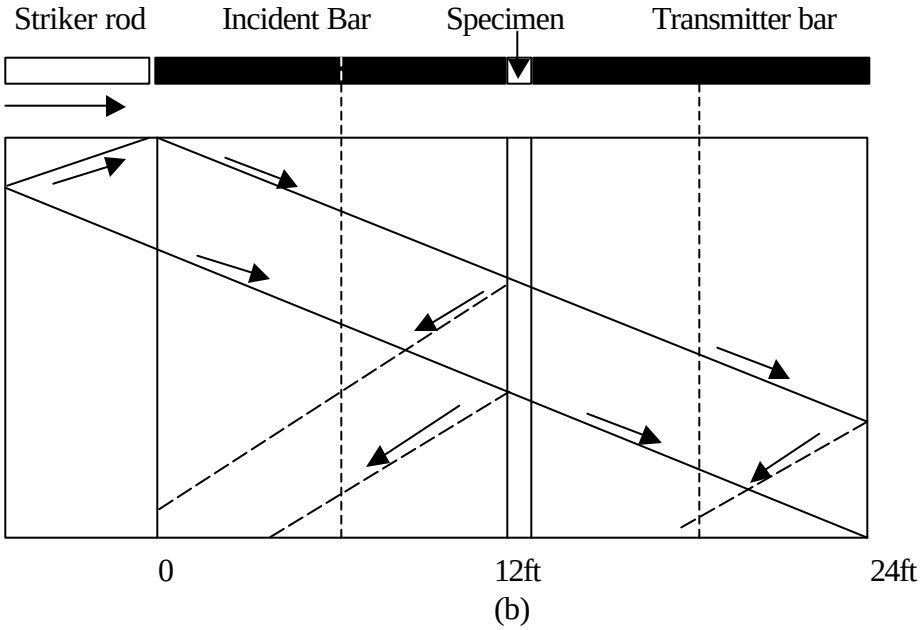

(b)

Figure 3.4. (a) Typical wave showing the incident, reflected and transmitted wave pulse and (b) Lagrangian diagram for the P-SHPB

The compressive stress wave pulse generated is recorded on the oscilloscope via the strain gauges mounted on both the incident and transmitter bar is analyzed through use of

computer software. All the relevant information pertaining to the specimen deformation is supplied by integrating the stress waves generated.

Figure 3.5 (a-b) shows the picture of the experimental set-up of the penetrating Hopkinson bar and data acquisition system. Relevant information was extracted from the analyzed wave and integrated to obtain the specimen responses.

Figure 3.6 presents the layout of the integrative penetrating split Hopkinson pressure bar (P-SHPB), with the continuous rotating high-speed camera, light source, camera control, remote fire unit and its other instrumentation accessories. A trigger activated by the striker bar impact on the incident bar operates the entire system.

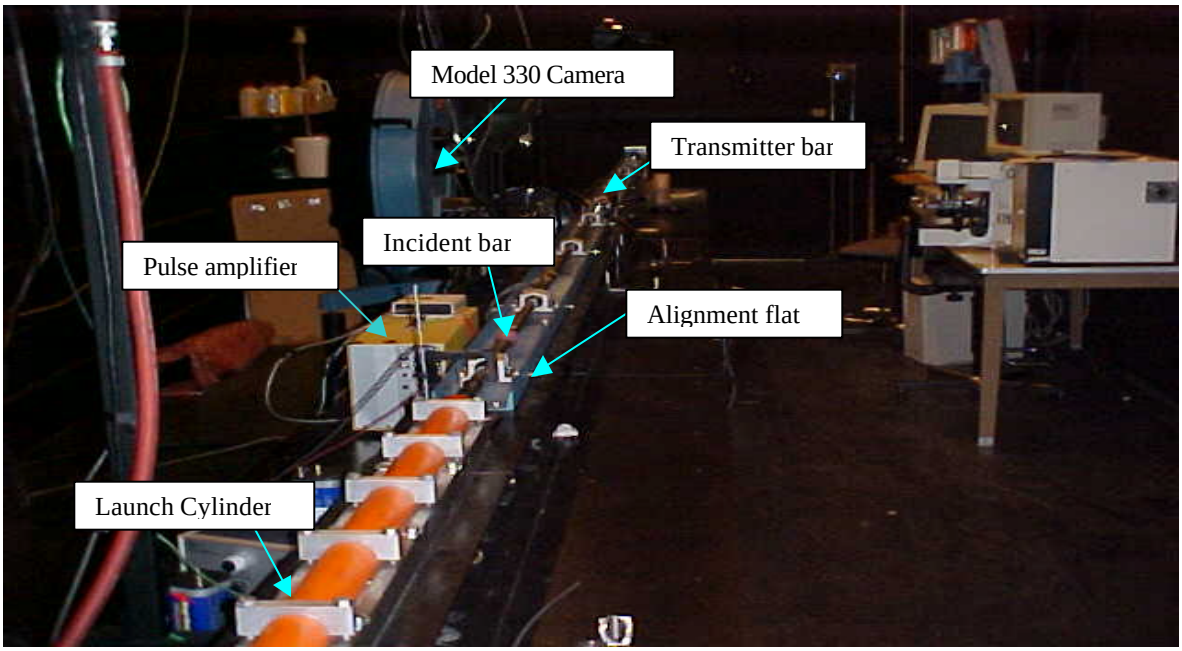

(a)

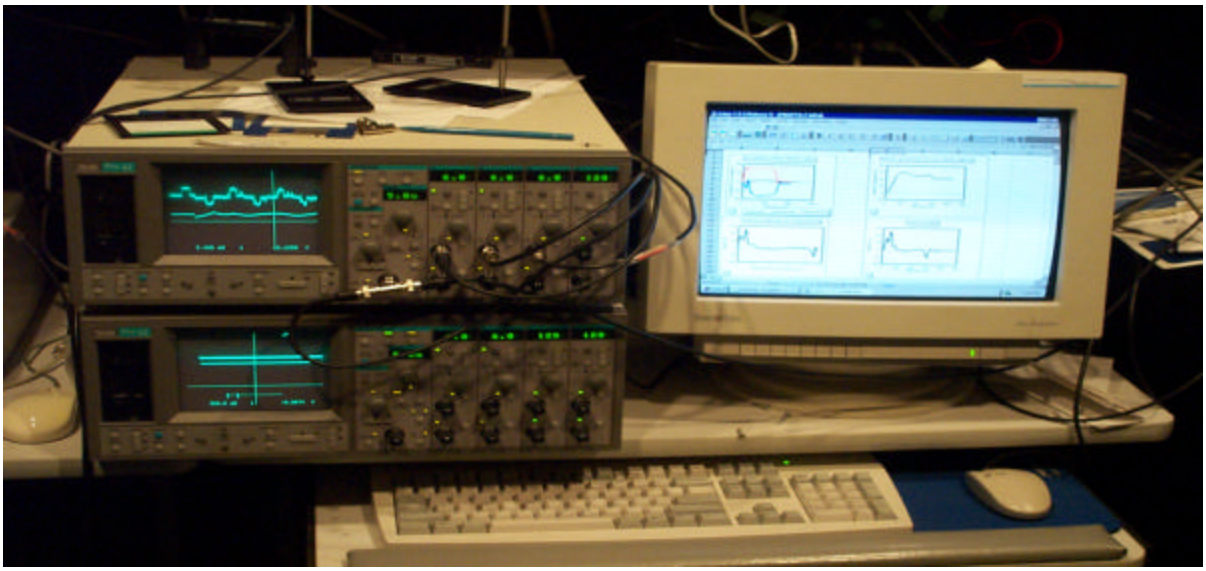

(b)

Figure 3.5 Picture showing (a) Experiment set-up of Penetrating split Hopkinson pressure bar (b) Nicolet data acquisition system with display of typical strain wave

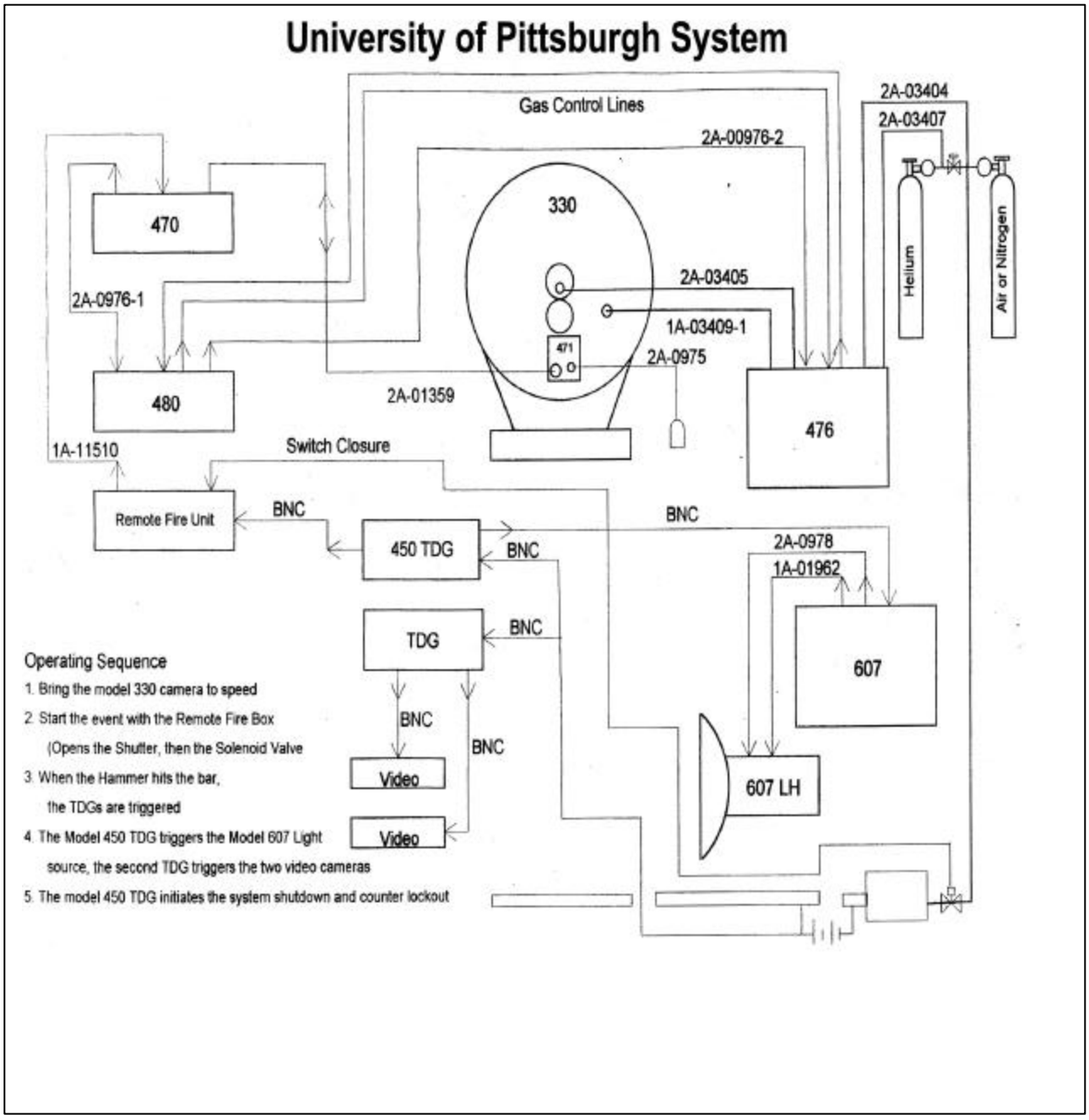

Figure 3.6 Integrated operational layout of the penetrating split Hopkinson pressure bar (P-SHPB) system.

3.7 System Calibration

3.7.1 Striker and Penetrator Velocity (Calibration results)

The objective is to develop a calibration curve and establish a correlation between the (compressor) impact pressure and striker delivered to the input bar and penetrator energy delivered to the specimen. The striker velocity just before impacting the incident bar was measured as a function of impact pressure using two infrared photo gate detectors.

3.7.1.2 Calibration. Two sets of two small flags constructed out of 25.4 mm-inch wide strips of cardboard were attached: one set to the end of the striker bar and the second to the end of the incident bar [35]. The strategic placement of the two infrared photo gate detectors along the split Hopkinson pressure bar system allowed for automatic data collection of the necessary time for the flags to pass through each gate; with the first gate recording the time of the striker bar and the second capturing the incident bar's time. The capture times were automatically converted into velocities using computer software. All other response parameter measurements, excluding impact energy, were taken from the wave analysis.

Figure 3.7 depicts the calibration curves and the empirical equations showing non-linear relationship between the striker and penetrator velocities and pressure. The penetrator attached to end of the incident bar penetrates the composite plate at an initial penetrator velocity, V_{pb} . The striker and the penetrating bar velocities are calibrated in terms of the compressor air pressure directly controlled by the experimenter. The data have been represented by a non-linear curve fitting schemes that gave the following empirical equations:

$$V_{pb} = 9x10^{-5} p^{0.7072} \qquad \textbf{3.1}$$
$$V_i = 0.0014 p^{0.7007}$$

The corresponding perforation and impact energies are determined from:

$$E_{pb} = \frac{1}{2} m_{pb} V_{pb}^{\ 2} \qquad \textbf{3.2}$$
$$E_i = \frac{1}{2} m_{sb} V_i^{\ 2}$$

where m_{sb} is the mass of the 0.61m striker bar equal to 2.47 kg, m_{pb} equal to 14.6 kg is the mass of the 3.66 m penetrating incident bar, the compressor pressure, p, is in Pa (1 MPa = 145 psi), velocity are in m/s, and energy in Joules. The above relationships provide us with a reliable impact pressure-impact energy calibration.

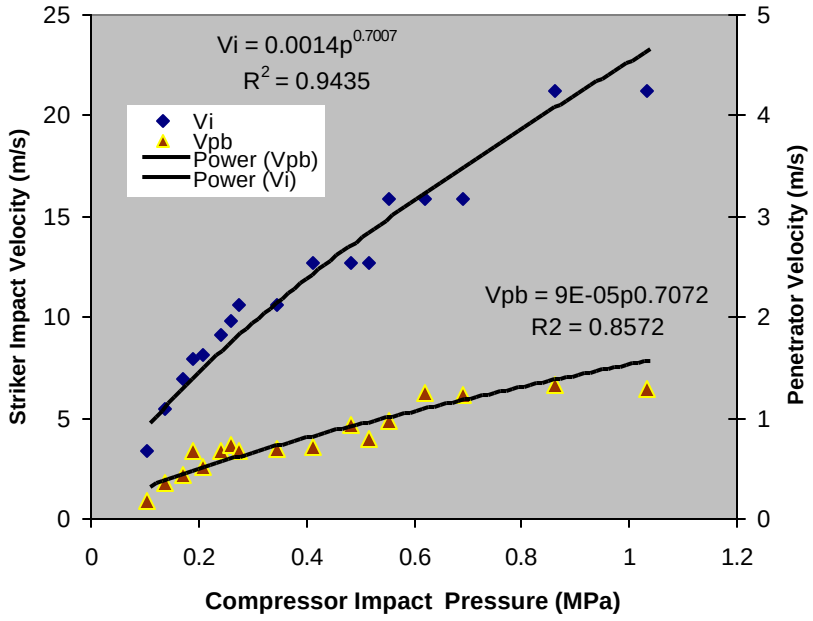

(a)

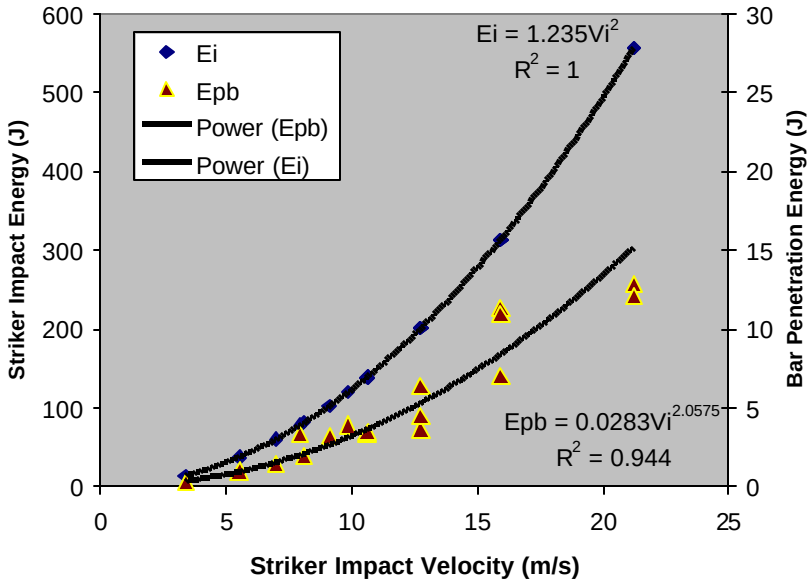

(b)

Figure 3.7: (a) Variation of striker impact and penetrator velocities with compressor Air Pressure (MPa) and (b) variation of incident bar penetration energy with striker velocity ($V_{pb}=0.0665V_i$, $R^2 = 0.92$, $E_{pb}=0.0271E_i$,$R^2=1.0$)

3.8 Criteria for Experimental Validation of Hopkinson Bar

3.4.1.1 A region of constant strain rate for about 200-300 microseconds (plateau) with changes in strain. This characterizes the specimen damage and this expected to increase as the specimen thickness increases (see strain rate – strain plot). This is very important in other for SHPB to be valid.

3.4.1.2 Tensile strain release wave usually occurs between 250-300 microseconds (see force-time graph). This is shown to be negative since it is a direct opposite of compressive wave stress. The different in this two parameter depicts the extent of damage to the specimen and these depend on the impact energy and velocity of the striker bar.

3.4.1.3 On the integration graph, the incident, reflected and the transmitted wave are moved to zero to that data can be integrated from $0 \rightarrow t$.

The experiments were performed at ambient temperature and moisture conditions. The different experimental parameters are summarized below specific for the results presented in this report.

Specimen Parameters

Samples Diameter:	1.5 in (38 mm)
Composite sample type:	(a) 12,16 and 24-layer plain weave Carbon fiber composite

System Parameters

Hopkinson Bar

Young's Modulus of maraging steel bar:	2.07×10^{11} Pa
Wave velocity in maraging steel bar:	5010 m/s
Bar length:	43.9 m

Density of maraging steel:	8000km/m^3

High Speed camera

Speed (Continuous Access):	100,000 to 1 million frames per second
Light Duration:	166 us to 700 us
Delay time:	700-850 us
Film Type:	T-Max 400 and 3200

Impact Parameters

Penetrator:	3/16-, 7/32- and 1/4-inch protruding spherically, 3/16-inch Protruding hemispherical and 1/4-inch diameter conical hemispherical maraging steel
Striker bar length:	2 feet (0.61m) maraging steel
Ram displacement:	0.61 m to impact the incident bar
Compressed air pressure:	0-250 psi
Striker Impact Energy (From Calibration):	$E_i = ap^x$
Striker Impact Velocity (from Calibration)	$V_i = bp^y$

(where p is compressor pressure in MPa; 1 MPa=145 psi, a, b, x, y are constants that depends on system set up)

4.0 EXPERIMENTAL RESULT

4.1 Determination of Ballistic Limit for Woven Composites

Figure 4.1 shows the plot of crack length and crack height (residual displacement above perforation threshold assumed to the thickness of the specimen). Ballistic limit here is defined as the threshold energy that has to be exceeded before a visible damage can be seen on the specimen (that is a small beam of light seen through the opened space). The curve exhibits very good s-curve shape typical of the ballistic region phenomenon.

The sudden rise seen on the result indicated that the specimen has been perforated thereby depicting the ballistic limit for this specimen. The crack length and height depends on the impact energy to a reasonable extent. Interestingly, after the ballistic limit has been exceeded the remaining residual energy (energy available after ballistic limit) will result into almost no further damage to the specimen.

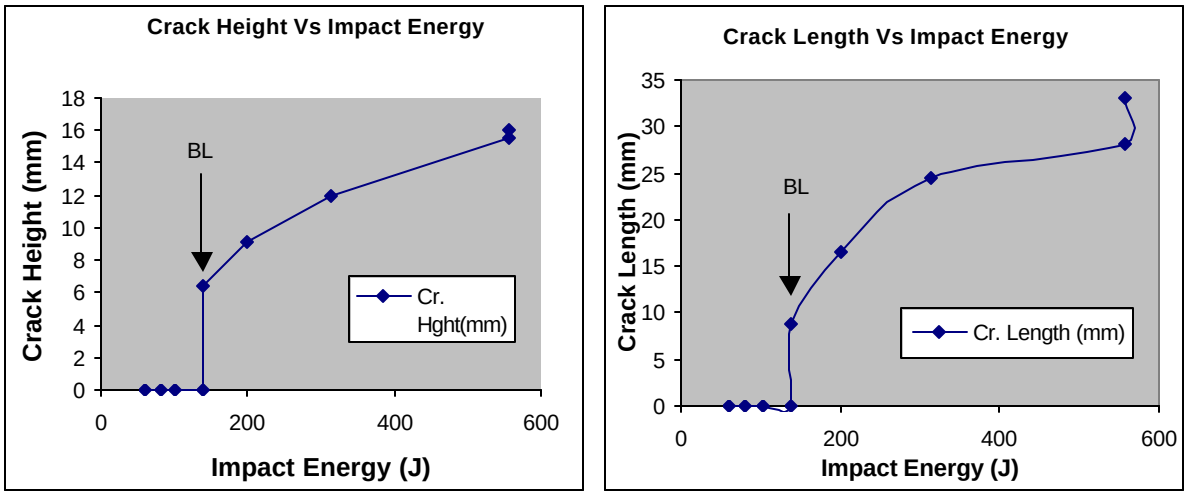

(a) (b)

Figure 4.1 Variation of (a) Crack height and (b) crack length with striker impact energy for plain woven graphite epoxy composite using 1/4-inch spherical nose penetrator

Figure 4.2 (a-d) compares the effects of sample thickness on ballistic limit velocity for the different penetrator geometries at their damage thresholds (BBL, BL and ABL).

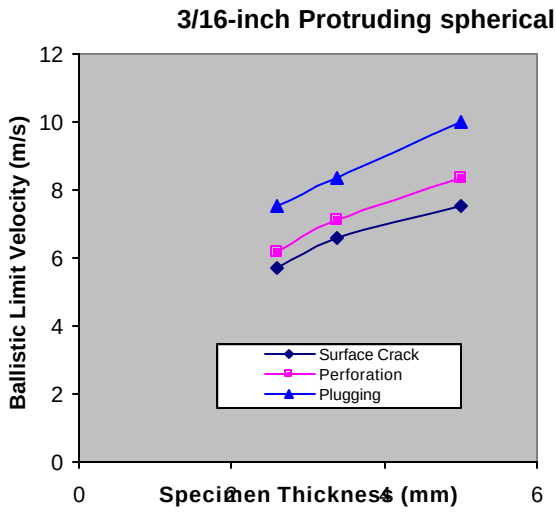

(a)

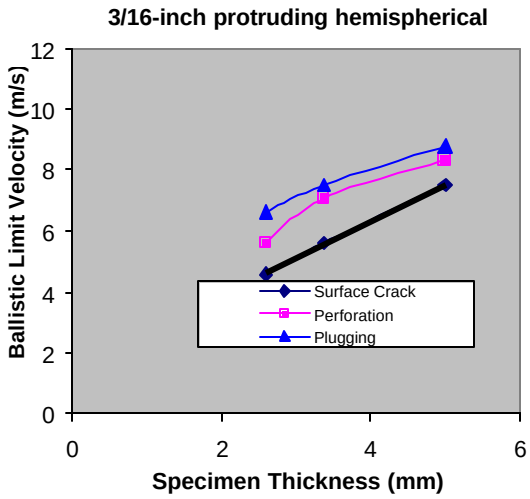

(b)

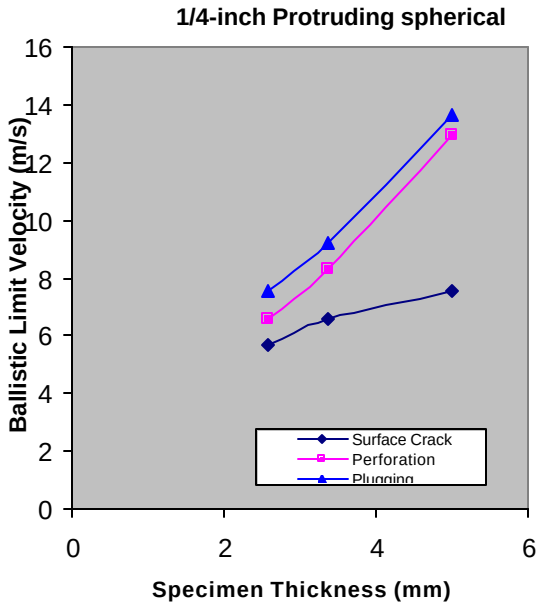

(c)

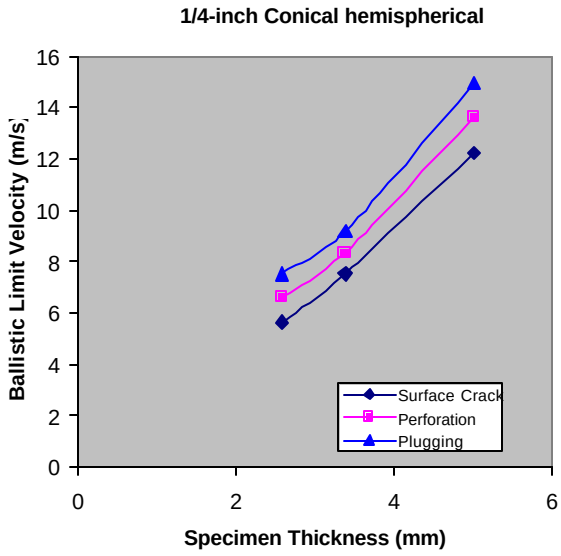

(d)

Figure 4.2 Variation of striker bar ballistic limit velocity with sample thickness for three penetrator geometries (a- c) protruding spherical and (b) protruding hemispherical and (d) conical hemi-spherical (The penetrating bar ballistic velocity is $V_{pb}^{BL} = 0.0665V_i^{BL}$) for plain weave specimen

Figure 4.2 (a-b) compares the 3/16-inch protruding spherical to the 3/16-inch Protruding hemispherical penetrator while Figure 4.2 (c-d) compares 1/4-inch Protruding spherical to 1/4-inch

Conical hemispherical penetrator. The ballistic limit can be seen to increase with sample thickness and from the above result, it can be seen that the penetrator geometry plays a significant role in specimen deformation in generating surface crack, perforation and plugging or punch-through levels of damage modes rather than penetrator sizes. Ballistic limit for spherical protruding is higher than protruding hemispherical penetrator for all the thickness. The damage of the protruding hemispherical penetrator is highly localized because of the penetrator shape.

The result also shows that the ballistic for conical hemispherical penetrator is also higher than protruding spherical for all the sample thickness studied (see Figure 4.2 c-d). In others words, for the same target thickness, protruding spherical penetrator will defeat the target at a lower energy level compared to the conical hemispherical. Once the target is defeated, it will cause a global damage to the target due to the effect of the increasing surface area. As the size of the penetrator is increased as in Figure 4.2, the penetration and perforation thresholds increase significantly causing a more global destruction of the target.

The table (4.1-4.5) below shows the energy absorbed by each specimen layer at the ballistic limit using different penetrators. The result indicated that protruding hemispherical penetrator would defeat its target at a lower energy level than any of the penetrators. However the damage is highly localized because of the penetrator shape while conical hemispherical will require higher energy to defeat its target apparently because of the conical section of the penetrator. Once the target is defeated, it will cause a global damage to the target.

Table 4.1 Damage initiation energy/layer for graphite epoxy woven specimen using 3/16 –inch Protruding Spherical

Specimen	Surface Crack Initiation		Perforation		Plugging	
	Impact Energy (J)	Striker Impact Velocity (m/s)	Threshold Energy **(J)**	Threshold Velocity (m/s)	Threshold Energy **(J)**	Threshold Velocity (m/s)
12 layer	40	5.69	47	6.17	70	7.53
16 layer	54	6.61	62	7.09	86	8.34
24 layer	70	7.53	86	8.34	123	9.98
Energy (J)/layer for 12 layer	3.3J/layer		3.9J/layer		5.8J/layer	
Energy (J)/layer for 16 layer	3.4J/layer		3.9J/layer		5.4J/layer	
Energy (J)/layer for 24 layer	2.9J/layer		3.6J/layer		5.1J/layer	

Table 4.2. Damage initiation energy/layer for graphite epoxy woven specimen using 7/32 -inch Protruding Spherical

Specimen	Surface Crack Initiation		Perforation		Plugging	
	Impact Energy (J)	Critical Striker Velocity (m/s)	Threshold Energy (J)	Threshold Velocity (m/s)	Threshold Energy (J)	Threshold Velocity (m/s)
12 layer	40	5.69	54	5.69	70	7.53
16 layer	54	6.61	78	7.95	86	8.34
24 layer	70	7.53	113	9.57	143	10.76
Energy (J)/layer for 12 layer	3.3J/layer		4.5J/layer		5.8J/layer	
Energy (J)/layer for 16 layer	3.4J/layer		4.9J/layer		5.4JJ/layer	
Energy (J)/layer for 24 layer	2.9J/layer		4.7J/layer		6.0J/layer	

Table 4.3 Damage initiation energy/layer for graphite epoxy woven specimen using 1/4 -inch Protruding Spherical

Specimen	Surface Crack Initiation		Perforation		Plugging	
	Impact Energy (J)	Critical Striker Velocity (m/s)	Threshold Energy (J)	Threshold Velocity (m/s)	Threshold Energy (J)	Threshold Velocity (m/s)
12 layer	40	5.69	54	6.61	70	7.53
16 layer	54	6.61	86	8.34	104	9.18
24 layer	70	7.53	206	12.92	229	13.62
Energy (J)/layer for 12 layer	3.3J/layer		4.5J/layer		5.8J/layer	
Energy (J)/layer for 16 layer	3.4J/layer		5.4J/layer		6.5J/layer	
Energy (J)/layer for 24 layer	2.9J/layer		8.6J/layer		9.5J/layer	

Table 4.4 Damage initiation energy/layer for graphite epoxy woven specimen using 3/16 -inch Protruding Hemispherical

Specimen	Surface Crack Initiation		Perforation		Plugging	
	Impact Energy (J)	Striker Impact Velocity (m/s)	Threshold Energy (J)	Threshold Velocity (m/s)	Threshold Energy (J)	Threshold Velocity (m/s)
12 layer	26	4.59	39	5.62	54	6.61
16 layer	39J	5.62	62	7.09	70	7.53
24 layer	70	7.53	86	8.34	95	8.78
Energy (J)/layer for 12 layer	2.1J/layer		3.3J/layer		4.5J/layer	
Energy (J)/layer for 16 layer	2.4J/layer		3.9J/layer		5.8J/layer	
Energy (J)/layer for 24 layer	2.9J/layer		3.6J/layer		4.0J/layer	

Table 4.5 Damage initiation energy/layer for graphite epoxy woven specimen using 1/4 -inch Conical Hemispherical

Specimen	Surface Crack Initiation		Perforation		Plugging	
	Impact Energy (J)	Striker Impact Velocity (m/s)	Threshold Energy (J)	Threshold Velocity (m/s)	Threshold Energy (J)	Threshold Velocity (m/s)
12 layer	39	5.62	54	6.61	70	7.53
16 layer	70	7.53	86	8.34	104	9.18
24 layer	184	12.21	229	13.62	275	14.92
Energy (J)/layer for 12 layer	3.3J/layer		4.5J/layer		5.8J/layer	
Energy (J)/layer for 16 layer	4.4J/layer		5.4J/layer		6.5J/layer	
Energy (J)/layer for 24 layer	7.6J/layer		9.5J/layer		11.5J/layer	

4.2 Characterization of the Waveforms

Figure 4.3-4.7 shows a typical incident, reflected and transmitted stress pulses determined from the measured strain signal using appropriate measuring system calibration for a 16 layer plain weave woven composite specimen using the protruding spherical penetrator. The incident wave reaches the strain gage located at 1.829 mm in 395 microseconds and 790 microseconds to the bar/specimen interface at 3.658 m. This represents a wave speed of 4630 m/s compared to the

5010 m/s theoretical value (determined from the density and elastic modulus supplied for the maraging steel hopkinson bar material). On reaching the bar/specimen interface part of this wave

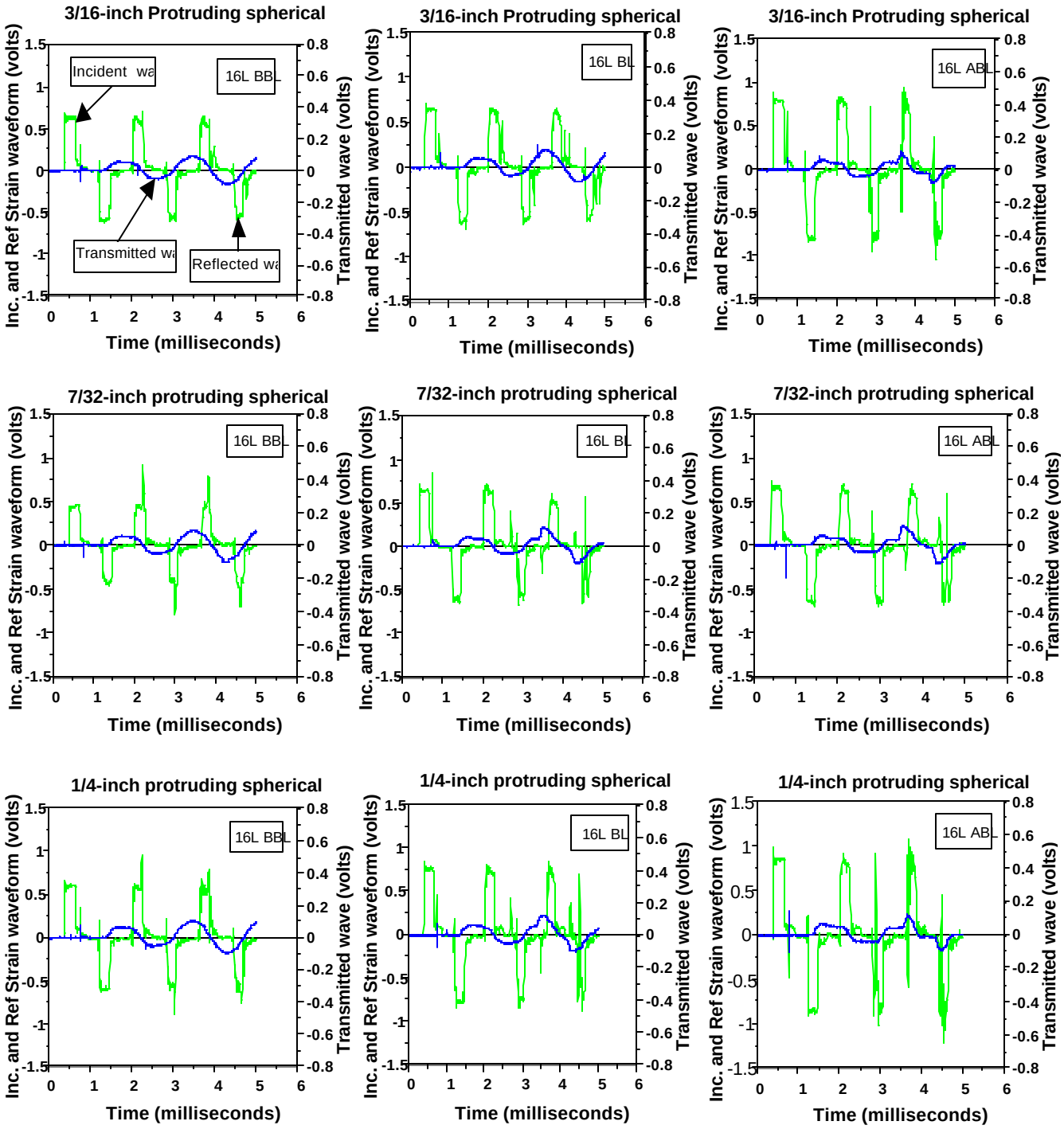

Figure 4.3 Effect of penetrator size on specimen waveform using different sized protruding spherical penetrators.

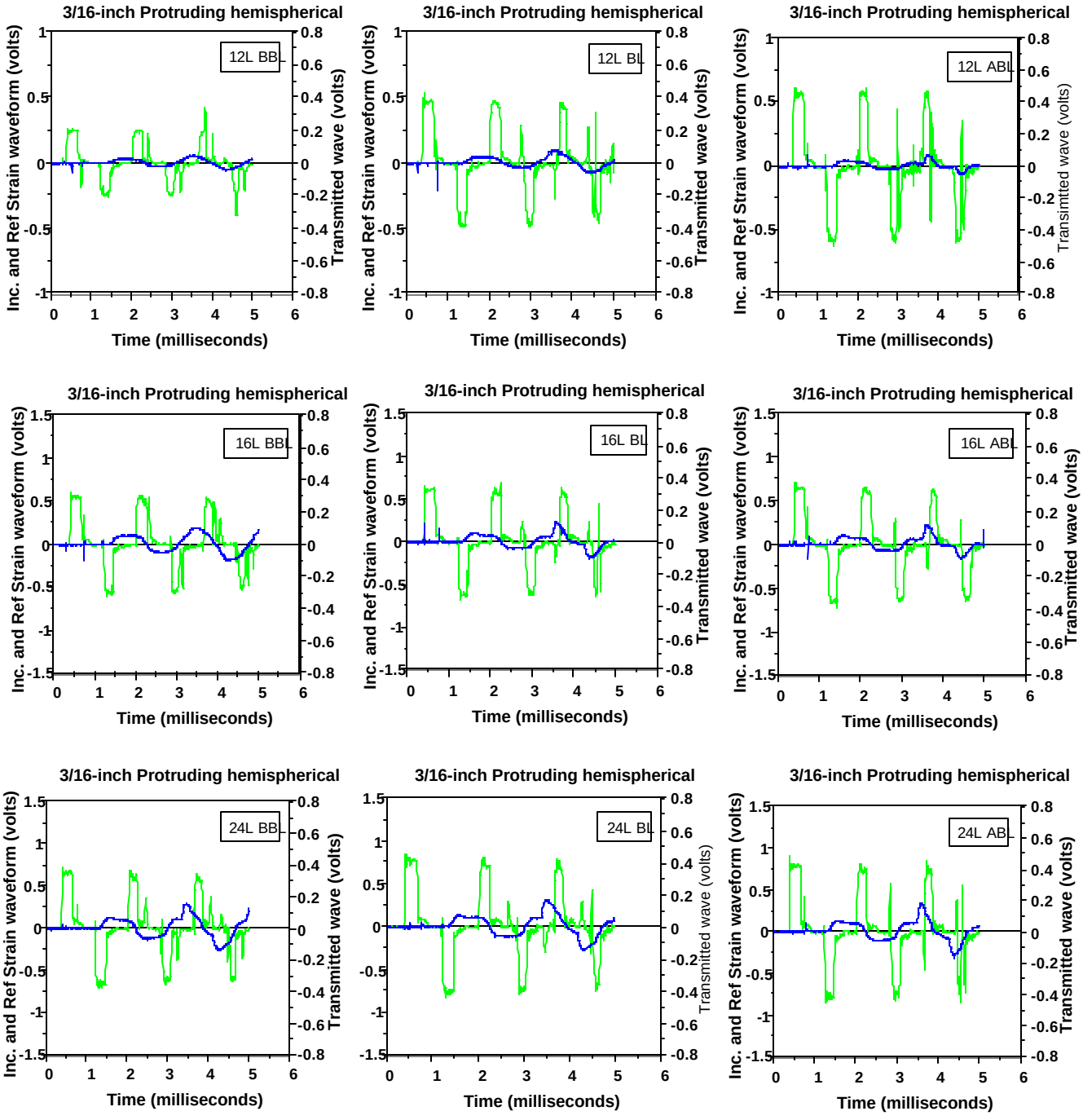

Figure 4.4 Effect of sample thickness and energy absorbed on specimen waveform using 3/16 –inch protruding hemispherical penetrator.

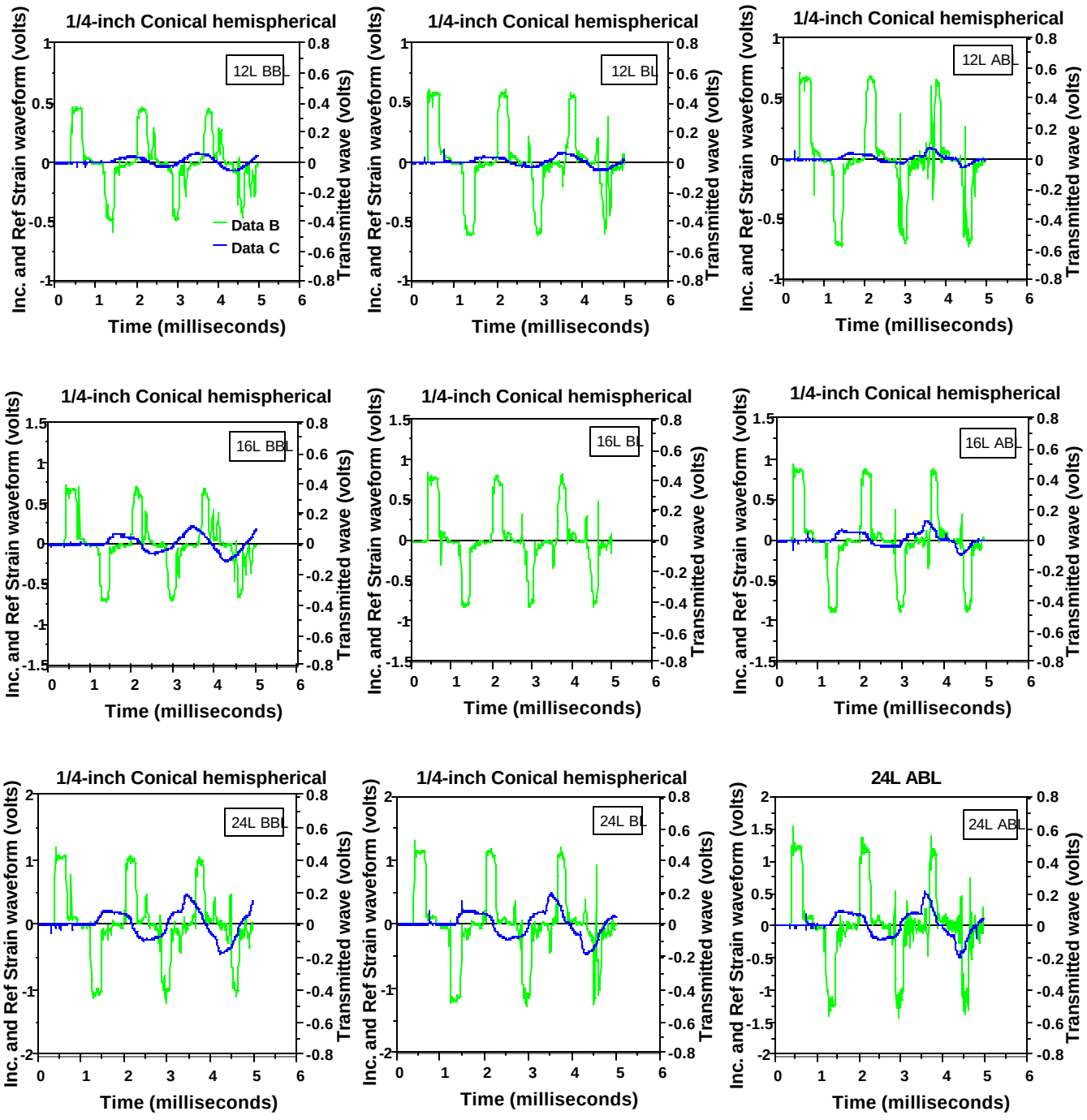

Figure 4.5 Effect of sample thickness and energy absorbed on the specimen waveform using 1/4-inch conical hemispherical penetrator

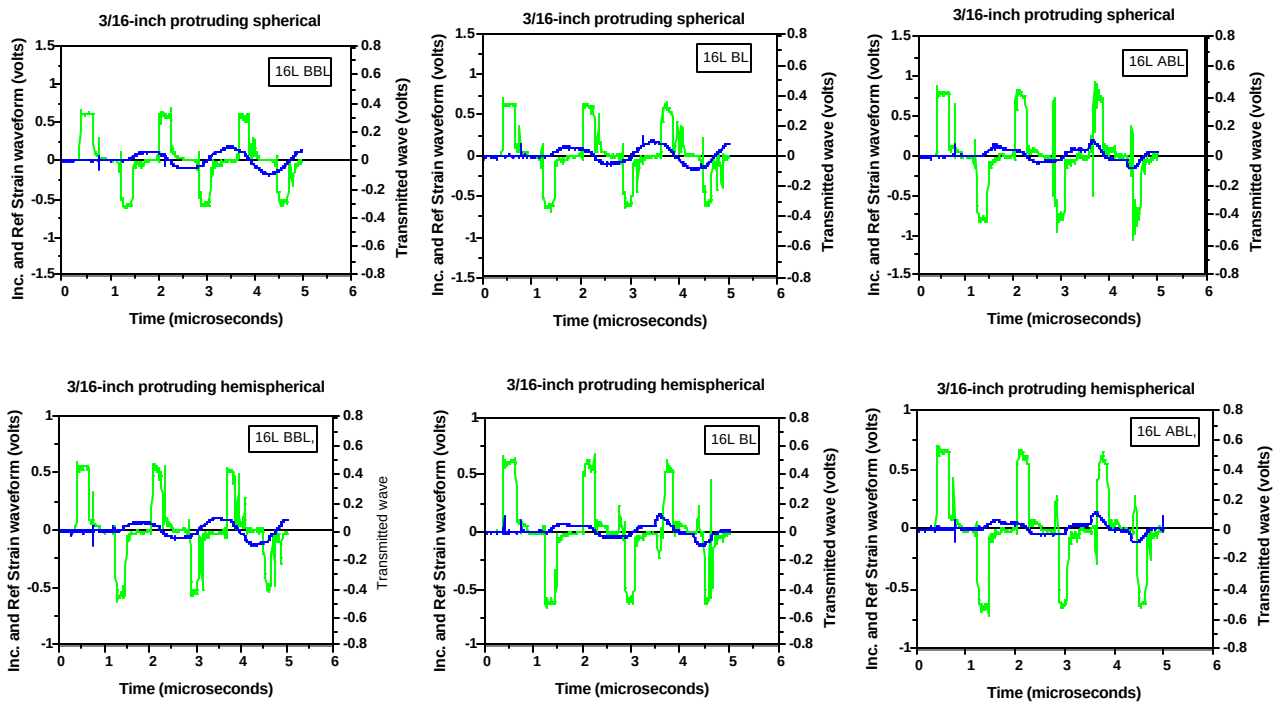

Figure 4.6 Effect of penetrator geometry on specimen waveform using 3/16-inch protruding spherical and 3/16-inch protruding hemispherical

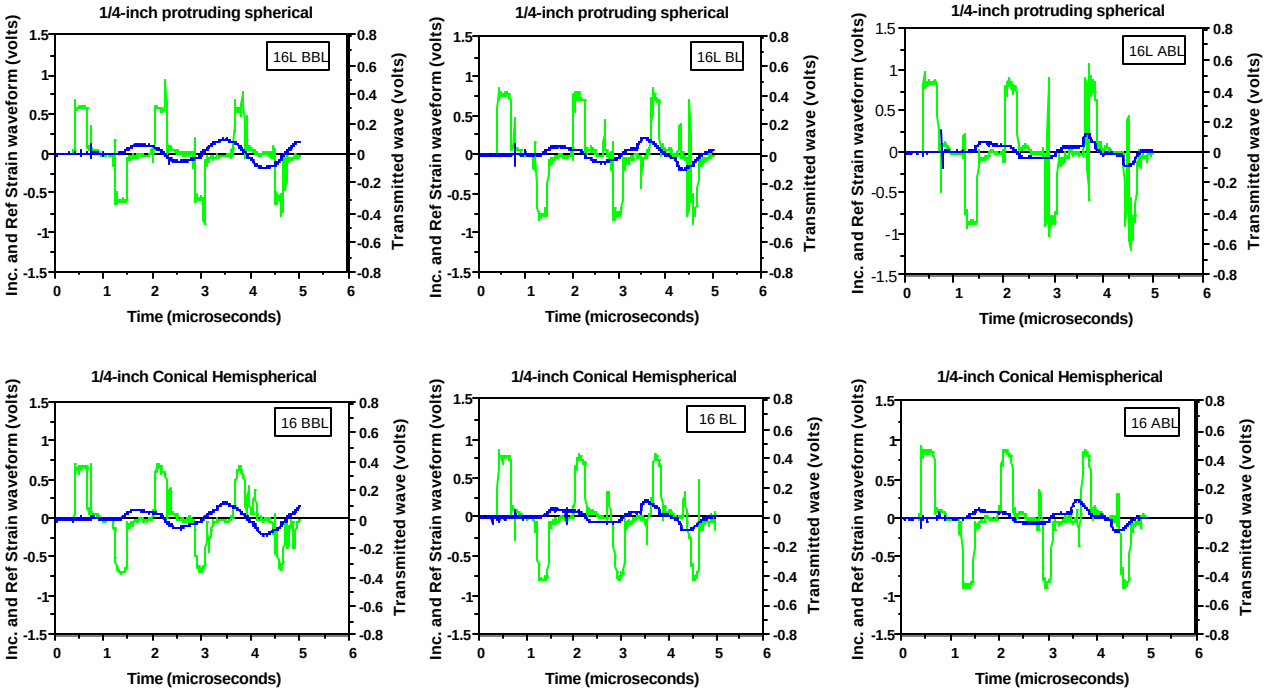

Figure 4.7 Effect of penetrator geometry on specimen waveform using 1/4-inch protruding spherical and 1/4-inch conical hemispherical

will be reflected back into the bar, traveling at the same speed it will reach the strain gage at about 395 microseconds. Without a specimen, the transmitted wave will also begin its traverse time at the same time as the reflected wave and will reach the strain gage on the transmitter bar after 395 μs. The strain wave pulse provides information for complete characterization of the damage process; this wave when integrated provides the energy absorbed –time history, force – displacement, stress – strain and other relevant data with which the specimen damage can be characterized.

The waveform was captured at the damage thresholds (below, at and above ballistic limit) using different protruding spherical penetrator (i.e. 3/16, 7/32 and 1/4-inch) for the experiment. It can be seen from the result that the amplitude of the all the waves increases as the damage threshold increases. The figure consistently shows that below the ballistic limit for all the penetrators, the waves were smooth and already established. At the ballistic limit, little distortion can be seen after the second wave and it tends to increase as the penetrator size increases. This behavior could be attributed to the transition between the spherical ends into the protruding section of the penetrator.

Figure 4.4 shows the waveform using the 3/16-inch protruding hemispherical penetrator; the amplitude of the wave also increases with the damage thresholds. From the figure, it can be seen that the there is a little distortion after the second wave; Nwosu [5] explained this to be as a result of global effect of the penetrator inside the specimen. For the 12-layer specimen, the waves become more established as the damage threshold increases, while 16 and 24 layer waves have been fully formed for all the damage thresholds. The behavior is similar to the waveform for 1/4-inch conical hemispherical penetrator as shown in Figure 4.5, the only difference noticed was that for the thicker specimen (24 layer), there was a lot of distortion in all the damage

threshold studied; this might not be unconnected with the conical portion of the penetrator taking part in the deformation process.

Figure 4.6 compares the effect of penetrator geometry using the 3/16-inch protruding spherical and 3/16-protruding hemispherical penetrator for a 16-layer specimen. The figure shows that the waves were fully formed for both penetrators at all the damage threshold studied. However, protruding penetrator showed little or no distortion below the threshold energy while protruding hemispherical showed a significant wave distortion after the second wave. At the threshold energy, protruding spherical penetrator wave became distorted after the second wave, but a cleaner wave was noticed in the protruding hemispherical penetrator signifying that the specimen has been perforated. This behavior continues after the threshold energy has been exceeded with little or no distortion on the waves.

Figure 4.7 characterizes the effect of penetrator geometry on specimen waveform using 1/4-inch protruding spherical and 1/4-inch conical hemispherical. The result showed that the waves were all formed for all the damage thresholds. Protruding spherical penetrator showed little distortion below ballistic limit, but conical hemispherical penetrator wave seems to be distorted after the second wave. At and above the ballistic limit protruding spherical wave generated suffer a considerable distortion while a cleaner wave can be seen on the conical hemispherical penetrator.

In conclusion, penetrator geometry affects to a reasonable extent the damage response of a specimen when impacted. As can be seen from the waveforms, determination can reasonably be made to determine if a specimen has been perforated or not. Protruding spherical penetrator behavior seems a little bit different from the other penetrators because of its shape.

4.3 Effect of penetrator size on dynamic failure response of graphite epoxy (woven) composite around the critical perforation energy

It was hypothesized in this study that the energy absorbed by a material will vary with the size and geometric shape of the penetrator used. For this study we used three different shaped penetrator and sizes, namely: protruding spherical, conical hemispherical and protruding hemispherical penetrators (see Figure 3.2). The protruding spherical penetrator formed the basis for the experiment while the others will provide a comparison for the result obtained form the spherical penetrator. These we hope will give us an insight into which penetrator delivers a more devastating damage on the plain weave woven graphite epoxy composite material used for this study and the overall dynamics of the failure. At same energy level, we hypothesized that all the penetrator will deliver nearly the same amount of penetration energy to the specimen but that the level of damage for different penetrators will be different owing to different energy dissipation rate of each penetrator. For example we expect the damage on smaller sized penetrator, especially protruding hemispherical, to be localized. Also, the ballistic limit for all the penetrators should increase as the diameter of the contact end of the penetrator increases.

The damage parameters that would be studied in this report are:

1. Energy Absorbed
2. Strain rate – strain
3. Stress – Strain relationship
4. Force-displacement

4.3.1 Effect of penetrator size on damage parameter around the Critical Energy using spherical Protruding Penetrator for varying sample thickness

In this section, we present the damage of different specimen thickness and penetrator geometry at the critical energy (also referred to as ballistic limit region). Experimental investigation carried out by previous authors [5, 14,37] revealed that specimen thickness has greater influence on impact perforation resistance. As specimen thickness increases the perforation resistance also increases and the higher the striker impact energy required for the perforation. Hence, the effect of specimen thickness for composite material must be thoroughly investigated at the region of ballistic limit (i.e. below and above the ballistic limit). This parameter would provide the basis to classify the resistance of the material to damage initiation and propagation.

4.3.1.1 Energy Absorbed – Time profile. Figure 4.8 (a-i) shows the plot of energy absorbed – time for 12-layer specimen at the damage thresholds (below, at and above the critical energy), the specimen steadily absorbed the energy released by the penetrators (3/16, 7/32 and 1/4-inch). At a low energy most of the energy is expended to overcome the specimen's internal stress before a noticeable damage could be done to the specimen, because the rate of energy absorbed by the specimen is lower than the impact energy damage threshold. Hence the material can be said to exercise a high compressive strength at this stage. This stage is characterized by incipient damage with small matrix cracking [5, 14].

At the critical or the ballistic limit, the specimen seems to absorb more energy even at the unloading section for all the protruding spherical penetrators studied regardless of specimen thickness and penetrators sizes. The uniform energy absorption after the first peak occurring the first 80 microseconds of the experiment is more noticeable on the 3/16-inch spherical penetrator,

apparently because of a smaller contact area. As the spherical end of the penetrator head transverse the specimen, the crack created tends to close back before transitioning into the protruding section, this lead to further energy absorption before the strain is released at the back of the specimen. The shape of this uniform loading section seems to reduce as the penetrator

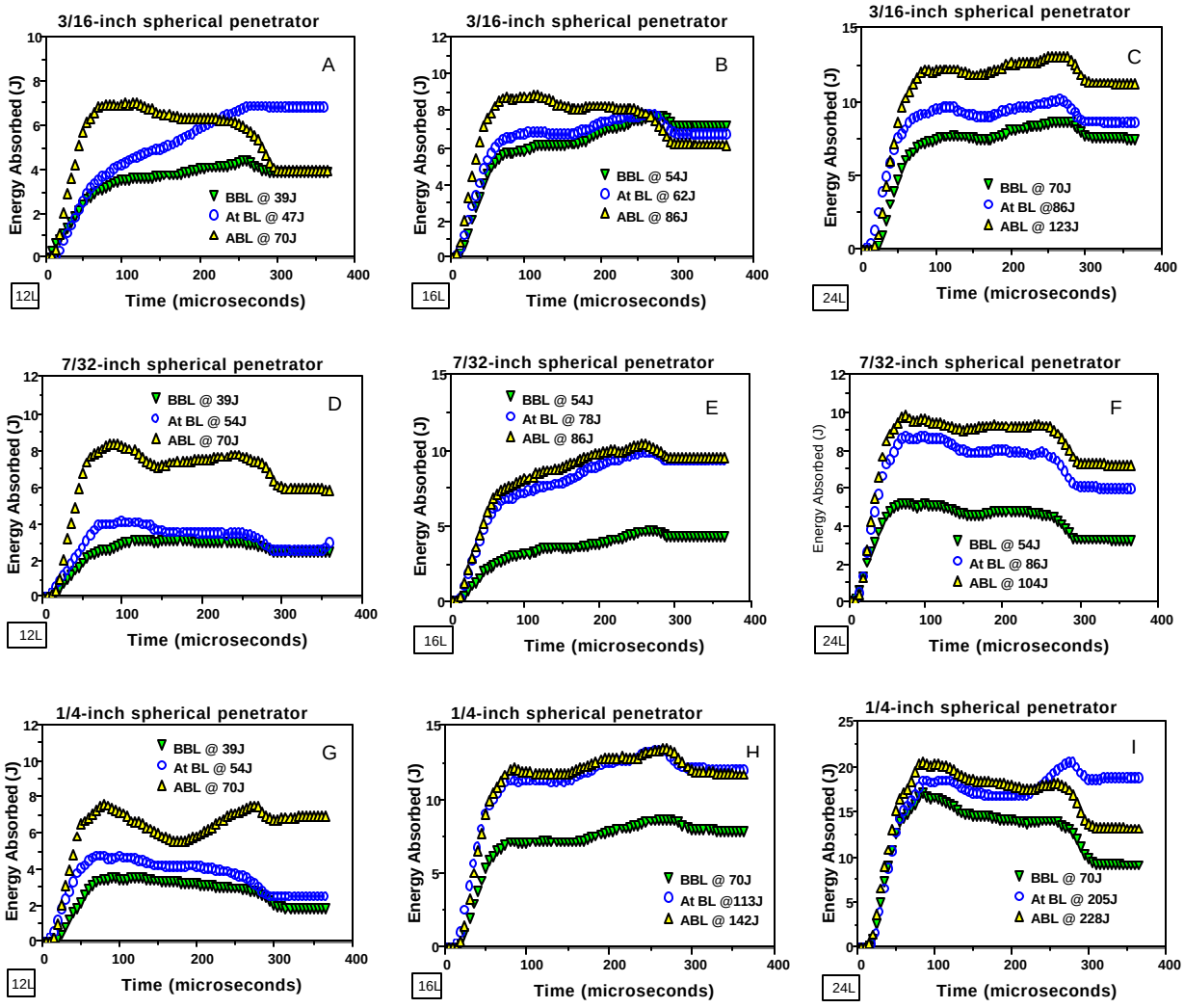

Figure 4.8 (a-c) Energy Absorbed – time plot for varying sample thickness (12, 16 and24) 24- layer specimen different sized penetrators (a-c) 3/16, (d-f) 7/32 and (g-I) 1/4-inch protruding spherical penetrator.

size and sample thickness increases. The typical damage here is penetration, fiber stretching (depicted by bulging at the back of specimen), matrix cracking, fiber breakage and impending perforation.

Beyond the ballistic limit, the specimen would have suffered some measure of irrecoverable damage at this point, this evident by high amplitude tensile strain release energy occurring at the rear end of the specimen. The constant energy absorbed region after the tensile release strain is said to be the energy absorbed or retained in the specimen.

Figure 4.8 (d-f) shows the specimen energy absorption for the 16-layer specimen. The specimen response can be seen to characteristically the same for the damage thresholds (below, at and above ballistic limit). After the first peak the specimen appears to go through a small plateau or constant energy absorption region (which increases as the specimen thickness and penetrator size increases) and thereafter the specimen continues absorb more energy before tensile strain release. At the damage thresholds studied (BBL, BL and ABL), it was discovered that, the rate at which the specimen retains the energy released to it by different sized penetrator is inversely proportional to the striker impact energy. This behavior is in agreement with our hypothesis, that beyond the ballistic limit any further impact energy will not result into any appreciable damage to the specimen but will be lost to the system as a residual energy.

However, the tensile release strain energy released at the rear of the specimen will be higher beyond the ballistic limit since the specimen would have suffered a perforation with greater residual energy. Above the ballistic limit there is gradual unloading of the compressive stress after the peak energy level has been reached.

Figure 4.8 (g-i) shows the energy absorption for the 24-layer specimen. The energy absorption profile for this specimen is characteristically the same for all the penetrators. The

ringing noticed on the specimen at and above the ballistic limit using 1/4-inch spherical penetrator is attributed to the system vibration and or the deflection of the specimen under loading. The jump in the energy absorption is attributed to higher energy required to cause a complete penetration/slight perforation in the specimen. This is due to the bigger contact surface area of the penetrator to the specimen. Above the ballistic limit the peak energy was almost the same with ballistic limit but the tensile strain is higher. Again, this result supports our hypothesis that the specimen below and at ballistic limit, the specimen absorbs the most energy delivered to it.

Figure 4.9a shows the effect of sample thickness on energy released to the specimen at the damage threshold using 3/16-inch spherical penetrator. The result shows that energy released by the penetrator increases as the damage threshold increases. The ratio of energy released by the penetrator to the damage threshold is almost linear for all the specimen thickness studied. Below and at the critical energy using the 3/16-inch penetrators the 12 and 16 layer specimen seems to agree with our hypothesis that beyond critical energy any residual energy left in the system does not significantly cause any more damage to the specimen. One reason that could be adduced for more energy absorbed by the 24-layer specimen after the critical energy could be that, the impact energy at that point is still within ballistic limit range (as can be seen from the stress-strain result discussed later in this chapter).

Figure 4.9b presents the effect of sample thickness on energy released by 7/32-inch penetrator to the specimen. The results indicate that the thicker specimen (i.e. 16 and 24 layers) absorbed very little energy beyond the ballistic limit. This is indicated by almost plateau region (constant) beyond the ballistic limit from the result. The 12-layer specimen however behaves

differently. This might not be unconnected with striker impact energy still being within the ballistic limit threshold.

Figure 4.9c shows the effect of sample thickness on energy released by 1/4-inch spherical penetrator. The result is consistent with the 7/32-inch penetrator result, with 16 and 24 layer specimen absorbing little or no energy after the ballistic limit. This behavior supported our hypothesis of specimen not absorbing any appreciable energy after the ballistic limit has been exceeded.

In conclusion, damage threshold increases as the specimen thickness increases as a result of greater striker impact energy. This evident from the result 12-layer specimen which has the least energy absorbed followed by the 16 layer while 24 layer absorbed the highest energy for the entire damage threshold considered in this report for all the penetrator sizes. It is also clear from the figures that for the same damage threshold, energy absorption during a perforation failure process increases with specimen thickness. The change in slope is evident at ballistic limit showing a transition to different damage level. This observed in 67% of the cases studied.

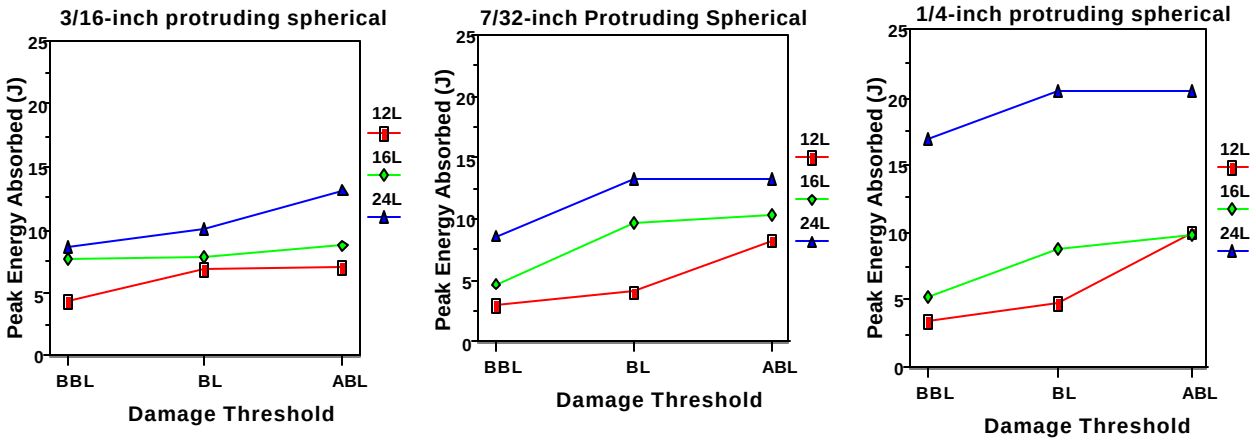

(a) (b) (c)

Figure 4.9, Showing the effect of sample thickness on peak energy absorption by the specimen at the damage threshold (below, at and above ballistic limit) for (a) 3/16, (b) 7/32 and (c) 1/4-inch protruding spherical penetrator.

4.3.1.2 <u>Effect of penetrator size on Energy absorbed for varying sample thickness.</u> Figure 4.10 (a-c) shows the effect of penetrator size on the energy absorbed by specimens for varying sample thickness. The experiment is repeated at the same energy level for varying sample thickness and penetrator sizes. This was done to be able to characterize the effect of penetrator size. The result shows that 3/16-inch penetrator consistently delivered the highest energy to the specimen while at the same time retaining most of the energy. Interestingly, 7/32-inch penetrator does not deliver as much energy to the specimen, though with the exemption of the thickest specimen (24 layer), it consistently followed the 3/16-inch in retaining the most energy in the specimen followed by the 24-layer specimen.

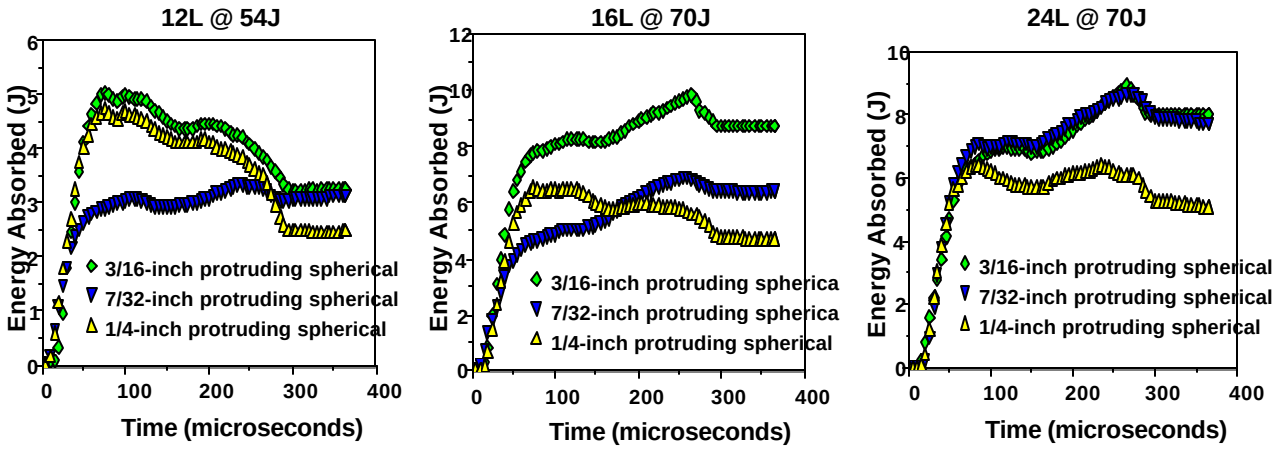

Figure 4.10 Effect of penetrator size on energy absorbed by the specimens for varying thickness: (a) 12-, (b) 16-, and (c) 24-layer.

4.3.1.3 <u>Strain rate – strain Behavior.</u> The strain rate – strain profiles shown in Figure 4.11 (a-c) provide information on the extent of damage a material suffers after the application of impulse load (either static or dynamic). The result shows that 12 layer specimen suffered more damage than the other thickness for all the penetrators sizes (3/16, 7/32 and 1/4-inch) apparently because of its size;

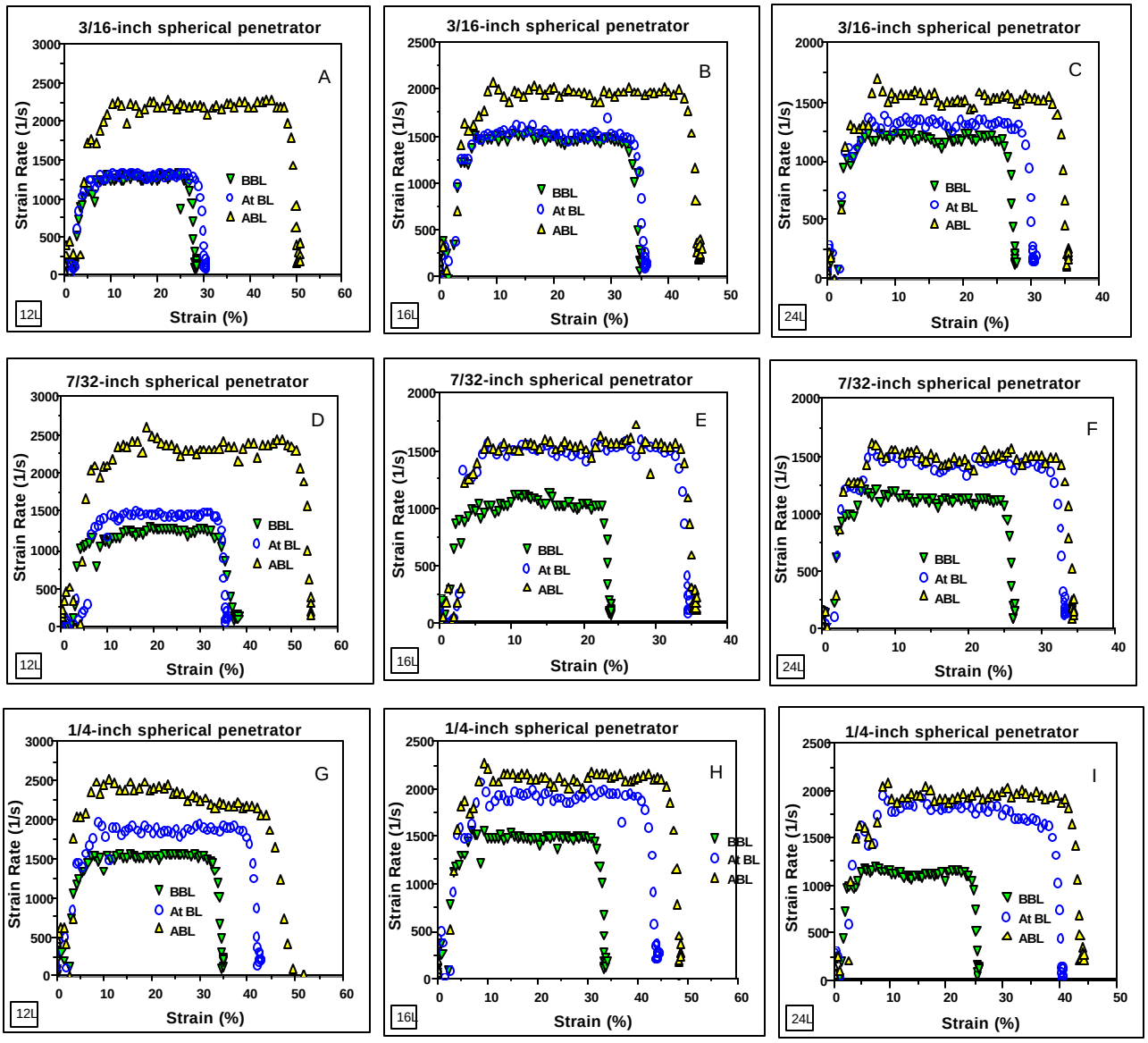

Figure 4.11 (a-c) Strain rate – strain plot for varying sample thickness (12, 16 and24) 24-layer specimen different sized penetrators (a-c) 3/16, (d-f) 7/32 and (g-I) 1/4-inch protruding spherical penetrator.

thinner specimen strain more than the thicker ones. The result shows that the energy chosen for the 3/16-inch and 7/32-inch penetrators are close for some of damage thresholds for the specimens.

Figure 4.11 (g-i) presents the specimen strain rate – strain response using ¼-inch spherical penetrator. The plot shows that increase in strain rate-strain relationship is almost a

linear in between the damage thresholds for all the specimen thickness apparently because of its larger contact surface area, which helps in distributing the strain uniformly across the specimen.

Figure 4.12 (a-c) shows the effect of penetrator size on strain rate – strain response. The experiment was repeated at the same energy close to ballistic limit energy for each specimen thickness. The result also shows that strain rate increases as the penetrator size is increased owing to the change in contact area of the penetrator. The bigger the penetrator tips the higher the impact energy needed to cause damage.

Figure 4.13 (a-c) shows the strain rate – strain result summary for all the penetrators (3/16, 7/32 and 1/4-inch). It can be seen clearly that strain rate linearly depends on strain and the ratio of strain rate to strain is a constant independent of sample thickness.

Conclusively, strain rate depends on the specimen thickness, size of the penetrator, striker velocity and the impact energy.

For all the penetrators studied, the specimen reaches their maximum strain rate and particle velocity at about 50-90 microseconds (this corresponds to peak energy absorbed time for each case). It remained constant for about 200 microseconds at which time the damage to the specimen must have been completed before finally dropping of at 325 microseconds regardless of the specimen thickness and the penetrators used for the experiment. This behavior validates one of the fundamental assumptions of Hopkinson bar that, the specimen damage is assumed to be under uniform stress during the experiment.

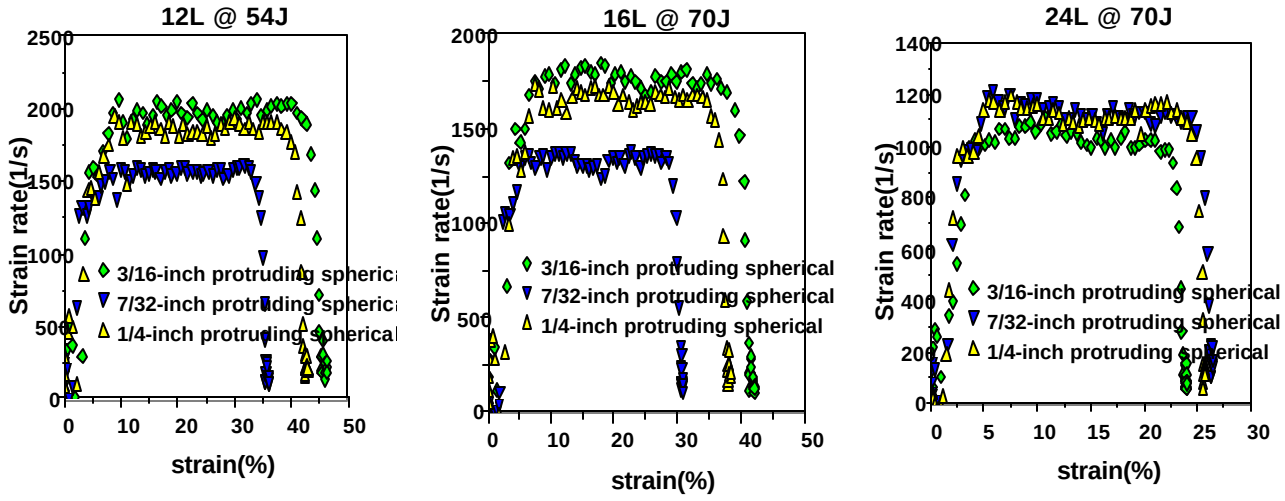

(a) (b) (c)

Figure 4.12 Effect of penetrator size on specimen response for varying sample thickness: (a) 12, (b) 16 and (c) 24 layer using different sized penetrator ends (3/16, 7/32 and ¼-inch).

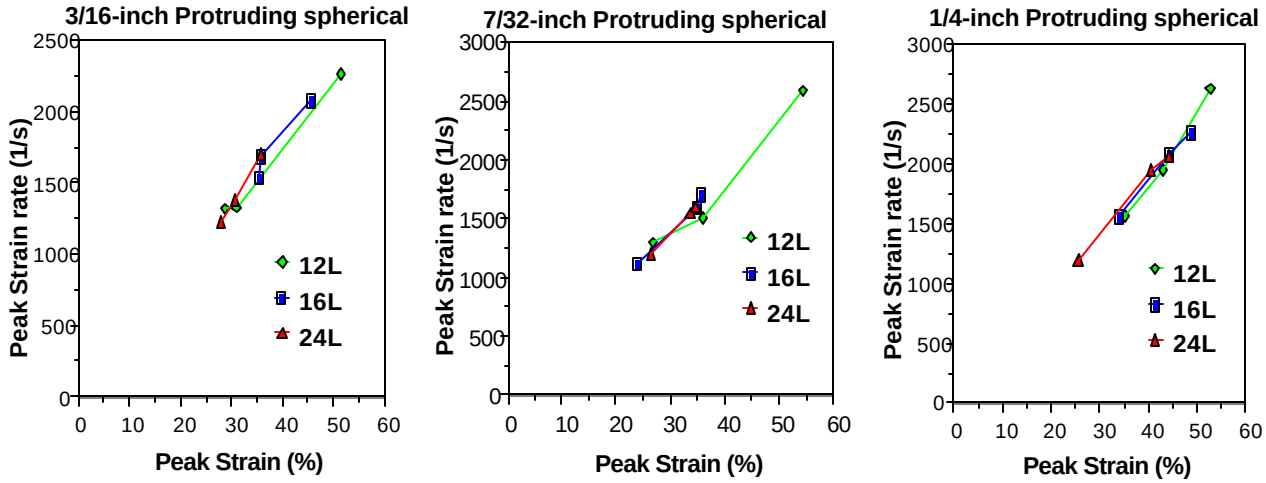

(a) (b) (c)

Figure 4.13 Strain rate – strain behavior for different specimen thickness for (a) 12-, (b) 16- and (c) 24-layers penetrated with energy around ballistic limit energy using different sized spherical protruding penetrators (3/16, 7/32 and 1/4-inch)

Figure 4.14 (a-c) presents the effect of specimen thickness on the strain rate for the spherical penetrators (3/16, 7/32 and 1/4-inch). Figure 4.15 (d-f) shows that strain rate increases

with incident energy and decreases with increase in specimen thickness. This behavior is conceivable since the thicker the specimen the more energy it can absorbed before failure (Figure 4.15 d-f). The result shows clearly the strain rate dependency on thickness. The result also indicated that the strain rate increases as the striker impact energy increases.

Figure 4.14 (g-i) show that strain rate is linearly dependent on energy. However, the slope of linearity decreases as the specimen thickness increased.

Figure 4.15 (a-c) present the ratio of strain rate to strain at the damage thresholds (below, at and above ballistic limit) for varying sample thickness and penetrator sizes (3/16-, 7/32-, and 1/4-inch). The result shows that the increase in damage threshold has no significant effect on the ratio of strain rate to strain for all the sample thickness and penetrator size. Also the average ratio of strain rate to strain is almost a constant for the entire specimen irrespective of penetrator size.

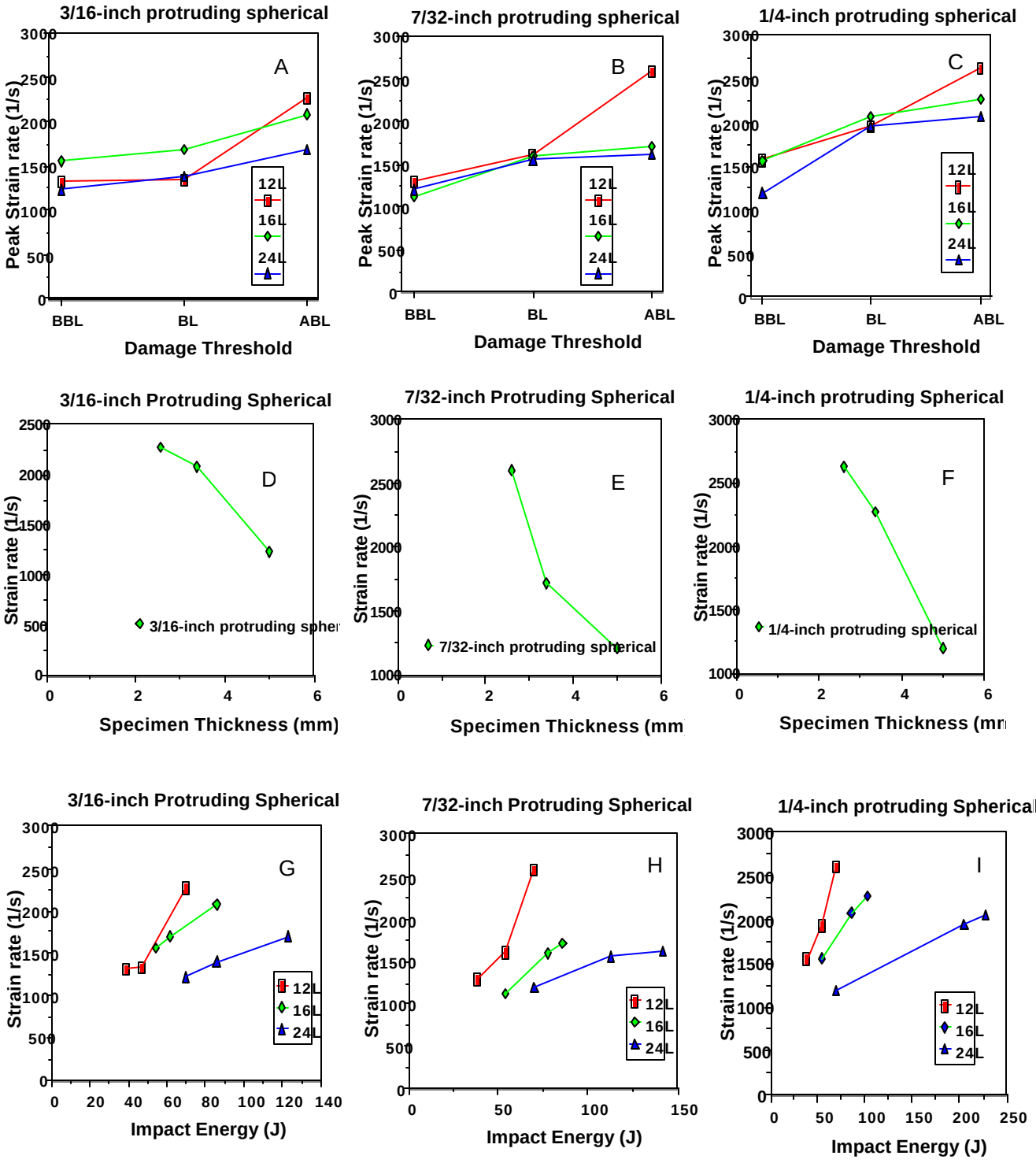

Figure 4.14 (a-c) Variation of specimen response at the damage threshold for varying penetrator sizes, (d-f) effect of sample thickness on strain rate at the damage thresholds, (g-i) Effect of Impact energy on strain rate.

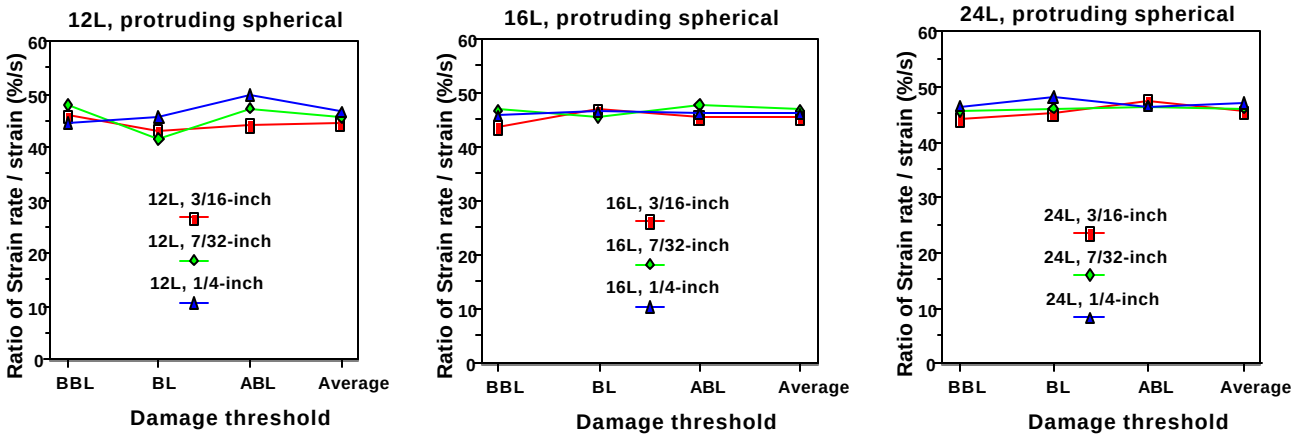

Figure 4.15 Ratio of strain rate to strain at the damage threshold for varying sample thickness using different sized penetrators.

4.3.1.4 Stress–Strain profile for varying thickness around the ballistic limit vicinity.

Figure 4.16 (a-c) shows the stress-strain history of the specimen using a 3/16-inch spherical penetrator. The results show that the area defined as below, at and above ballistic limit were all more or less within the vicinity of the threshold or critical energy to perforate specimens for all the penetrator sizes, but, it still serve the purpose for this research. The 12 layer deformation below and at ballistic using a 3/16-inch spherical penetrator seems to be dominated largely by elastic response apparently because of low striker impact energy, however plastic deformation was noticed above the ballistic limit. 16 layer specimen show both elastic and plastic response but with more plasticity than 12 layer. The 24-layer specimen also shows both elastic and plastic response with plastic behavior dominating most of the damage process for all the regions and energy threshold levels.

Figure 4.16 (d-f) shows the history stress-strain for the 7/32-inch penetrator. There appears to be a small area of elastic region before a change in slope depicting an onset of plastic deformation in the specimen regardless of the penetrators' size for all the damage threshold

considered (i.e. below, at and beyond the critical energy) for all the specimens. From the figure greater change in slope can be seen occurring more at and beyond the critical energy level for all the specimen thickness.

Figure 4.16 (g-i) shows the stress –strain behavior for the 1/4-inch spherical penetrator. The result is also consistent with other result obtained earlier on. For the thinner specimen (12 layer) the stress appears to be linear to the strain for a longer period of time before the onset of plastic deformation after the ballistic limit has been exceeded apparently because of low striker impact energy. The 16-layer specimen can be seen to behave in the same manner. However, the 24 layer behaves differently from the other specimens, though, the damage is still dominated by both elastic and plastic deformations. It shows that the sample stress is thickness dependent.

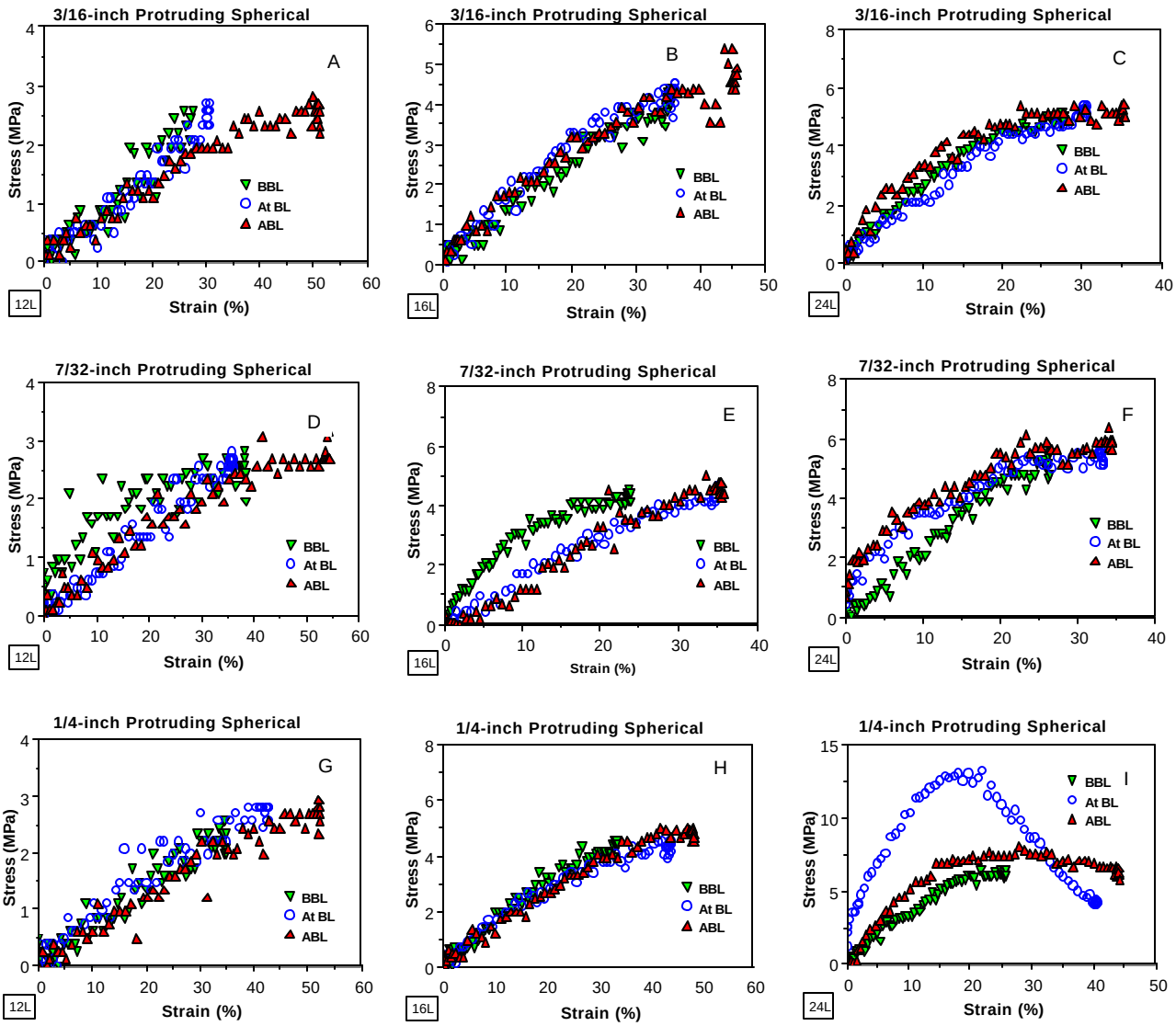

Figure 4.16 Stress-strain response for varying specimen thickness (12, 16 and 24 layer) and penetrator sizes (a-c) 3/16, (d-f) 7/32 and (g-i) 1/4-inch)

4.3.1.5 <u>Force – Displacement</u>. Figure 4.17 (a-c) indicated the force-displacement plot using the 3/16-inch penetrator. The result shows a good correlation between the impact energy, specimen thickness and penetrator size. It can be seen from the plot that, the extent of material deformation depends strongly on the impact energy and penetrator size. Maximum specimen displacement depends also on the impact energy [1,2,5,18 37]. The area just before the inception of unloading signifies the end of elastic limit beyond this point the material deforms plastically. The stress

wave is released as tensile strain release at about 300 microseconds at the back of the specimen; the constant loading afterwards signifies the energy absorbed by the specimen.

Figure 4.17 (d-f) shows the force-displacement plot using a 7/32-inch spherical penetrator. The result is consistent with what we expected and it follows the same trend as the 3/16-inch penetrators in that it elucidates displacement as being incident energy dependent for specimen thickness used.

Figure 4.17 (g-i) shows the force-displacement plot using 1/4-inch spherical penetrator. The result shows a good correlation between the impact energy, specimen thickness and penetrator size. It can be shown from the result that, the extent of material deformation depends strongly on the impact energy and penetrator size.

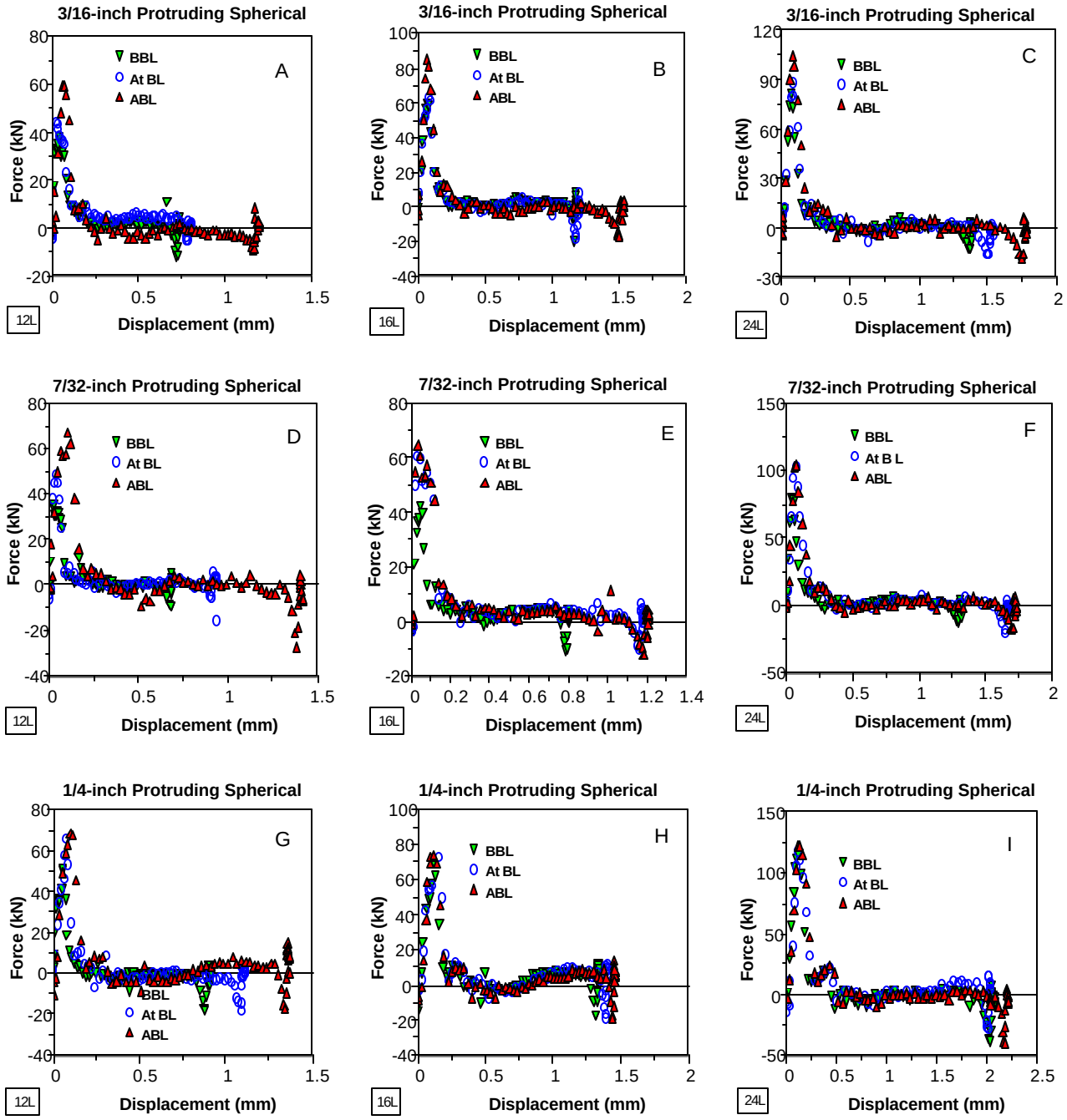

Figure 4.17 (a-c) Force- displacement plot for varying sample thickness (12, 16 and24) 24-layer specimen different sized penetrators (a-c) 3/16, (d-f) 7/32 and (g-I) 1/4-inch protruding spherical penetrator.

Figure 4.18 (a-c) shows the variation of peak force on the sample thickness for all the penetrator sizes at their damage thresholds (below, at and above ballistic limit). The result shows that peak force is proportional to specimen thickness. For the same thickness the specimen experienced greater loading at higher striker energy. This behavior is typical for all the penetrators.

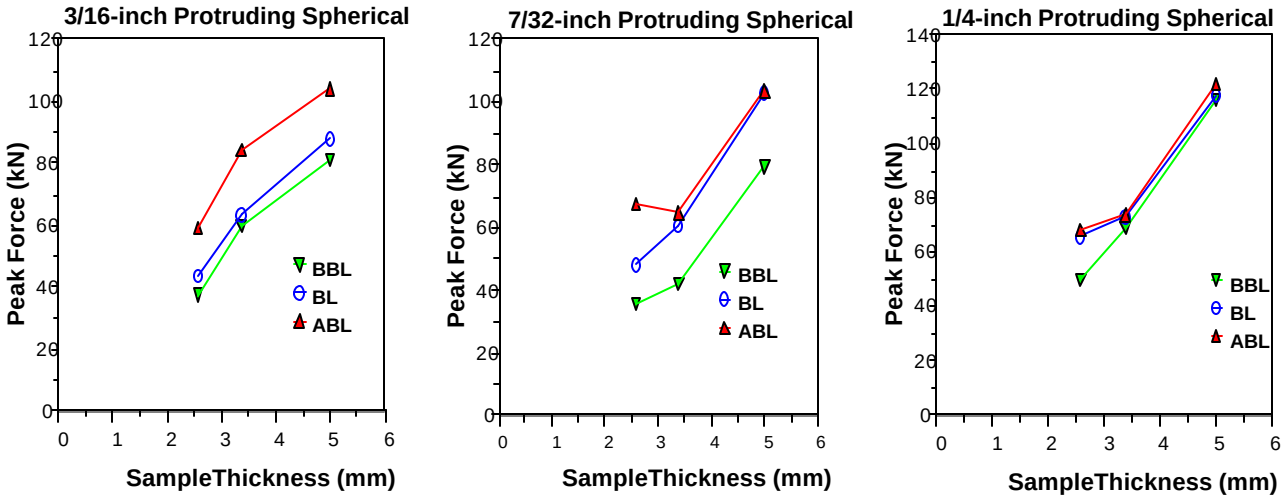

(a) (b) (c)

Figure 4.18 (a-c) Variation of sample thickness (12, 16 and 24 layer) on peak loading for different sized penetrators (3/16-, 7/32- and 1/4-inch).

5.0 EFFECT OF PENETRATOR GEOMETRY ON DYNAMIC FAILURE RESPONS OF GRAPHITE EPOXY (WOVEN) COMPOSITE AROUND THE CRITICAL PERFORATION ENERGY

5.1 3/16-inch Protruding Spherical and 3/16-inch Protruding Hemispherical Penetrator

In this section 3/16-inch spherical protruding penetrator will be compared to 3/16 –inch protruding hemispherical in terms of damage response parameter (below, at and above ballistic limit). The reason for doing this is to be able to characterize the behavior of each penetrator vis-a- vis the energy delivered to the specimen and how much will be retained it the specimen. The amount of energy retained in the specimen determines the level of deformation that the specimen suffers. The hypothesis here is that; any penetrator that delivers the highest energy to the specimen, should have more of energy absorbed thereby translating to greater level of specimen damage.

5.1.1 Energy Absorbed

Figure 5.1 compares the energy absorption of 3/16-inch protruding spherical penetrator to 3/16-inch protruding hemispherical penetrator. The result shows that 3/16-inch protruding spherical penetrator delivered highest energy to the specimen and it retained most of the energy. The wide gap in energy absorbed seen below the ballistic limit on 12 layers and 16 layers could be attributed to difference in energy level at which the experiment was performed. The protruding spherical can be seen absorbing energy continuously below and at ballistic limit. These behaviors may be attributed to the fact that after the crack has been opened by the

penetrator; the crack tends to close back after it has transverse the spherical end before transitioning into the protruding section.

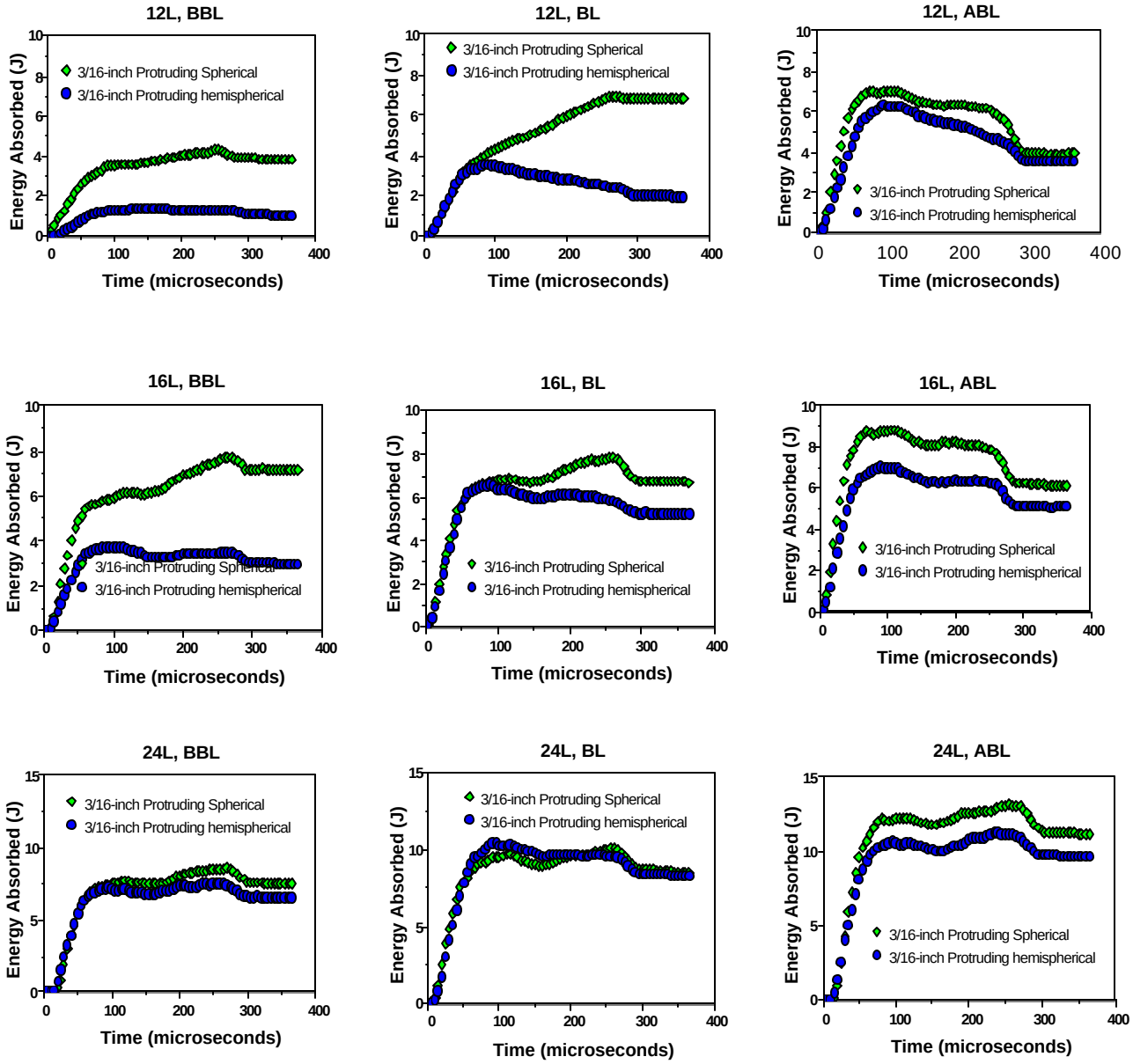

Figure 5.1 Comparison of energy absorption for 3/16-inch protruding spherical and 3/16-inch protruding hemispherical penetrators for 12-, 16-, and 24 –layer specimen at damage thresholds (below, at and above ballistic limit) energies.

Figure 5.2 shows the effect of penetrator geometry, the experiment was repeated at the same impact energy for both penetrators. This was done to be able characterize the specimen

damage response using same size of penetrator but different geometry (shape). At the first peak, which occurs at about 90 microseconds, both penetrators delivered almost the same amount of energy to the specimen. Characteristically of the protruding spherical penetrator it continues to absorbed more energy before failure. The gradual drop in energy absorbed by the 12 layer specimen noticed on the result for protruding hemispherical indicated that the specimen damage has been completed, because the specimen has been saturated and could not hold any more energy.

In conclusion, the 3/16-inch protruding spherical delivered the highest energy to the 12, 16 and 24 layer specimen and retain the most energy for all thickness used in this experiment.

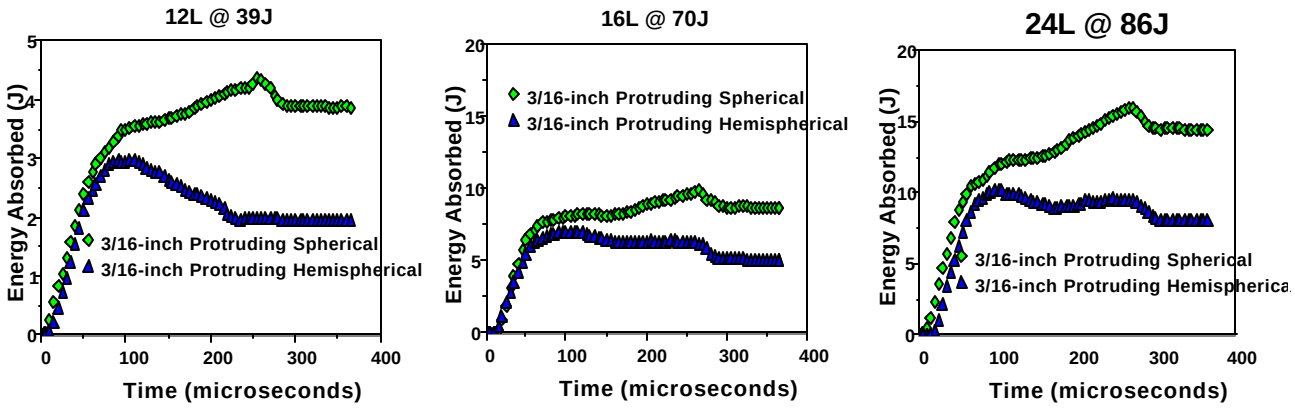

Figure 5.2 Comparison of energy absorption for 3/16-inch protruding spherical and 3/16-inch protruding hemispherical penetrators for 12-, 16-, and 24 –layer specimen at the same impact energies.

5.1.2 Strain rate-Strain

Typically, any specimen that absorbed the most energy should suffer more deformation because the amount of energy absorbed by a specimen determines the level of damage or deformation of the specimen. Figure 5.3 show that 3/16-inch protruding spherical penetrator generated the highest level of damage to all the specimens (i.e. 12, 16 and 24 layer). It also

consistently suffers the most damage (this evident from the strain on the specimen). The only exemption being at the ballistic limit for the 12-layer specimen. However, the hypothesis can be said to be true 90% of the time for the entire three specimens studied. The result also shows strain rate dependency on striker impact energy and on specimen thickness.

All specimens (12, 16 and 24 layer) reached their peak strain rate at about 80 microseconds and remain constant for about 200 microseconds during the perforation process. The difference in strain rate and strain value can be attributed to the difference in energy level for each damage threshold and it can also be as a result of penetrator geometry.

Figure 5.4 compares the strain rate – strain at the same energy. The result shows that spherical protruding penetrator generated the highest strain rate and strain on the specimen. This result shows clearly that penetrator geometry rather than energy has significant effect on specimen damage response.

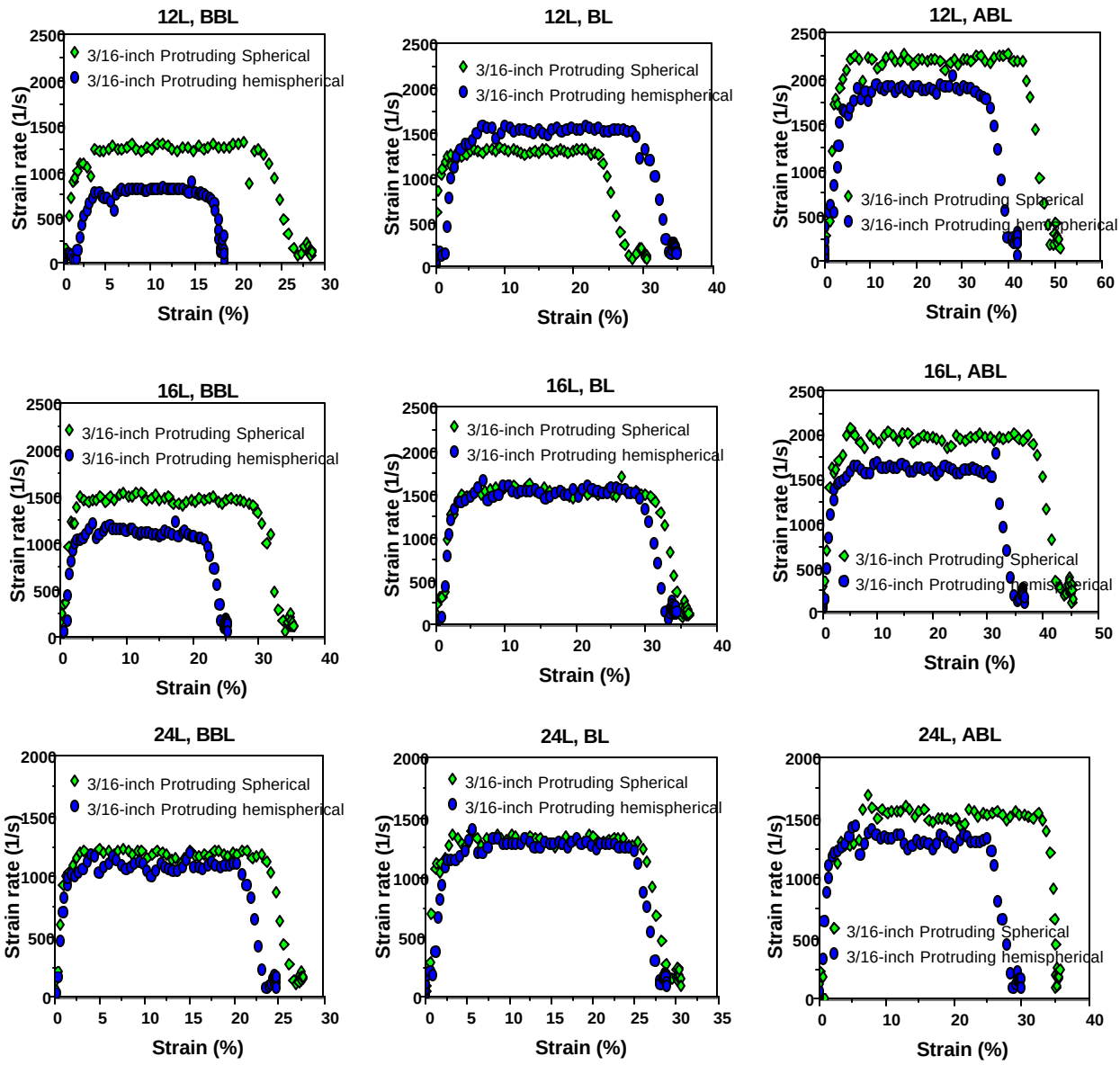

Figure 5.3 Comparison of strain rate – strain plot for 3/16-inch protruding spherical and 3/16-inch protruding hemispherical penetrators for 12-, 16-, and 24 –layer specimen at damage thresholds (below, at and above ballistic limit) energies.

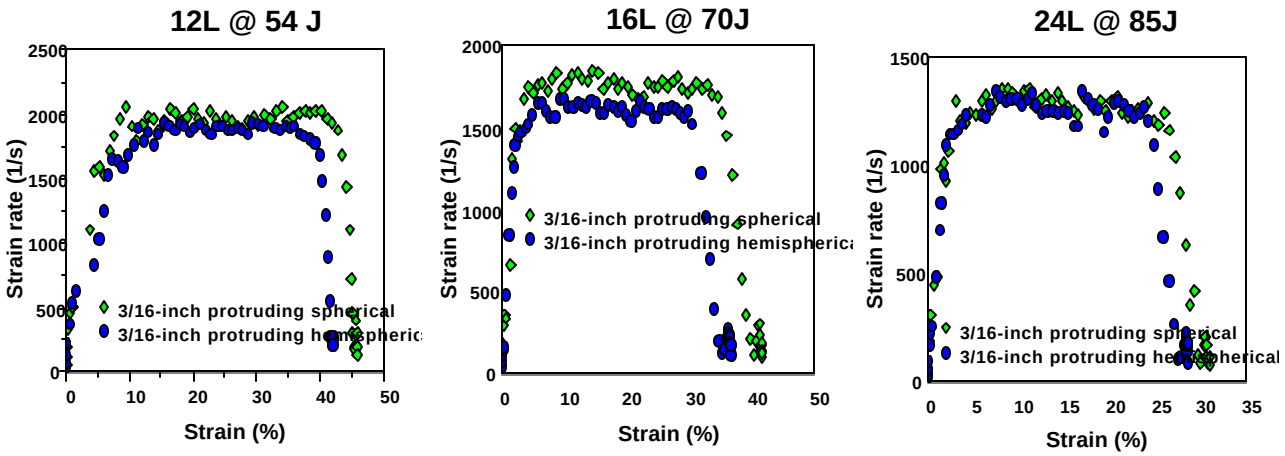

Figure 5.4 Comparison of strain rate – strain for 3/16-inch protruding spherical and 3/16-inch protruding hemispherical penetrators for 12-, 16-, and 24 –layer specimen at the same impact energies.

5.1.3 Force - Displacement

Figure 5.5 indicated that 3/16-inch protruding spherical penetrator released maximum load force on all the specimens in all the damage thresholds than the 3/16-inch protruding hemispherical penetrator. This behavior can be attributed to the shape of the penetrator contact end. This is because the spherical penetrator requires a higher energy to perforate it (see section 5.1.1.1).

Figure 5.6 shows the result of the experiment repeated for all the specimens (12, 16 and 24 layer) at the same impact energy using both penetrators. It can be seen clearly that the 3/16-inch protruding spherical also consistently delivered the maximum load to the specimen irrespective of their thickness. The maximum displacement value seen in the 12 layer specimen is due to the fact that, at the impact energy used for the comparison, 3/16-inch protruding hemispherical penetrator is at ballistic limit point while 3/16-inch protruding spherical suffered

penetration type damage. It is conceivable therefore that the maximum displacement value for the protruding hemispherical penetrator will be higher than protruding spherical.

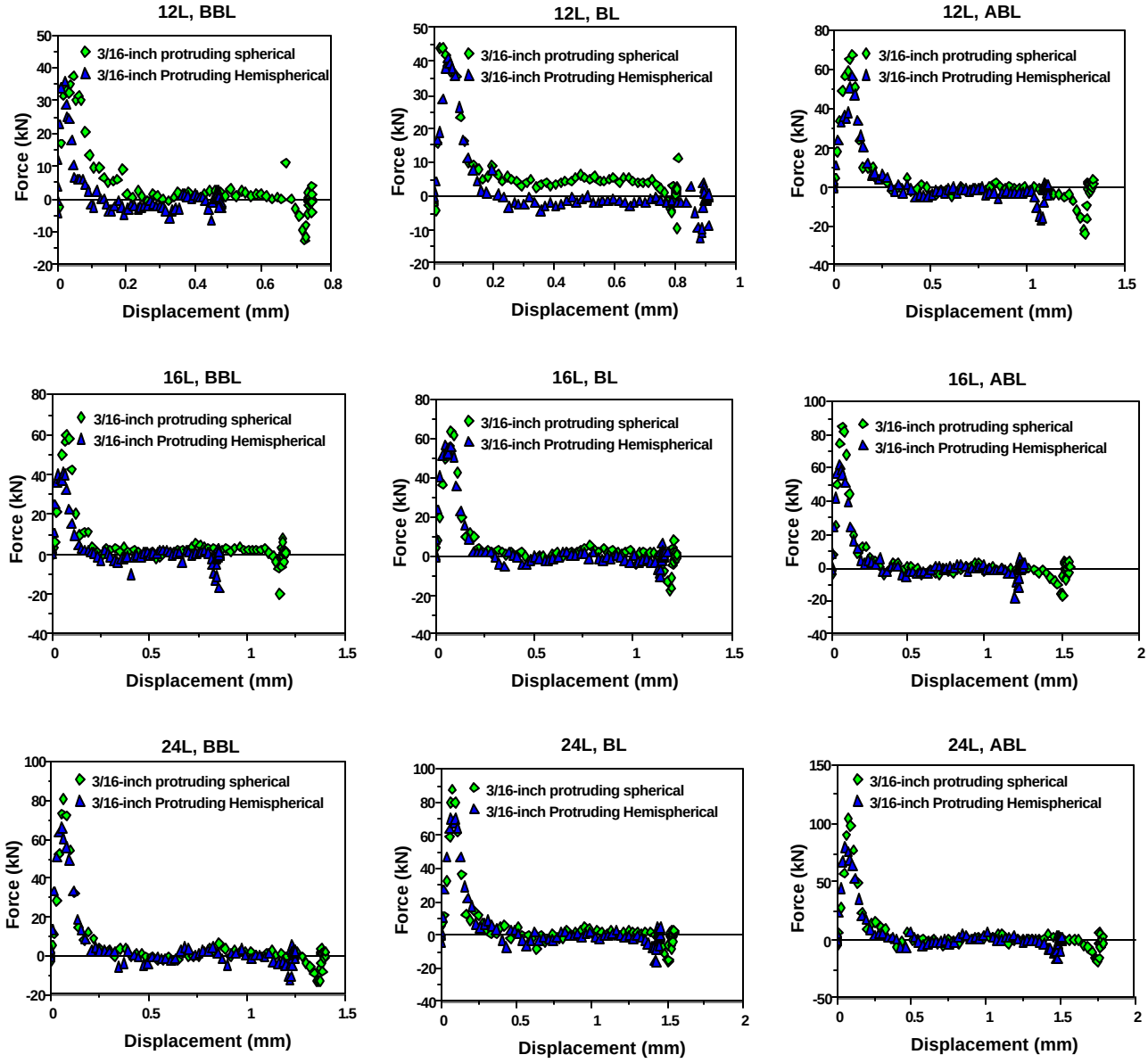

Figure 5.5 Comparison of force- displacement for 3/16-inch protruding spherical and 3/16-inch protruding hemispherical penetrators for 12-, 16-, and 24 –layer specimen at damage thresholds (below, at and above ballistic limit) energies.

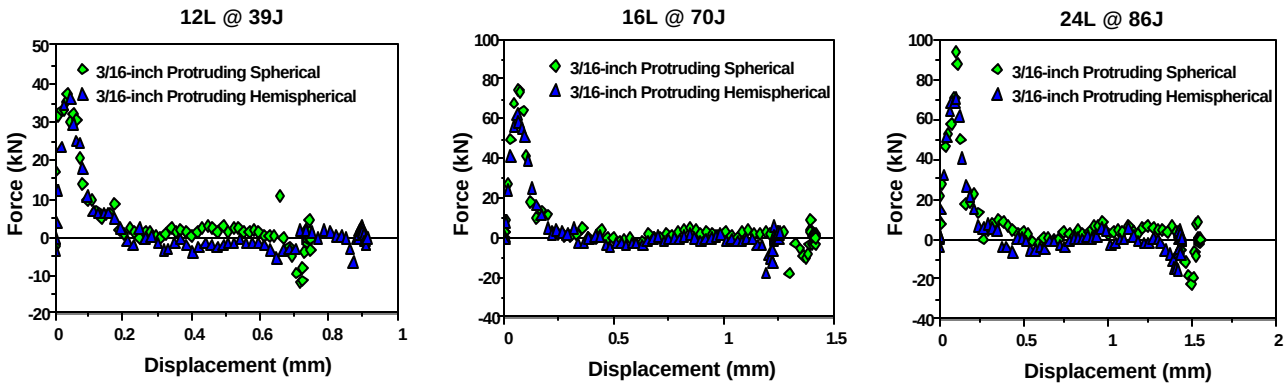

Figure 5.6 Comparison of energy absorption for 3/16-inch protruding spherical and 3/16-inch protruding hemispherical penetrators for 12-, 16-, and 24 –layer specimen at the same impact energies.

5.2 1/4-inch Protruding Spherical and 1/4- inch Conical Hemispherical Penetrators

The 1/4-inch protruding spherical is compared to 1/4-inch conical hemispherical penetrator so as to characterize their effect on the material behavior. The experiment was first run for the damage threshold considered (i.e. below, at and above ballistic limit), based on the data collected, the two penetrators responses were compared at the same impact energy, the result is presented below.

5.2.1 Energy Absorbed Profile

Figure 5.7 shows the specimen energy absorption for all the damage thresholds. It can be shown from the result shows that the conical hemispherical delivers more energy to the specimens for all the cases considered. There is a steady/uniform energy absorbed, for about 60 microseconds from when the specimen was penetrated (below this point depicts the elastic region). The summary plot shows that energy absorption increases linearly with incident energy levels with hemispherical nose penetrator delivering more energy for the same thickness.

Figure 5.8 compares the variation of energy delivered to the specimen by both penetrators at the same striker impact energy. Since both penetrators have the same contact surface area, it was hypothesized that they will deliver nearly the same amount of energies to the specimen at the same striker impact energy. This hypothesis was found to be wrong because looking at the result especially for the thicker specimen, the penetrators delivered different amount of energy to the specimen. The difference in energy delivered may not be unconnected to the shape of the penetrator. The conical hemispherical penetrator was found to deliver more energy to the specimen in all cases.

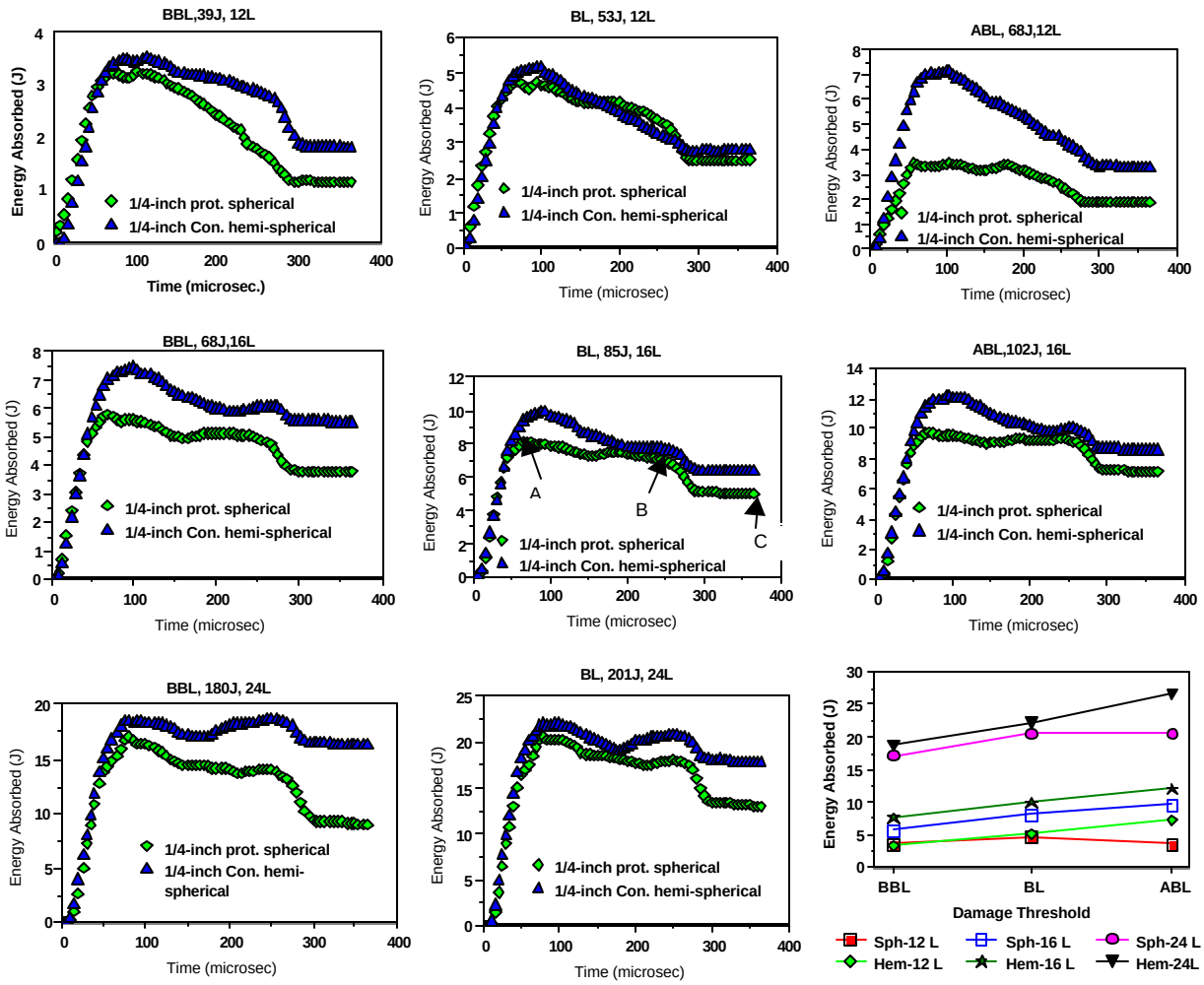

Figure 5.7 Comparison of energy absorption for 1/4-inch protruding spherical and 1/4-inch conical hemispherical penetrators for 12-, 16-, and 24 –layer specimen at damage thresholds (below, at and above ballistic limit) energies.

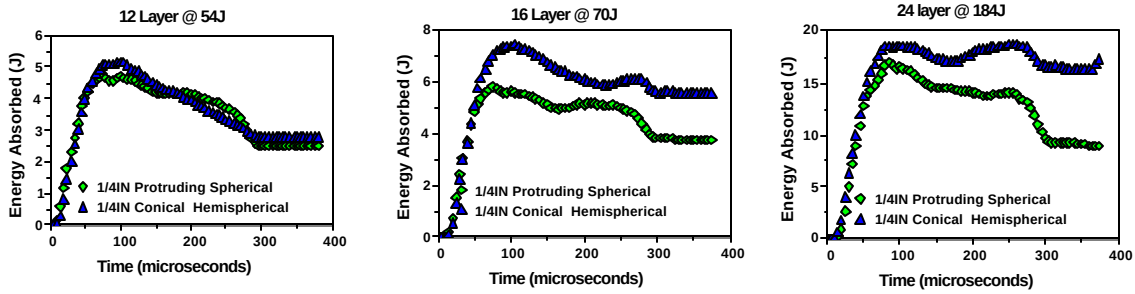

Figure 5.8 Comparison of energy absorption for 1/4-inch protruding spherical and 1/4-inch conical hemispherical penetrators for 12-, 16-, and 24 –layer specimen at the same impact energies.

5.2.2 Strain rate - Strain

Figure 5.9 shows the strain rate-strain plot, specimen damage 12 and 16 layer sample appears to be very close with the exemption of above ballistic limit for the 12-layer specimen. However the wide gap be seen on the 24 layer specimen for all the damage threshold can be attributed to the global damage effect of the conical hemispherical penetrator. Contributory factor to this behavior might not unconnected with the diameter of hemispherical-nosed of the penetrator (0.25-inch) which is thicker than the specimen (0.197-inch), the conical shape of the penetrator can be seen to take part in the deformation process right from the onset of damage initiation.

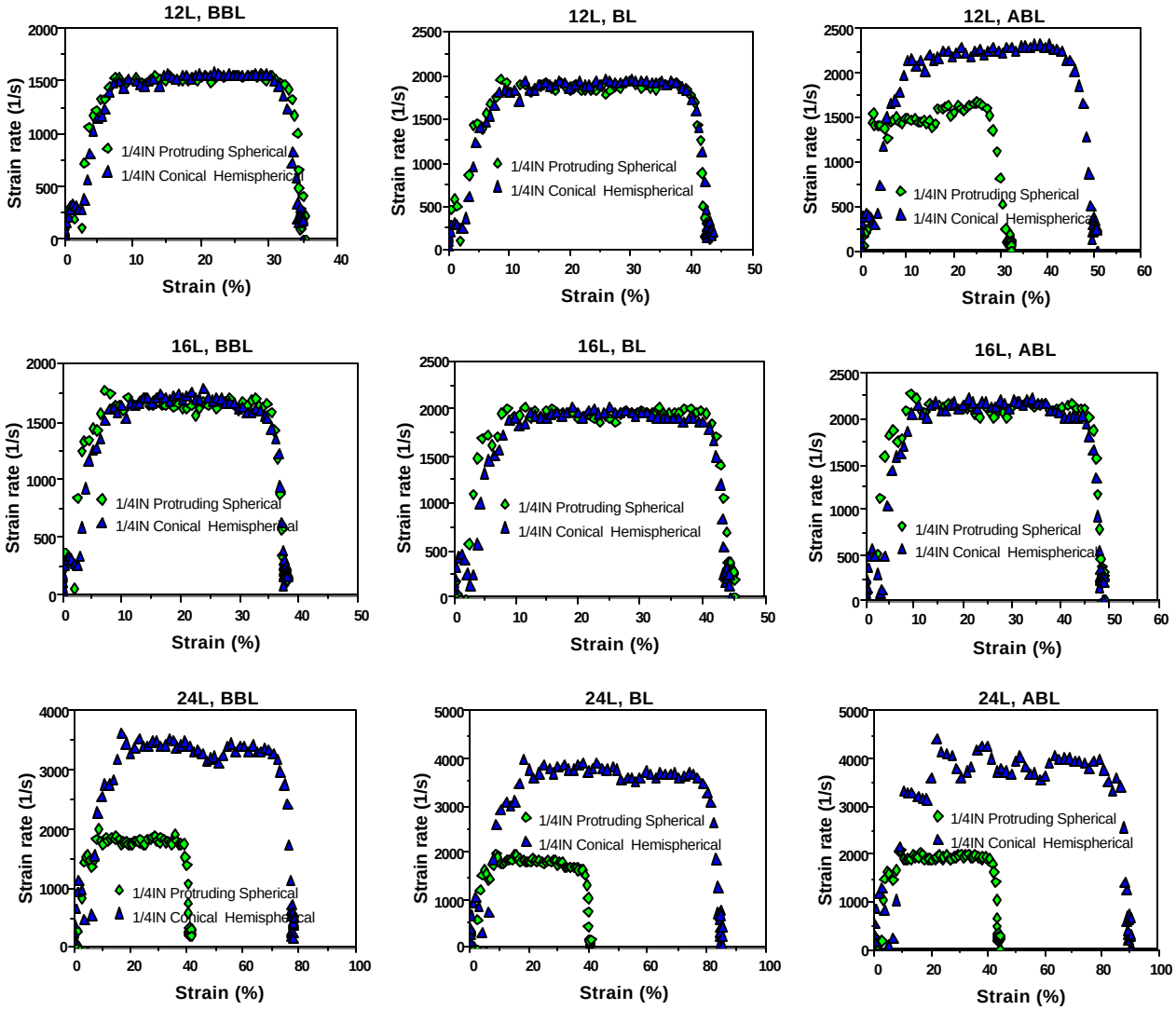

Figure 5.9 Comparison of strain rate - strain for 1/4-inch protruding spherical and 1/4-inch conical hemispherical penetrators for 12-, 16-, and 24 –layer specimen at the damage thresholds (below, at and above ballistic limit) energies.

Figure 5.10 compares the strain rate-strain plot at the same impact energy for each specimen thickness. The result shows that for 12 and 16 layer specimens both penetrator generated virtually same level of strain rate – strain damage in the specimen while in 24 layer, different level of damage specimen strain can be seen with conical hemispherical penetrator showing the highest damage to the specimen. This is as a result of the conical section of the

specimen taken part in specimen deformation because the diameter of sample thickness is bigger than penetrator nose diameter.

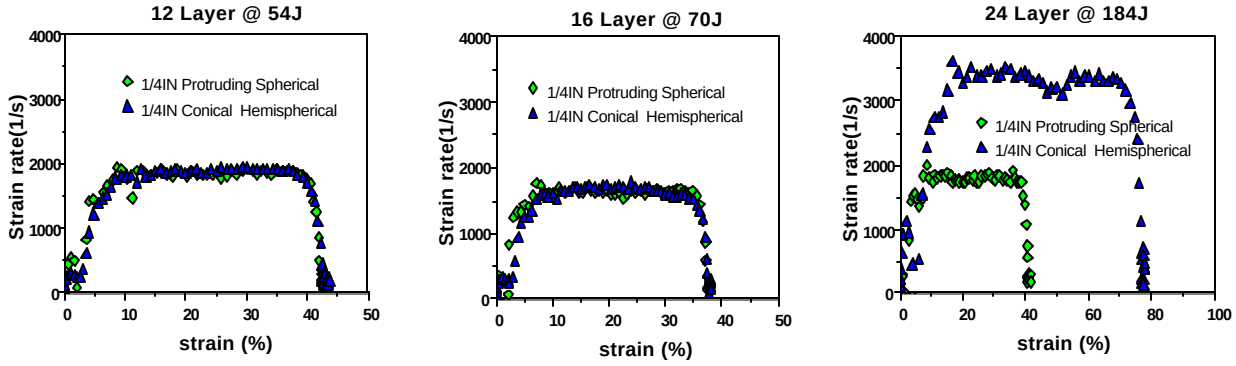

Figure 5.10 Comparison of strain rate – strain for 1/4-inch protruding spherical and 1/4-inch conical hemispherical penetrators for 12-, 16-, and 24 –layer specimen at the same impact energies.

5.2.3 Force - Displacement

The maximum loading force for both penetrator is as shown Figure 5.11, the result shows that the 1/4-inch protruding spherical penetrator delivered the highest loading force to the specimen in all the damage thresholds though this did not translate into more specimen penetration with exemption of 12 layer above ballistic limit and 24 layer at and above the ballistic. The reason being that the conical section restrict the movement of the penetrator into the specimen except when run way above the ballistic limit of the specimen.

Figure 5.12 compares the loading force for both penetrators at the same striker impact energy. It can be shown clearly that the spherical penetrator released the highest load on the specimen for all the specimen thickness but specimen displacement seems to be the same for both penetrators.

In Conclusion, conical hemispherical delivers more energy to the specimen and the net energy absorbed by the specimen is higher for this penetrator. Global damage effect is recorded

on thicker specimen because of the conical section of the penetrator. Strain rate is dependent on the sample thickness and also on the impact energy.

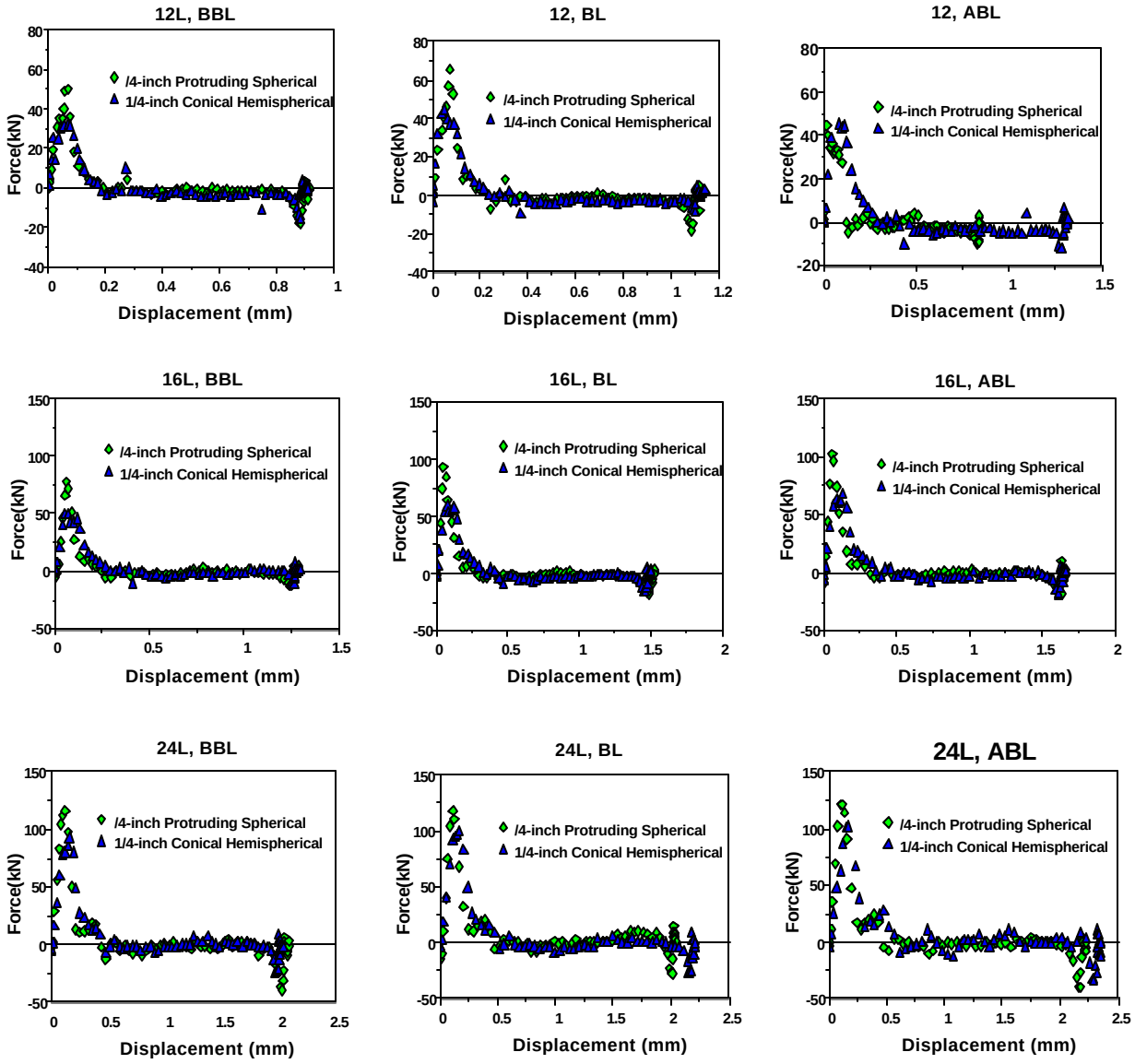

Figure 5.11 Comparison of force-displacement plot for 1/4-inch protruding spherical and 1/4-inch conical hemispherical penetrators for 12-, 16-, and 24 –layer specimen at the damage thresholds.

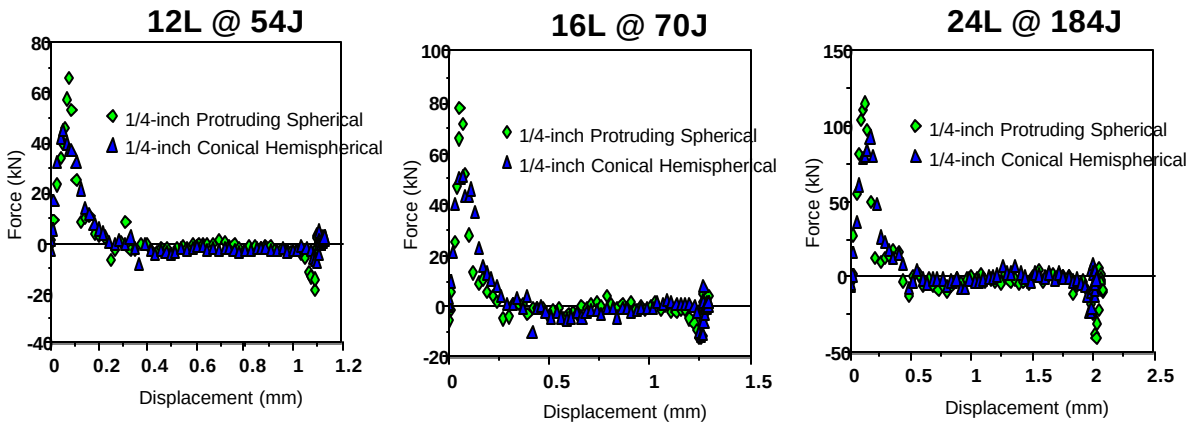

Figure 5.12 Comparison of force – displacement plot for 1/4-inch protruding spherical and 1/4-inch conical hemispherical penetrators for 12-, 16-, and 24 –layer specimen at the same impact energies.

Figure 5.13 compares the tensile strain released at the rear of a 16-layer specimen using 1/4-inch conical hemispherical penetrator at the damage thresholds (below, at and above ballistic limit). The objective of this is to see if damage to a specimen can be estimated based on the amplitude of tensile strain released at the specimen's rear. It can be shown that below or at the ballistic limit the tensile strain energy release is less apparently because below the ballistic limit the specimen absorbs most of the energy delivered. The damage is characterized by indentation and partial penetration at the most. At the ballistic limit, only a portion of the energy is released, therefore the strain energy dip is expected to be higher than below ballistic limit. The damage is characterized by slight perforation to the sample. Above the ballistic limit, it was hypothesized in this study that after the specimen has been damage any increase in striker impact energy would not result in appreciable more damage to the specimen. At best they will be absorbed by the system. It can be shown from the results that of all the energy available for deformation, some of it is lost to the system as indicated by tensile strain energy release (B) while the plateau after this point (C) signifies the energy absorbed by the specimen. This behavior agrees with our

hypothesis (see Figure 5.13). The damage to the specimen above the ballistic limit is characterized by perforation and plugging. Plugging here is defined as the stage where the conical section of the penetrator took part in the specimen damage. The damage is irrecoverable because some of the material will be lost in the process. This behavior is typical for all specimen thickness studied regardless of the penetrator size, shape or geometry. Thus, from this result, it can be concluded that the amplitude of strain release can be used to estimate amount of strain energy a material could withstand before failure [5].

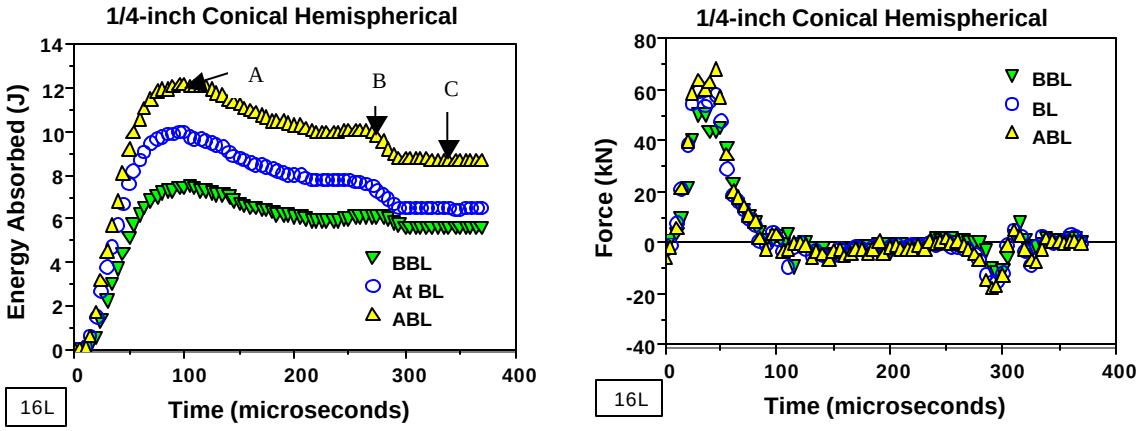

Figure 5.13 Tensile strain release at the damage threshold for 16-layer specimen using 1/4-inch Conical hemispherical penetrator (a) Energy Absorbed and (b) Force – time plot.

Figure 5.14 (a-b) shows the plot of force – time at different impact energies and force-time curve at the same impact energy level using the same penetrator. The amplitude of the tensile release wave was found to be dependent on the impact energy but it is independent on thickness of the specimen. The amplitude of the strain release by 16-layer specimen below ballistic limit is lower compared to the one released at the ballistic while the strain released above the ballistic limit is higher than the rest. This behavior is expected because below ballistic limit almost all the energy is used up in overcoming internal stresses in the specimen while at

ballistic limit, the specimen still used most of energy absorbed but since the specimen has suffered little perforation more strain energy will be released. Beyond the ballistic limit more of this energy is released to the system, force-time plot at the same energies buttresses the fact that strain release time at the same impact energies is independent of the specimen thickness as they all appear to occur at the same time and the amplitude are the same.

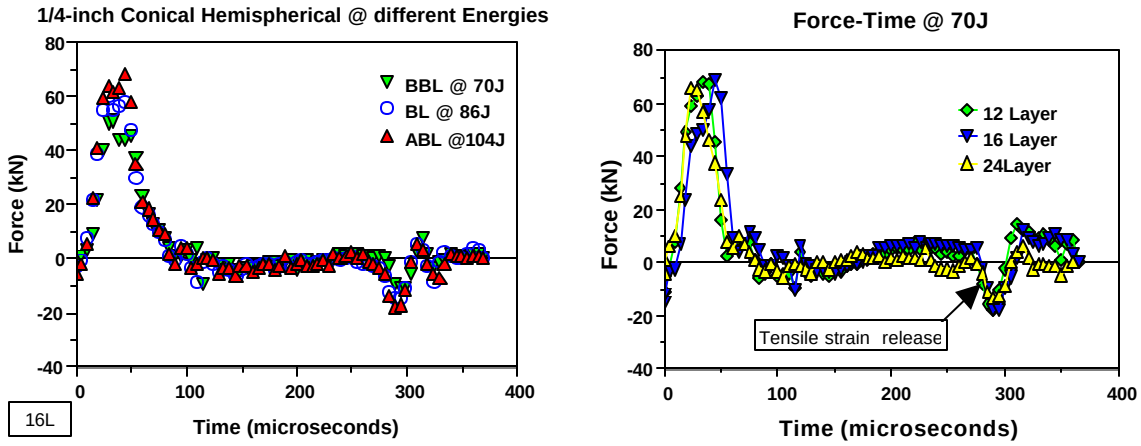

(a) (b)

Figure 5.14 Effect of sample thickness on tensile strain release for (a) Force – time at different impact energies, (b) Force – time at the same impact energy

In conclusion, it was discovered that as the projectile size increases the energy absorption rate of the composite material increases also. This is not unexpected because of the increase in the contact surface area of the projectile, which tends to distribute the incident energy over a wider area for the same amount of energy applied. Fiber stretching prior to perforation was noticed during the experiment. This could be attributed to shape of the projectile, which creates a hole that enlarges as the specimen is perforated. This position was supported by (M.V Hosur et al) among several researchers. Also increased in penetrator size or geometry increases the perforation threshold of the specimen significantly [5,17].

6.0 EFFECT OF SAMPLE THICKNESS ON THE SPEED OF CRACK PROPAGATION USING 1/4-INCH PROTRUDING SPHERICAL PENETRATOR WITH THE AID OF AN HIGH SPEED DIGITAL VIDEO IMAGING CAMERA

6.1 Introduction

Of utmost importance to a design engineer in specifying a component part is the material compressive and tensile resistance to applied load. Because dynamic impact are impulsive in nature, that is they act for a short period of time, characterizing the nature of damage in the affected region becomes imperative, for example bird strike in aircraft, storage of component parts. High compressive strength indicates a strong energy absorption rate of the composite part.

This study was carried out using a model 330 high-speed camera with a recording rate of 2 million frames per second. This helps to capture both the transverse and longitudinal crack propagation in the specimen.

6.1.1 Operation of model 330 camera

Figure 6.1 present the system configuration for the high-speed camera used for the experiment, which is part of the integrated operational layout for the penetrating split Hopkinson pressure bar (P-SHPB) presented earlier (see Figure 3.6). The model 330 camera is setup as an integral part of the whole experimental setup, rotated by gas control system model 476 via the camera control model 480. The trigger is connected to the camera via model 450 the 2- channel delay generator, which is integrated into a remote operation box. The flash is connected to the light source model 607 via BNC cable. The mirror in the camera is rotated by an air unit, which took its source from a 250HP compressor machine. The rate of data collection depends on the speed at which Camera Control model 480 is set to capture an event. It was found during the

course of this experiment that speed of rotation of the mirror is proportional to the impact energy. That is, the increase of one leads to the increase of the other.

To capture an event, the shutter button on remote fire unit is depressed and held down while the fire button is energized. The fire button energizes the quick acting solenoid valve which in turns opens up to allow the metered air to push the striker rod against the incident bar. The moment the striker rod impacts the incident bar, a high intensity flash produced by the light opens after a preset delay set on delay generator (this might vary depending on the impact velocity and the rate of capture of event) to illuminate the back of the specimen via 4 fiber optic cable connected to the specimen holder while the event is recorded on the film through the opened shutter on the 80 frames in the model 330 camera. The film is then developed in the laboratory and the crack propagation event captured on the film can be measured with the aid of a magnifier glass and venier caliper or appropriate measuring instruments.

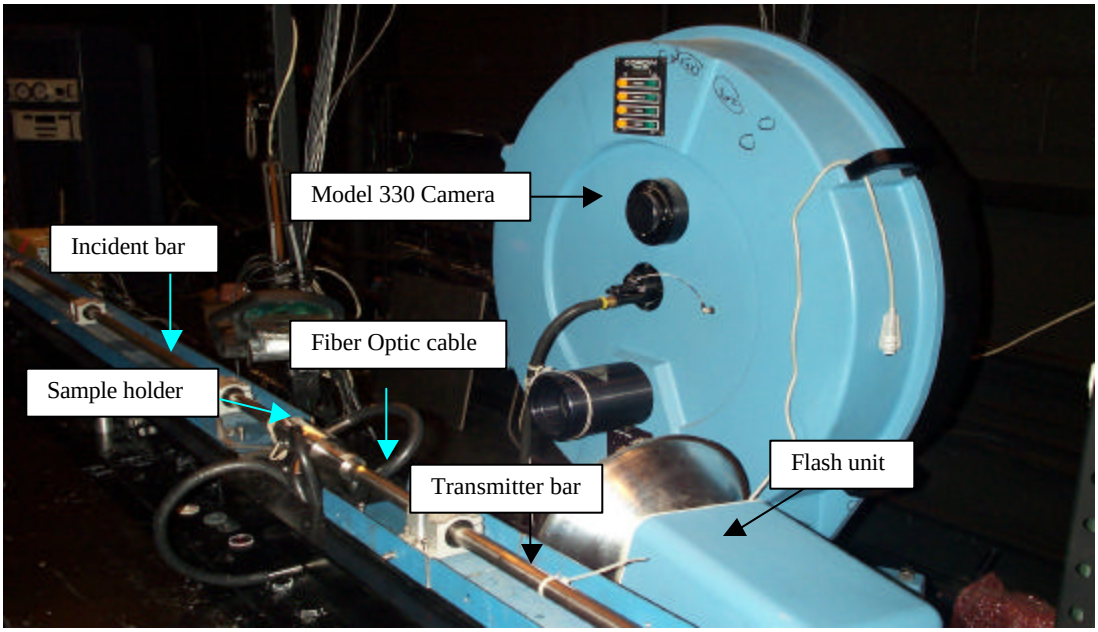

Figure 6.1 System configuration showing high-speed camera looking into sample holder illuminated by 5kV flash unit via fiber optical cables.

6.1.2 Calibration and magnification of the high speed camera

During the course of this experiment one of the difficulty encountered was the calibration of the model 330 camera to be able to capture the event at the right time which is very crucial to the crack propagation measurement.

A clear glass disc of the same dimension as the specimen was marked around the center with a red ink. This test piece was placed inside the test section (i.e. penetrator, sample holder and transmitter bar); light was flashed in by a floodlight and with the aid of a touch light. The light in the experiment room was shut off (for better contrast) and the back of the camera was opened so as to be able to locate the disc marking on the film reel of the camera. The sample holder was adjusted a couple of times before the right point is located and marked as reference point. Transverse and longitudinal movement clearances of test section was performed, it was discovered that while longitudinal clearance was about 1-inch on each side; transverse clearance is very small compared to the longitudinal, it is about 0.25-inch each way.

To determine the speed at which the camera mirror has to be rotated to capture the events, several experiments was run at the same impact energy while varying the speed of the camera until a satisfactory picture is recorded on the films developed. Also, the impact energy could be varied while maintaining a constant recording rate (speed of camera).

Figures 6.2-6.8 show the crack propagation of the different sized specimen thickness used for the experiment (i.e. 12, 16 and 24 layers) using the 1/4-inch protruding spherical penetrator at the damage thresholds (BBL, BL and ABL). The picture recorded on the high-speed camera was developed and digitized so that the speed of crack propagation can be measured. A preset marking (1cm) was marked on the specimen to serve as the reference for obtaining the magnification factor from the digitized picture of the event. A venier caliper was used to

measure the crack length on the original specimen while a ruler was used to measure the crack length on the film developed. The difference in crack size between each subsequent inter-frame picture divided by the inter-frame time gives the speed of crack propagation of the specimen.

Gpw12-51a, Below BL, 60 J

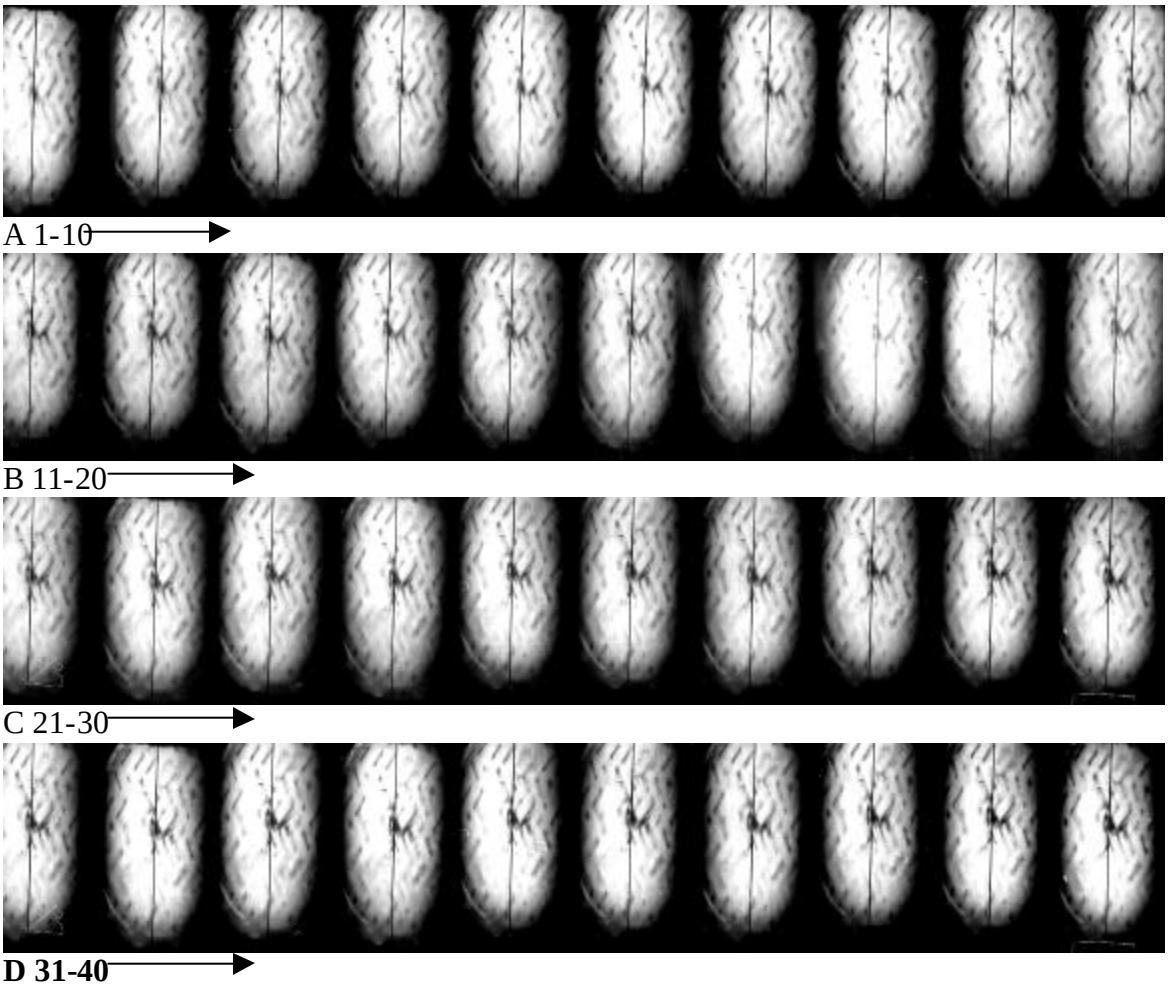

Figure 6.2, Crack propagation for 12-layered woven graphite-epoxy specimen below ballistic limit velocity using 1/4-spherical penetrator at 60J Below BL impact energy

Gpw12-67a, Above BL, 68 J

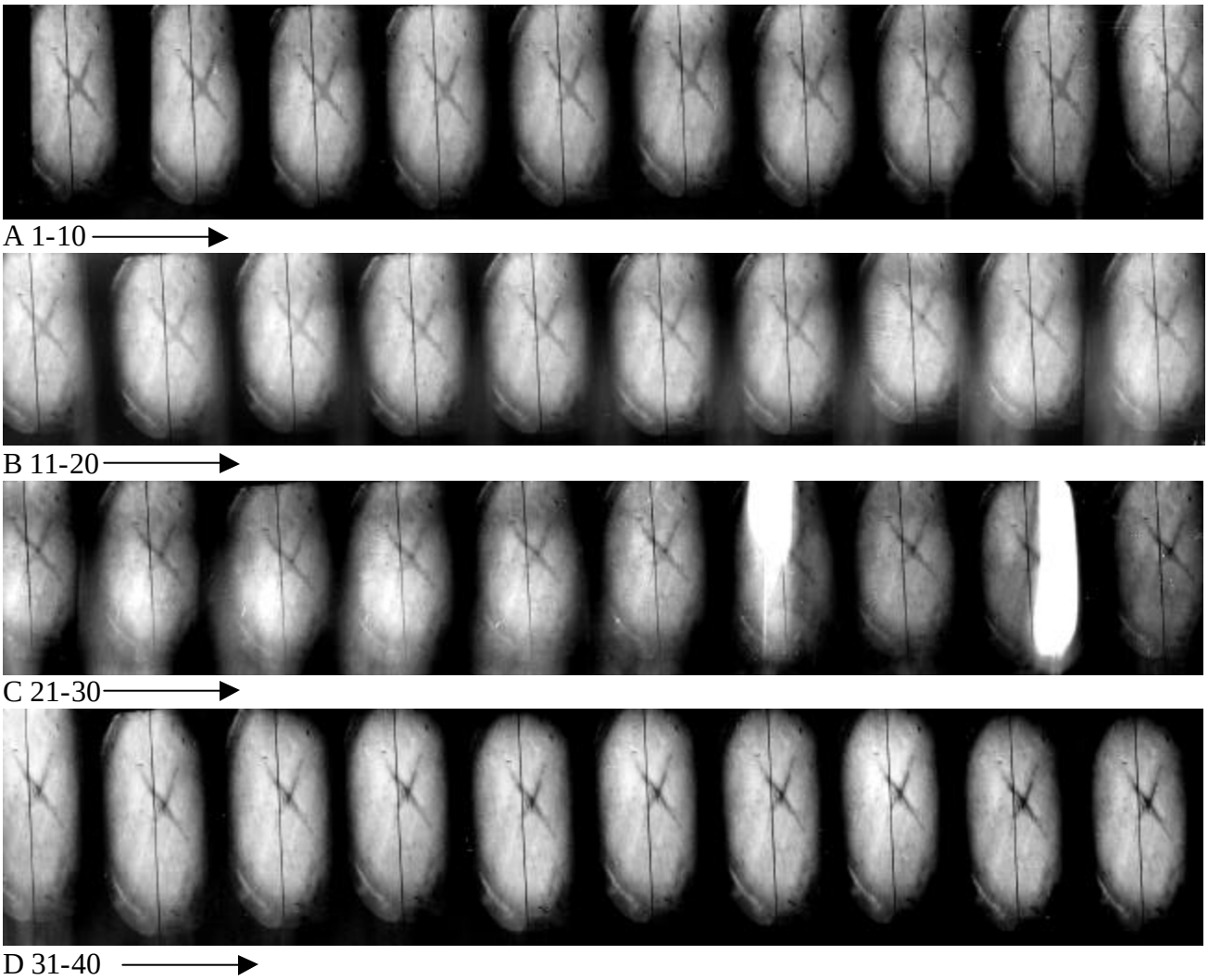

Figure 6.3 Crack propagation for 12-layered woven graphite-epoxy specimen at ballistic limit velocity using 1/4-inch spherical penetrator at 68 J above BL impact energy

Gpw16-75a Below BL, 68 J

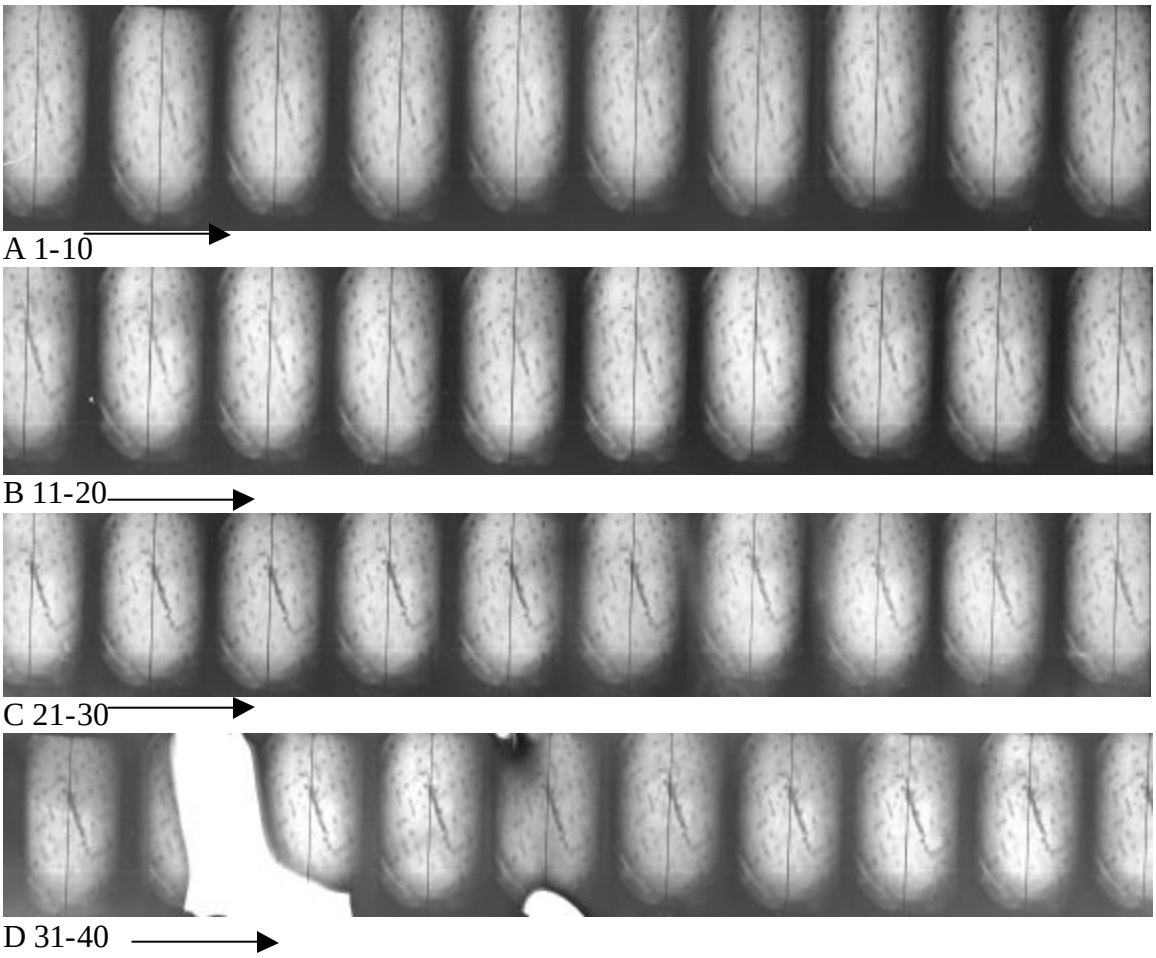

Figure 6.4, Crack propagation for 16-layered woven graphite-epoxy specimen below ballistic limit velocity using 1/4-inch spherical penetrator at 68J

Gpw16-92a, BL, 76J

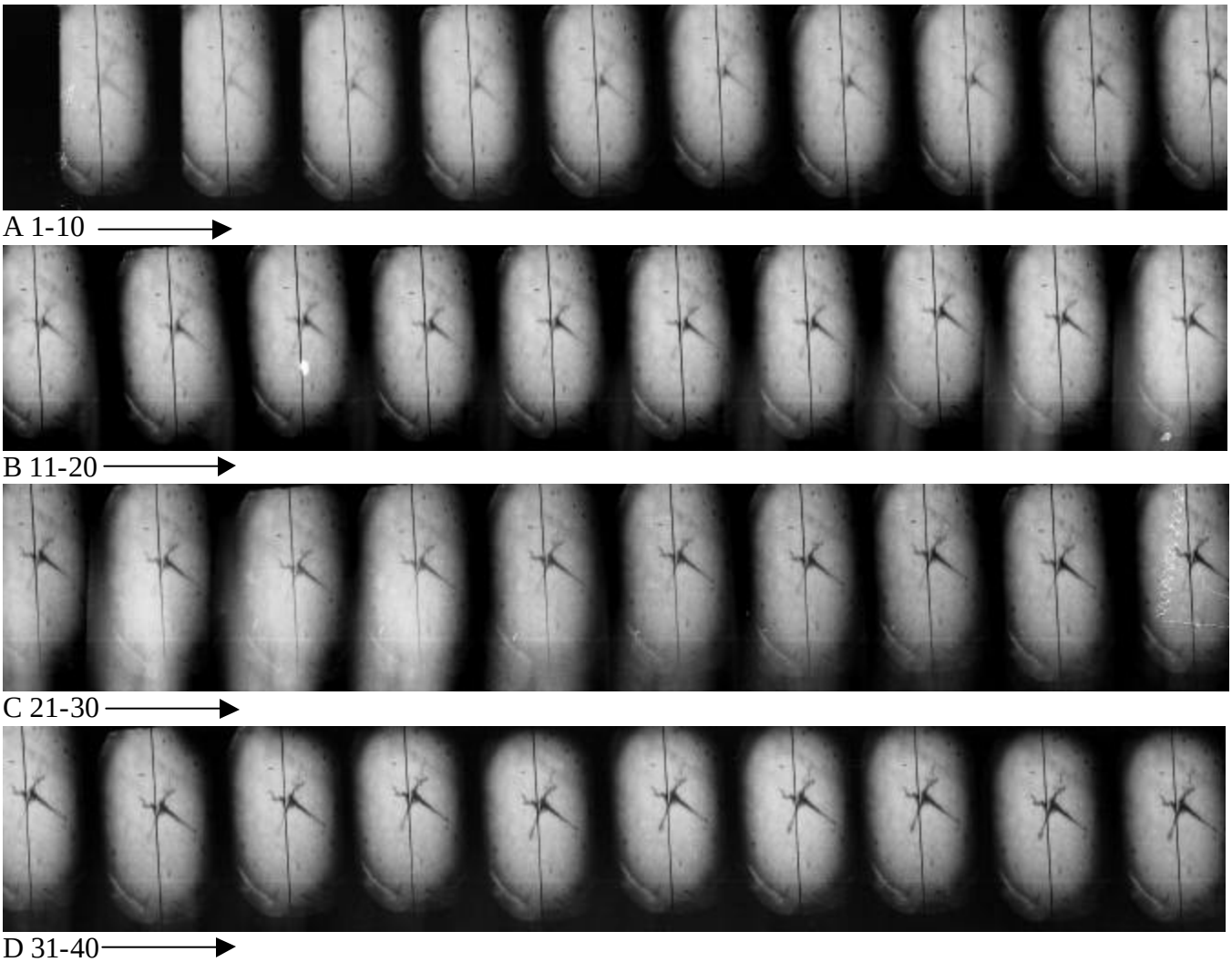

Figure 6.5 Crack propagation for 16-layered woven graphite-epoxy specimen at ballistic limit velocity using a 1/4-inch spherical penetrator at 76J impact energy

Gpw16-45a Above BL, 85J

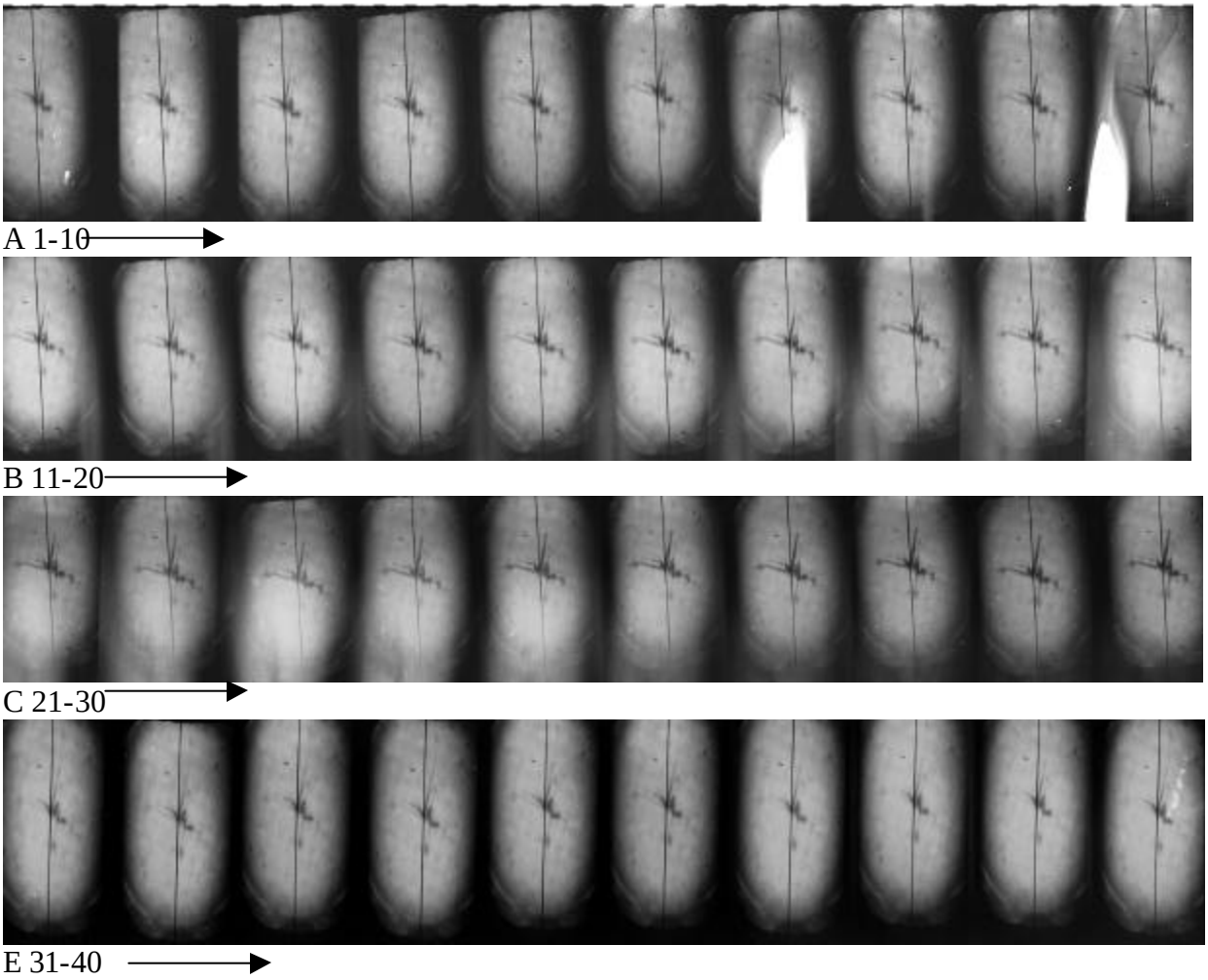

Figure 6.6, Crack propagation for 16-layered woven graphite-epoxy specimen above ballistic limit velocity using a 1/4-inch conical hemi-spherical penetrator at 85J BL impact energy

Gpw24-41, Below BL, 180 J

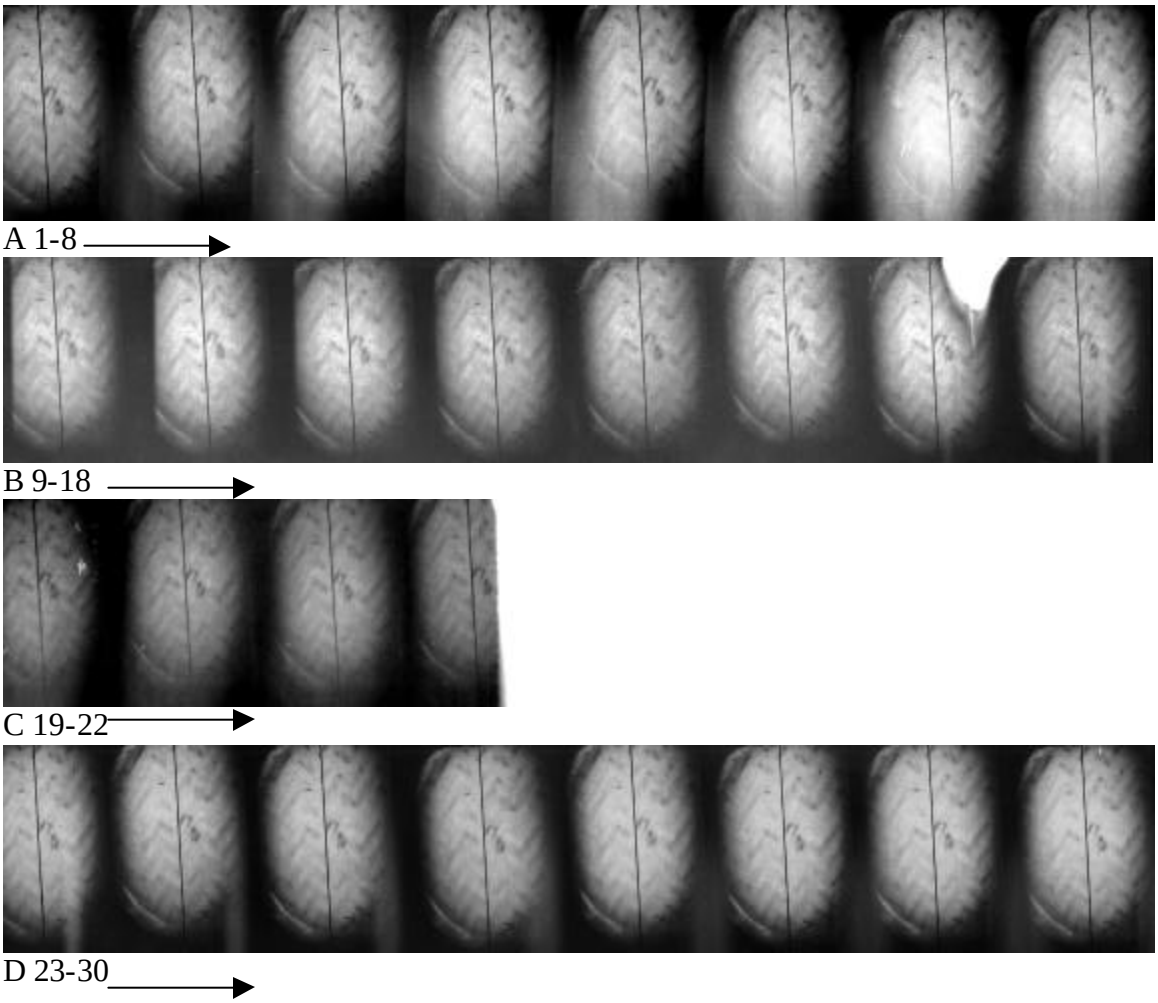

Figure 6.7 Crack propagation for 24-layered woven graphite-epoxy specimen below ballistic limit velocity using a 1/4-inch conical hemi-spherical penetrator at 180 J BL impact energy

Gpw24-09a, At BL, 201 J

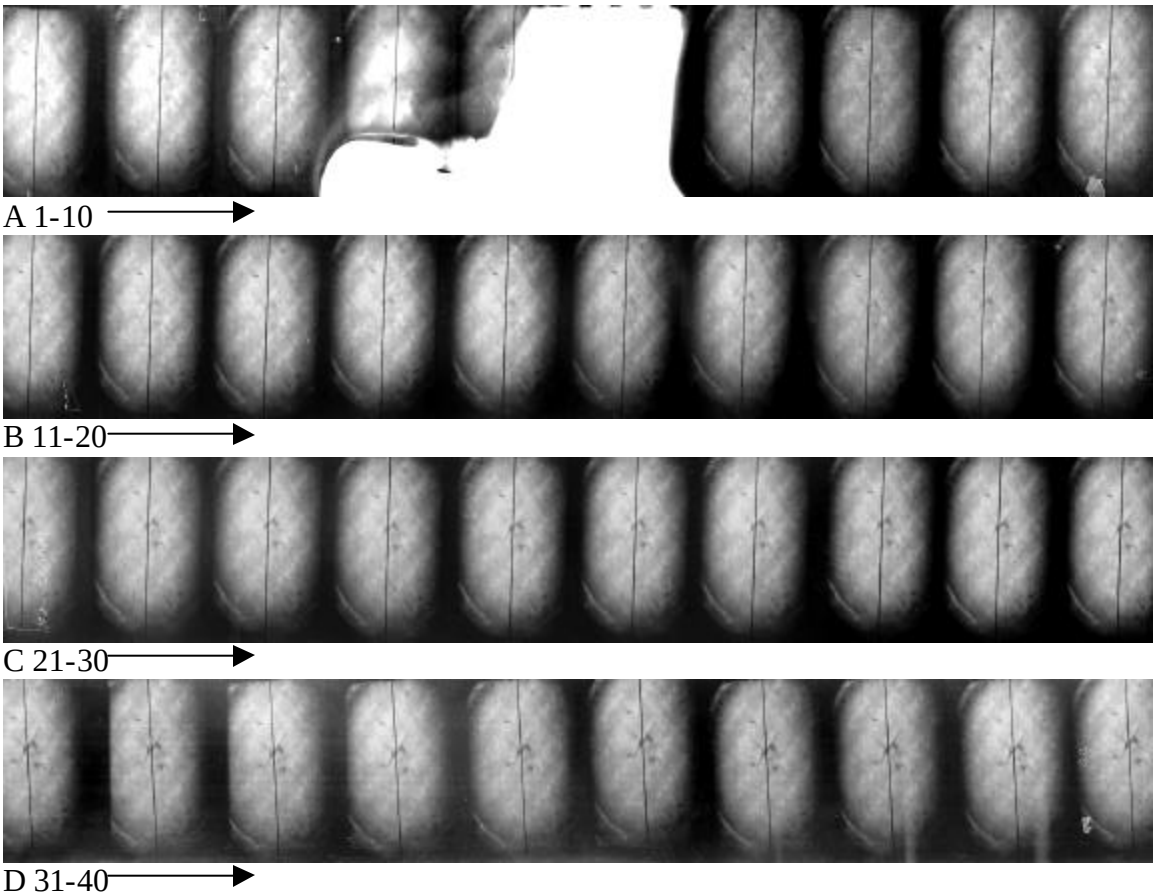

Figure 6.8, Crack propagation for 24-layered woven graphite-epoxy specimen above ballistic limit velocity using a 1/4-inch conical hemi-spherical penetrator at 201J BL impact energy.

The result shows that crack propagation increases as the damage threshold increases. From the physical measurement of the cracks, it was noticed that the speed of crack propagation below the ballistic limit was small (typical damage at this point is fiber stretching/bulging accompanied by fiber breakage at the rear) this is evident from the pictures as the crack length seems not to grow as such in between the inter-frames. This reason for this could be as a result of low velocity at which the striker bar impacts the specimen below the ballistic limit. However, at the ballistic limit, the crack can be seen to propagate faster especially with the 12 layer specimen

followed by the 16 layer specimen while the speed of crack propagation for 24 layer specimen is lower. Evidently, this is as a result of the specimen thickness (typical damage is penetration with slight perforation accompanied by fiber breakage with fiber still attached to the specimen.

The cross-like specimen crack propagation in both direction was observed, this might be as result of the woven nature of the specimen and the fact that one crack travels faster than the other depicts uneven nature of strain intensity of the woven specimen. It also shows that the point of intersection of the weave will also indicate the point of weaker or highest strain for the same energy.

In conclusion, the speed of crack propagation depends on the impact energy but it depends more on the specimen thickness.

6.2 Effect of penetrator geometry on speed of crack propagation around the ballistic limit using the high-speed CCD intensifier camera

Figures 6.9 and 6.10 presents the crack propagation results for both 1/4-inch protruding spherical and 1/4-inch conical penetrator using the model 220 CCD camera. A preset marking (10mm) was marked on the specimen to serve as the reference for obtaining the magnification factor from the digitized picture of the event. The measurements involve measuring the event at two pre-selected times. Two static shots—one before and other after the event—are taken for characterization of the complete penetration failure. The event is time-delayed for 900μ s delays plus a total of 260 μs event times. This allowed 800 μs for the wave to reach the specimen and extra 260 μs for damage process. The speed at which crack travels in the woven specimen was found to be very low, this might not be unconnected to the woven nature of the specimen that impedes crack propagation in the specimen or may be the camera timing was not accurate to take

picture when the crack has fully developed. However, on the average, the crack speed increases for both penetrators as the damage threshold increases. This however does not translate into a greater specimen damage by the conical hemispherical penetrator as the crack speed in spherical penetrator seems to travel faster thereby inducing greater damage into the specimen. One reason can be because of the conical section of the penetrator, which restricts the penetrator from moving further into its target.

A. Below BL

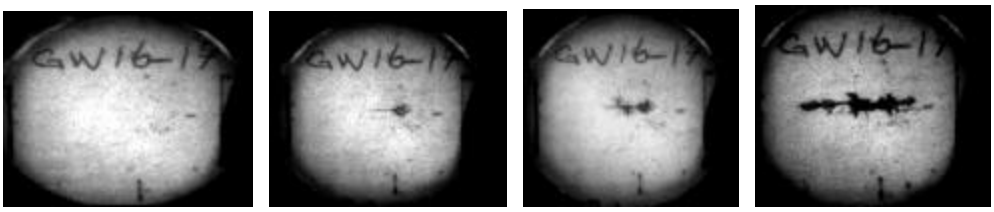

25 psi: Before 160 µs 260 µs Static

B. At BL

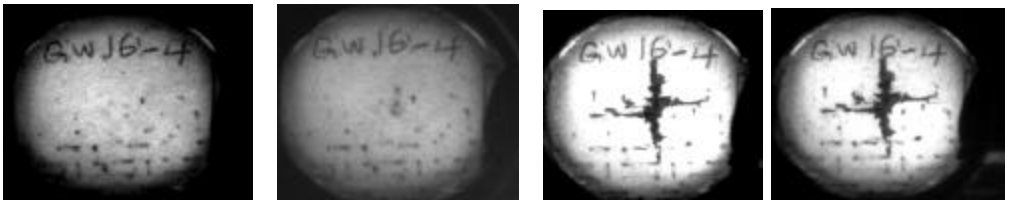

32.5 psi: Before 160 µs 260 µs Static

C. Above BL

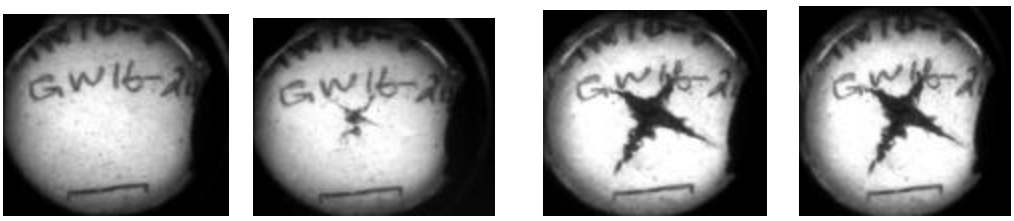

35 psi : Before 160 µs 260 µs Static

Figure 6.9 Crack propagations using high-speed video model 220 CCD Camera and a picture of 1/4-inch protruding spherical penetrator (25 psi=54J, 32.5 psi=76J and 35 psi= 84J of striker impact energies)

A. Below BL

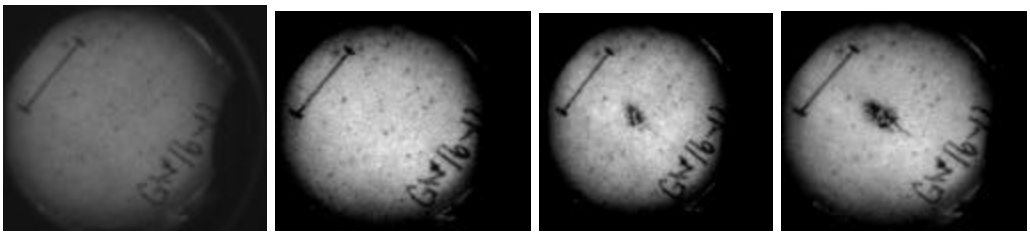

25 psi : Before 160 μs 260 μs Static

B. At BL

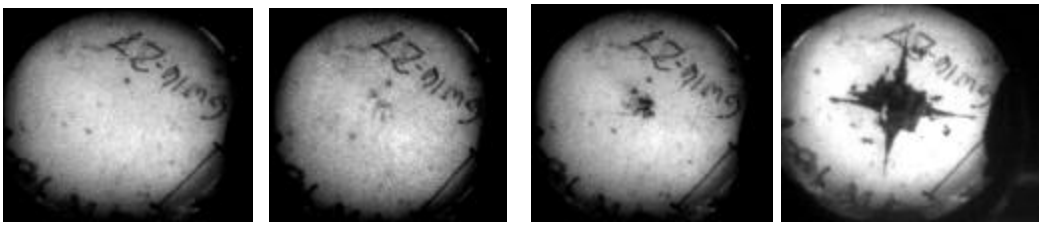

B 32.5 psi: Before 160 μs 260 μs Static

C. Above BL

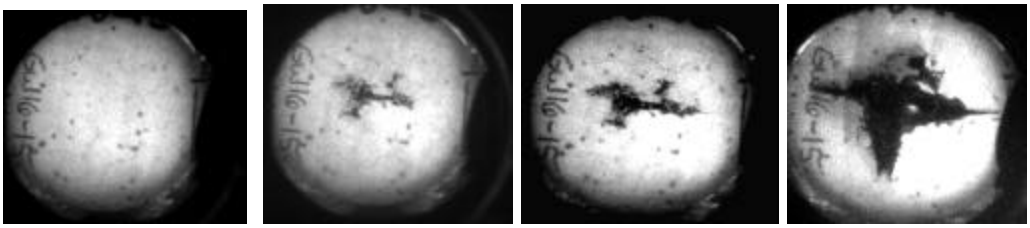

C 35 psi: Before 160 μs 260 μs Static

Figure 6.10 Crack propagations using high-speed video model 220 CCD Camera and a picture 1/4-inch conical hemispherical-nosed penetrator (25 psi=54J, 32.5 psi=76J and 35 psi= 84J of striker impact energies)

Figure 6.11 compares the average speed of crack propagation for both penetrators, the result show that crack propagates faster in protruding spherical than the conical hemispherical, the reason for this has been covered in the above section.

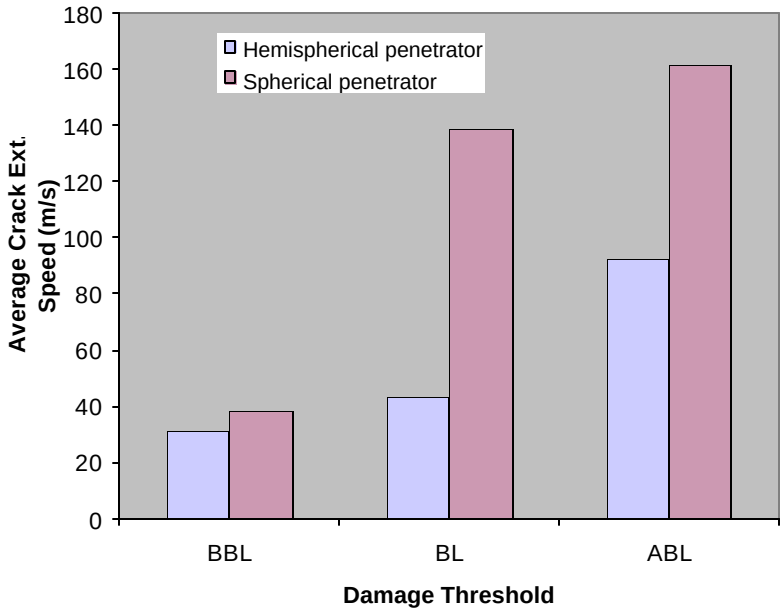

Figure 6.11 Comparison of average crack speed around the ballistic limit energies for conical hemispherical and protruding spherical penetrators

7.0 CONCLUSIONS

Below are the conclusions made from this thesis experiment:

1) As the projectile size increases the energy absorption rate of the composite material increases also, though the increase is not linear. This is not unexpected because of the increase in the contact surface area of the projectile, which tends to distribute the impact energy over a wider area for the same amount of energy applied.

2) The nature of specimen damage depends on the penetrator geometry, for example while the damage configuration impacted by a protruding hemispherical penetrator is highly localized, conical hemispherical penetrator impacts a global damage into its target because of the conical section of the projectile.

3) For the effect of penetrator size: at the same impact energy, the 3/16-inch protruding spherical penetrator delivered highest amount of energy to the specimen and the specimen in turn absorbed or retained more energy with this penetrator.

4) For the effect of penetrator geometry: comparing the 3/16-inch protruding spherical and 3/16-inch protruding hemispherical at the same impact energy, the 3/16-inch protruding spherical consistently released the highest energies into the specimen and the specimen absorbed more energy using this penetrator.

5) For the effect of penetrator geometry: comparing 1/4-inch protruding spherical and 1/4-inch conical hemispherical penetrator, the conical penetrator delivers the highest energy into the specimen and the specimen also retained more energy within.

6) Increase in damage threshold was found not have significant effect on the ratio of strain rate to strain for all the sample thickness.

7) The average ratio of strain rate to strain is a constant which independent of damage threshold but it is dependent on the material property of the specimen.

8) The result shows that as the penetrator size increases the penetration and perforation threshold energies increases significantly regardless of the penetrator geometry.

9) The results indicate high ballistic limit energies for the conical hemispherical penetrator for all the specimen thickness followed by the protruding spherical penetrator and lastly the protruding hemispherical used for this study. The thicker the specimen the higher the ballistic limit.

10) The crack propagates in both directions for the woven specimen in a cross-like manner owing to the woven nature of the specimen. The crack was observed to travel at different speed depicting the uneven nature of the strain intensity.

11) From the experiment, the result indicate that specimen strain rate depend to large extent on the penetrator size and configuration (shape). Increase in penetrator size increases the strain on the specimen but the increase is non-linear

12) Strain rate does not only depend impact energy, it also depend on the sample thickness irrespective of the penetrator size and shape. At the same energy level, strain rate was found to decrease as the specimen thickness increases.

This work validates our hypothesis that, penetrator geometry affects to a reasonable extent the damage response of a specimen when impacted. Also the waveforms can reasonably be used to determine the level of damage to the specimen (i.e. if a specimen is perforated or not).

APPENDIX

Appendix I

Figure I.1 and Figure I.2 shows the Hopkinson bar apparatus and complete layout of the hammer assembly respectively.

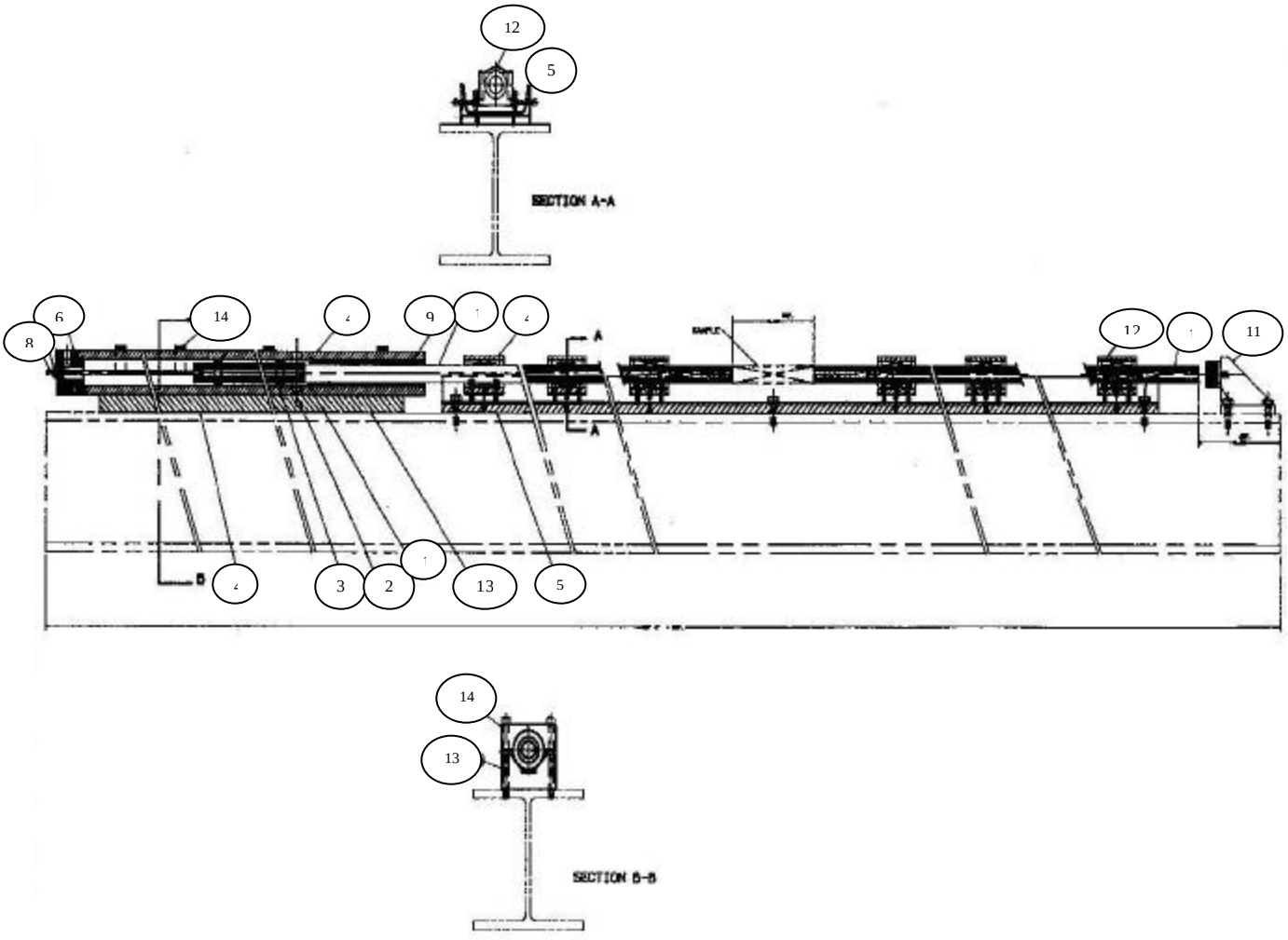

Figure I.1 Complete layout of the Hopkinson bar apparatus

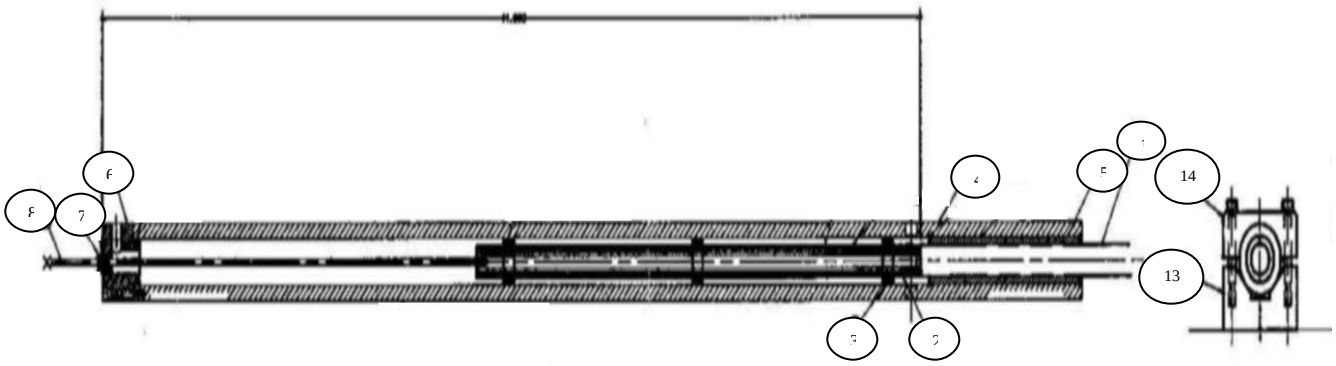

Figure I.2 Hammer assembly

List of components parts in the assembly:

1. Incident and transmitter bar
2. Striker rod
3. Piston
4. Receiver
5. U-shaped channel
6. End cap
7. Pull rod packing
8. Pull rod or retractor rod
9. Guide bushing

11. Stopper
12. Pillow blocks
13. Cradle
14. Saddle clamp

BIBLIOGRAPHY

1) Zukas, Jonas A., H. F. Swift, L.B Greszczuk Impact Dynamics. (Florida: Krieger Publishing Company, 1992)

2) Meyers, Marc Andre, Dynamic Behavior of Materials (New York: John Wiley & Sons, Inc., 1994)

3) Daniel, Isaac M. and O. Ishai, Engineering Mechanics of Composite Materials (New York: Oxford University Press, 1994)

4) Tsai, Stephen W. and H.T. Hahn, Introduction to Composite Materials. (Basel: Technomic Publishing Company Inc., 1980)

5) Nwosu, S.N., S.K Sivapuram, P.K Dutta and D. Hui, "Hopkinson Bar Perforation of Laminated Composite," Final report, Dillard University, 1997

6) Nwosu, S.N. and D. Hui," Use of Composites in Infrastructure," Advanced Multilayered and Fiber-Reinforced Composites, Kluver Academic Publishers, 1998. pp 3-11

7) Cantwell, W.J. and J. Morton," The Impact Resistance of Composite Materials- a review," Composites, Vol. 22, No. 5 (September 2001), pp 348-350

8) Cantwell, W.J. and J. Morton," Comparison of the Low and High Velocity Impact Response of CFRP," Composites, Vol. 20, No. 6 (November 1989), pp 545-551

9) Raju, Basavaraju B. and D. Liu, "Thickness Effects on Impact Response of Composite Laminates," Proceedings of the 13th Annual Technical Conference on Composite Materials, (September 21-23 1998) pp 1-14.

10) Schoeppner, G.A. and S. Abrate, "Delamination Threshold Loads for Low Velocity Impact on Composite Laminates," Composites Part A 31, (2000) pp 905-910.

11) Tanoglu, M. and S.H. McKnight," A New Technique to characterize the Fiber Interphase properties under high Strain Rates," Composites Part A 31, (2000) pp 1127

12) Caprino, G. and A. Langella, "Elastic behavior of circular composite plates transversely loaded at the center," Composites Part A 33, (2002) pp 1191-1193

13) Nwosu S.N, Hosur M.V, S. Jeelani, U.K Vaidya, Ajit D. Kelkar, "Survivability of Affordable Aircraft Composite Structures", Interim TechnicalWork Status Report for Research Project (April-September 2002)

14) Dahsin. Liu, Todd Richman, Guojing Li and Basavaraju Raju, "Penetration and Perforation Thresholds of Laminated Glass/Epoxy Composite Plates," Department of Materials Sciences and Mechanics, Michigan State University.

15) Marshall, P. and J. Price,"Fibre/Matrix Interface Failure controlled by a critical Energy Criterion," Composites, Vol. 22 No. 6 (November 1991) pp 445-447.

16) Foley, M.E. and S.H. McKnight," Fiber/matrix interphase characterization using the dynamic interphase loading apparatus," Composites Part A 33, (2002) pp 1345-1347

17) Liu, Dashin and B.B. Raju, "Thickness Effects on Impact Perforation Resistance of Composite Laminates," Symposium on Recent Developments in the Study of Impacts on Composite Materials, (June 1999) pp 1-2

18) O. Akil, U Yildrin, M Guden and I.W H Effect of strain rate on the compression behavior of a woven composite fabric S2-glass fiber reinforced vinyl ester composite, Polymer Testing, pp 1-5, February 2003

19) Sjoblom, Peter O. and J.T Hartness," On Low-Velocity Testing of Composite Materials," Journal of Composite Materials, Vol. 22 (January 1988) pp 39-43.

20) Zavattieri, Pablo D. and H.D. Espinosa, "Energy Dissipation in Ballistic Penetration of Fiber Composites," Project, Northwestern University, (1999) pp. 1-6

21) Akthar S. Khan, Ozgen U. Colak and Prabhakaran Centala, Compressive failure strengths and modes of woven S2-glass reinforced polyester due to quasi-static and dynamic loading, International Journal of Plasticity 18, (December 2001) pp 1337-1357

22) Wen H.M, Predicting the penetration and perforation of FRP laminates struck normally by projectiles with different nose shapes, Composites Structures Vol. 49 2000, pp.321-329.

23) Wen H.M, Penetration and Perforation of thick FRP laminates, Composites Science and Technology, Vol. 61, 2001, pp. 1163-1172

24) Vinson, Jack R. and E. Woldesenbet, "Fiber Orientation Effects on High Strain Rate Properties of Graphite/Epoxy Composites," Journal of Composite Materials, Vol. 35, No. 6 (2001) pp 509-515.

25) Woldenbet E and Vinson J.R Effect of specimen geometry in High Strain Rate Testing of Graphite/epoxy Composites In Proceeding of 38th AIAA/ASME/ASCE/AHS/ASC. Structural. Dynamics and material conference, Vol 2 (1997), pp 927-934

26) Rodriguez, J. and M.A. Martinez, "High Strain Rate Properties of Aramid and Polyethylene Woven Fabric Composites," Department of Materials Sciences, Polytechnic University of Madrid.

27) Shivakumar, K.N. and W. Elber,"Prediction of Impact Force and Duration Due to Low-Velocity Impact on Circular Composite Laminates," Journal of Applied Mechanics, Vol. 52 (September 1985) pp 674-677

28) Sohn, M.S. and X.Z. Hu,"Impact and high strain rate delamination characteristics of carbon fiber epoxy composites" Theoretical and Applied Fracture Mechanics 25, (1996)

29) Chen, W. and D.J. Frew, "Dynamic Compression Testing of Soft Materials," Journal of Applied Mechanics, Vol. 69, (May 2002), pp. 214-223.

30) Bibo G.A, Hogg P.J. Influence of reinforcement architecture on damage mechanisms and residual strength of glass-fibre/epoxy composite systems. Composites Science and Technology, Vol. 58, 1998, pp 803-813

31) Lagace P.A, Wolf E. Impact damage resistance of several laminated material systems. 34th AIAA Structure, Structural Dynamic matter conference. 1993 pp 1863-1872

32) Pablo D. Zavattieri, Hung-Chen Lu, Sunil K Dwievi and H.D Espinosa. Energy dissipation in Ballistic Penetration of Fiber Composites, 1999, pp 1-13

33) Kolsky, H Stress waves in Solids. Dover Publication New York, 1963

34) Ferreira, F.J. and M.A. Vaz,"The Role of Specimen Geometry for accurate Characterisation of Bone Properties using the Split Hopkinson Pressure Bar," Workshop on Bone Mechanics at Instituto Superior Technico, (June 2002)

35) Roark R.J and Young W.C. Formulas for stress and strain. New York: MCGraw-Hill Book Co. 1975, pp332.

36) Nwosu S.N. Survivability studies: High-energy Penetration/Perforation mechanics of composite plate using an integrative Split Hopkinson bar and High speed optical imaging system, Air Force Final report, April 2003.

37) Brockington, A. "Calibration and Low Energy Impact Damage Analysis of Split Hopkinson Pressure Bar, University of Pittsburgh senior project (2002).